Mohamed Boudiaf University - M’sila

FACULTY OF TECHNOLOGY

ELECTRICAL ENGINEERING DEPARTMENT

Serial Number:……………….
Registration Number: 201533067098

Thesis

Presented for the attainment of the

DOCTORATE LMD

Field: Electrical engineering

Specialization: Renewable Energy

TITLE

Contribution to the Improvement of Control Strategies for Electric Drive Systems Dedicated to Electric Vehicles

Presented by:

MOHAMMED BOUKHARI

Defended on: 18 / 12 / 2025
Before the jury was composed of:

Name & Surname	Rank	Institution	Role
SAID BARKAT	**Professor**	Univ. of M’sila, Algeria	President
ISMAIL GHADBANE	**Professor**	Univ. of M’sila, Algeria	Supervisor
RIAD BOUZIDI	**MCA**	Univ. of M’sila, Algeria	Co-Supervisor
ABDELMALIK ZORIG	**MCA**	Univ. of M’sila, Algeria	Examiner
OUALID AISSA	**MCA**	Univ. of BBA, Algeria	Examiner
NOUREDDINE HAMOUDA	**Senior Researcher**	DSTA, CRTI, Algiers, Algeria	Examiner

Academic Year: 2025/2026

Université Mohamed Boudiaf - M'sila

FACULTE DE TECHNOLOGIE
DEPARTEMENT DE GENIE ELECTRIQUE

Numéro de série……………….
Numéro d'inscription : 201533067098

Thèse

Présentée pour l'obtention du diplôme de

DOCTORAT LMD

Filière : Electrotechnique

Spécialité : Energie Renouvelable

THEME

Contribution à l'amélioration de la commande du système d'entraînement électrique dédié aux véhicules électriques

Présentée par :

BOUKHARI MOHAMMED

Soutenue le : 18 / 12 / 2025
Devant le jury composé de :

Nom & Prénom	Grade	Etablissement	Qualité
BARKAT SAID	**Professeur**	Univ. de M'sila, Algérie	Président
GHADBANE ISMAIL	**Professeur**	Univ. de M'sila, Algérie	Encadreur
BOUZIDI RIAD	**MCA**	Univ. de M'sila, Algérie	Co-Encadreur
ZORIG ABDELMALIK	**MCA**	Univ. de M'sila, Algérie	Examinateur
AISSA OUALID	**MCA**	Univ. de BBA, Algérie	Examinateur
HAMOUDA NOUREDDINE	**Maître de Recherche Classe (A)**	DSTA, CRTI, Alger, Algérie	Examinateur

Année Universitaire : 2025/2026

Acknowledgments

This thesis presents the research work conducted as part of the PhD program in Electrical Engineering at the University of Mohamed Boudiaf, M'sila, Algeria.

First and foremost, I would like to express my deepest gratitude to Allah, the Most Gracious and the Most Merciful, for granting me the strength, patience, and wisdom to complete this work.

I would like to express my sincere appreciation to my supervisor, **Prof. Ismail Ghadbane** and my co-supervisor, **Dr. Riad Bouzidi**, thank you for your continuous support, encouragement, and insightful guidance throughout my doctoral journey.

I would also like to express my sincere gratitude to the members of the jury for honoring me with their time and expertise: **Prof. Said Barkat**, President of the jury; **Dr. Abdelmalik Zorig**, Examiner from the University of M'sila; **Dr. Noureddine Hamouda**, Senior Researcher at DSTA, CRTI, Algiers, Algeria; and **Dr. Oualid Aissa**, Assistant Professor at the University of Bordj Bou Arreridj (BBA)

I would also like to extend my special thanks to **Dr. Ahmed Bendib**, and **Dr. Amar Guichi**, for their guidance, support, and valuable discussions throughout my research.

My sincere thanks also go to **Prof. Aissa Chouder**, and **Prof. Djalal Eddine Khodja**, professors at the University of M'sila, for their academic encouragement, constructive feedback, and generous support.

I am also deeply grateful to **Prof. Saad Mekhilef** from the University of Malaya (Malaysia), **Prof. Messaoud Saidani**, and **Dr. Lu Wang** from Coventry University (United Kingdom) for their warm welcome during my internships at their respective institutions. I sincerely appreciate the valuable knowledge I gained from their extensive experience.

Furthermore, I would like to thank all the members of the Electrical Engineering Laboratory, including professors, doctors, and my colleagues, for creating a collaborative and supportive research environment.

Last but certainly not least, I am forever grateful to my parents for their unconditional love, prayers, and sacrifices, as well as to my brothers, sisters, and friends for their constant support and encouragement.

Dedication

I dedicate this humble thesis
To my beloved parents, whose countless sacrifices have enabled me to pursue and achieve my goals. May they find here the full measure of my gratitude and appreciation.
To my dear sisters and brothers.
To my esteemed professor, Elkheir Merabet.
To my respected supervisor, Professor Ismail Ghadbane.
To my valued co-supervisor, Dr. Riad Bouzid.
To all my colleagues and friends.
To all my teachers, from primary school to the present day.

★ *Abstract* ★

This thesis presents the development, implementation, and experimental validation of advanced sensorless control strategies for induction motor–based electric vehicle (Ev) drive systems. To address the growing demand for efficient, reliable, and cost-effective electric propulsion, the proposed approaches eliminate mechanical speed sensors, thereby reducing system cost and complexity while enhancing robustness in harsh operating environments.

The first contribution of this work is a low-cost sensorless scalar control strategy based on a Second-Order Generalized Integrator Frequency-Locked Loop (Sogi-Fll), in which rotor speed and stator frequency are estimated in real time using only a single stator current sensor. This configuration significantly reduces hardware requirements and computational burden, making it particularly suitable for high-speed operating regions and applications where simplicity and energy efficiency are prioritized. Experimental results demonstrate stable operation and satisfactory speed regulation at medium and high speeds, although performance degrades at reduced speeds due to inherent limitations associated with fixed-slip operation.

To overcome these limitations and enhance the dynamic performance of the drive system, an improved sensorless Direct Torque Control (SDtc) strategy is subsequently developed using a Multiple-Enhanced Sogi-Fll (Mesogi-Fll) estimator. In this scheme, two stator current sensors are employed to enable more accurate estimation of torque and stator flux. The Mesogi-Fllimproves harmonic and DC-offset rejection as well as frequency estimation accuracy, resulting in faster torque response and superior flux regulation under dynamic operating conditions. While the proposed sensorless Dtc approach significantly enhances overall drive performance, its effectiveness remains constrained in very low-speed regions, where estimation sensitivity increases.

Comprehensive simulation studies are conducted using Matlab/Simulink, followed by real-time experimental validation on a dSPACE MicroLabBox control platform using ControlDesk. The experimental test bench, comprising an induction motor, a power electronic inverter, and real-time control hardware, enables thorough evaluation of the proposed strategies under realistic operating scenarios. Overall, the results confirm that the sensorless scalar control offers a simple and economical solution for high-speed applications, whereas the sensorless Dtc scheme provides superior torque and flux control for demanding dynamic conditions, highlighting the complementary nature of the proposed approaches for electric vehicle drive systems.

Keywords--- Induction Motor (Im), Direct Torque Control (Dtc), Speed Sensorless Control (Ssc), dSPACE MicroLabBox, Multiple enhanced second-order generalized integrator-frequency locked-loop (Mesogi-Fll).

★ *Résumé* ★

Cette thèse présente le développement, la mise en œuvre et la validation expérimentale de stratégies avancées de commande sans capteur pour les systèmes d'entraînement des véhicules électriques (EV) à moteur asynchrone. Afin de répondre à la demande croissante en solutions de propulsion électrique efficaces, fiables et économiquement viables, les approches proposées éliminent les capteurs mécaniques de vitesse, ce qui permet de réduire les coûts et la complexité du système tout en améliorant sa robustesse dans des environnements de fonctionnement sévères.

La première contribution de ce travail consiste en une stratégie de commande scalaire sans capteur à faible coût, basée sur un intégrateur généralisé du second ordre associé à une boucle de verrouillage de fréquence (SOGI-FLL). Dans cette approche, la vitesse du rotor et la fréquence statorique sont estimées en temps réel à partir d'un seul capteur de courant statorique. Cette configuration réduit significativement les exigences matérielles et la charge de calcul, ce qui la rend particulièrement adaptée aux régimes de fonctionnement à vitesse élevée et aux applications privilégiant la simplicité et l'efficacité énergétique. Les résultats expérimentaux montrent un fonctionnement stable et une régulation de vitesse satisfaisante aux vitesses moyennes et élevées, bien que les performances se dégradent à vitesse réduite en raison des limitations inhérentes à l'utilisation d'un glissement fixe.

Afin de dépasser ces limitations et d'améliorer les performances dynamiques du système d'entraînement, une stratégie avancée de commande directe du couple sans capteur (SDTC) est ensuite développée en s'appuyant sur un estimateur SOGI-FLL à améliorations multiples (MESOGI-FLL). Dans cette configuration, deux capteurs de courant statorique sont utilisés pour permettre une estimation plus précise du couple électromagnétique et du flux statorique. Le MESOGI-FLLaméliore le rejet des harmoniques et des composantes continues, ainsi que la précision de l'estimation fréquentielle, ce qui se traduit par une réponse rapide du couple et une meilleure régulation du flux en régime dynamique. Bien que la commande DTC sans capteur proposée améliore significativement les performances globales de l'entraînement, son efficacité demeure limitée dans les régimes de très basse vitesse, où la sensibilité de l'estimation augmente.

Des études de simulation approfondies sont réalisées sous MATLAB/SIMULINK, suivies d'une validation expérimentale en temps réel à l'aide d'une plateforme de contrôle dSPACE MicroLabBox et du logiciel ControlDesk. Le banc d'essais expérimental, comprenant un moteur asynchrone, un onduleur de puissance et un système de commande en temps réel, permet une évaluation complète des stratégies proposées dans des conditions de fonctionnement réalistes. Dans l'ensemble, les résultats confirment que la commande scalaire sans capteur constitue une solution simple et économique pour les applications à vitesse élevée, tandis que la commande DTC sans capteur offre un contrôle supérieur du couple et du flux pour des conditions dynamiques exigeantes, mettant ainsi en évidence le caractère complémentaire des approches proposées pour les systèmes d'entraînement des véhicules électriques.

Mots clés---Moteur Asynchrone, Commande Directe du Couple, Commande Sans Capteur de Vitesse, dSPACE MicroLabBox, Intégrateur Généralisé Multi-Amélioré du Second Ordre avec Boucle de Verrouillage de Fréquence (MESOGI-FLL).

★ الملخص ★

تتناول هذه الأطروحة تطوير وتنفيذ والتحقق التجريبي من استراتيجيات متقدمة للتحكم بدون حساسات في أنظمة الدفع الخاصة بالمركبات الكهربائية المعتمدة على المحرك الحثي. واستجابةً للطلب المتزايد على حلول دفع كهربائية تتسم بالكفاءة والموثوقية وانخفاض التكلفة، تعتمد المقاربات المقترحة على الاستغناء عن حساسات السرعة الميكانيكية، مما يساهم في تقليل تعقيد النظام وتكلفته، مع تعزيز متانته وملاءمته لظروف التشغيل القاسية.

تتمثل المساهمة الأولى لهذا العمل في تطوير استراتيجية تحكم قياسي بدون حساسات ومنخفضة التكلفة، تعتمد على المُكامل المعمم من الرتبة الثانية المقترن بحلقة قفل التردد (SOGI-FLL). في هذه المقاربة، يتم تقدير سرعة الدوار وتردد العضو الثابت في الزمن الحقيقي باستخدام حساس واحد فقط لتيار العضو الثابت. ويساهم هذا التكوين في تقليل المتطلبات العتادية والحمل الحسابي بشكل ملحوظ، مما يجعله مناسبًا بشكل خاص لمجالات التشغيل ذات السرعات العالية والتطبيقات التي تُعطي الأولوية للبساطة والكفاءة الطاقوية. وتُظهر النتائج التجريبية استقرارًا جيدًا في التشغيل وتنظيمًا مرضيًا للسرعة عند السرعات المتوسطة والعالية، إلا أن الأداء يتدهور عند السرعات المنخفضة نتيجة القيود الملازمة لاعتماد قيمة انزلاق ثابتة.

ولتجاوز هذه القيود وتحسين الأداء الديناميكي لنظام الدفع، تم بعد ذلك تطوير استراتيجية متقدمة للتحكم المباشر في العزم بدون حساسات (S-DTC) بالاعتماد على مُقدِّر MESOGI-FLL المحسَّن متعدد المراحل. في هذا الإطار، يتم استخدام حساسين لتيار العضو الثابت من أجل تمكين تقدير أكثر دقة لكل من العزم الكهرومغناطيسي وتدفق العضو الثابت. ويُحسِّن MESOGI-FLL من رفض التوافقيات والمركبات المستمرة، إضافةً إلى زيادة دقة تقدير التردد، مما يؤدي إلى استجابة سريعة للعزم وتحكم أفضل في التدفق تحت ظروف تشغيل ديناميكية. وعلى الرغم من أن استراتيجية التحكم المباشر في العزم بدون حساسات المقترحة تُحسن بشكل كبير الأداء العام للنظام، إلا أن فعاليتها تظل محدودة في مناطق السرعات المنخفضة جدًا، حيث تزداد حساسية التقدير.

تم إجراء دراسات محاكاة شاملة باستخدام MATLAB/Simulink، تلتها عملية تحقق تجريبي في الزمن الحقيقي بالاعتماد على منصة التحكم dSPACE وبرنامج ControlDesk. ويتكون منصب الاختبار التجريبي من محرك حثي، ومحول قدرة إلكتروني، ومنظومة تحكم آنية، مما يسمح بتقييم دقيق وشامل للاستراتيجيات المقترحة تحت ظروف تشغيل واقعية. وبصفة عامة، تؤكد النتائج أن التحكم القياسي بدون حساسات يُعد حلاً بسيطًا واقتصاديًا للتطبيقات ذات السرعات العالية، في حين يوفر التحكم المباشر في العزم بدون حساسات تحكمًا متفوقًا في العزم والتدفق للتطبيقات ذات المتطلبات الديناميكية العالية، مما يُبرز الطابع التكميلي للمقاربات المقترحة في أنظمة دفع المركبات الكهربائية.

الكلمات المفتاحية--- محرك الحث، التحكم المباشر في العزم، التحكم بدون حساس للسرعة، دي سبيس ميكرولاب بوكس، مقدر متعدد محسّن من نوع الحلقة التزامنية لتكامل عام من الدرجة الثانية.

List of Publications Related to the Thesis

Journal Publications

1- Boukhari, M., Bouzidi, R., Ghadbane, I., Khaled, B., Bendib, A., & Abdelhammid, K. (2025). REAL-TIME IMPLEMENTATION OF ESOGI-FLL-BASED SPEED-SENSORLESS CONTROL FOR INDUCTION MOTOR DRIVES WITHIN ELECTRIC VEHICLE SYSTEMS. Archives of Automotive Engineering/Archiwum Motoryzacji, 107(1). https://doi.org/10.14669/AM/202568

2- Bouzidi, R., Ghadbane, I., Boukhari, M., Bendib, A., & Kherbachi, A. (2022). Experimental implementation of low-cost and robust sensorless control based on SOGI-FLL estimator for electric vehicles. International Journal of Power Electronics and Drive Systems, 13(4), 1993. https://doi.org/10.11591/ijpeds.v13.i4.pp1993-2004

3- Bouzidi, R., Ghadbane, I., & Boukhari, M. (2022). Experimental Study of an Induction Motor Using Scalar Control Method Applied in Electric Vehicle. Przegląd Elektrotechniczny, 98. https://doi.org/10.15199/48.2022.11.02

Conference Proceedings

1- Mohammed, B., Ismail, G., & Riad, B. (2022, May). Sensorless Scalar Control Based On SOGI-FLL for an Induction Motor U sed in Electric Vehicle. In 2022 19th International Multi-Conference on Systems, Signals & Devices (SSD) (pp. 2121-2126). IEEE. https://doi.org/10.1109/SSD54932.2022.9955687

2- Mohammed, B., Ismail, G., & Riad, B. Sensorless speed control based on PLL of two induction motors used in electric vehicle. In 1st International Conference on Innovative Academic Studies on 10-13 September in 2022 at Konya/Turkey, pp. 346. Conferences link: https://www.icias.net/

3- Mohammed, B., Ismail, G., & Riad, B. Speed Control of Two Induction Motors Using a Five Arms DC-AC Inverter. In 4th International Conference on Applied Engineering and Natural Sciences on 10-13 November in 2022 at Konya/Turkey, pp. 247. Conferences link: https://www.icias.net/

4- Mohammed, B., Ismail, G., Riad, B., & Khaled, B. Sensorless Processor-in-the-Loop (PIL) Control of an Induction Motor Using an STM Microcontroller. In 2nd International Conference on Recent and Innovative Results in Engineering and Technology February 10-11 in 2025 in Konya, Turkey, pp. 57. Conferences link: https://as-proceeding.com/index.php/icriret/home

5- Mohammed, B., Ismail, G., Riad, B., Khaled, B, & Khaled, B. & Field-Oriented Control of Dual Front-Wheel Motors in Electric Vehicles. In The First National Conference on Renewable Energies and Advanced Electrical Engineering (NC-REAEE'25), May 06-07th, 2025 , M'Sila (Algeria). Conferences link: https://media.univ-msila.dz/NC-REAEE25

Table of Contents

List of Figures

List of Tables

Symbols & Abbreviations

EV	Electric Vehicle.
IM	Induction motor.
SC	Scalar Control.
FOC	Field-Oriented Control.
DTC	Direct Torque Control.
MRAS	Model Reference Adaptive System.
EKF	Extended Kalman Filter.
SMO	Sliding Mode Observer.
ANN	Artificial Neural Networks.
SOGI	Second-Order Generalized Integrator.
FLL	Frequency-Locked Loop.
MESOGI	Multiple Enhanced Second-Order Generalized Integrator.
SSC	Sensorless Scalar Control.
SDTC	Sensorless Direct Torque Control.
ICE	Internal Combustion Engine.
BEVS	Battery Electric Vehicles.
HEVS	Hybrid Electric Vehicles .
PHEVS	Plug-in Hybrid Electric Vehicles .
FCEVS	Fuel Cell Electric Vehicles.
PMSM	Permanent Magnet Synchronous Motor.
SRM	Switched Reluctance Motor.
PLL	Phase-Locked Loop.
PWM	Pulse-Width Modulation.
NEDC	New European Driving Cycle.

v_{sa}, v_{sb}, v_{sc}	stator phase voltages.
v_{ra}, v_{rb}, v_{rc}	rotor phase voltages.
i_{sa}, i_{sb}, i_{sc}	stator phase currents.
i_{ra}, i_{rb}, i_{rc}	rotor phase currents.
$\psi_{sa}, \psi_{sb}, \psi_{sc}$	stator flux linkages.
$\psi_{ra}, \psi_{rb}, \psi_{rc}$	rotor flux linkages.
R_s	stator resistance.
R_r	rotor resistance.
L_s	stator self-inductance.
L_r	rotor self-inductance.
M_{s-r}	magnetizing inductance.
M_s	mutual inductance of stator phases.
M_r	mutual inductance of rotor phases.
Ω_r	Rotor angular speed.
p	Number of pole pairs.
J	Moment of inertia of the motor and load.
T_{em}	Electromagnetic torque produced by the motor
T_r	Load torque.
C_f	Friction coefficient.
W	storage energy.
θ_g	the geometry angle.
θ_e	the electric angle.
v_{ds}, v_{qs}	stator voltages in the direct and quadrature axes.
v_{dr}, v_{qr}	rotor voltages in the direct and quadrature axes.
i_{ds}, i_{qs}	stator currents in the direct and quadrature axes.
i_{dr}, i_{qr}	rotor currents in the direct and quadrature axes.
ω_s, ω_r	the synchronous and rotor angular speeds.
F_{rr}	The rolling resistance force.
K_r	the tire rolling resistance coefficient.
m	the total mass of the vehicle.
g	the gravitational acceleration.
F_{hc}	the Hill Climbing Force.
F_{ad}	Aerodynamic Drag Force.
ρ	the air density.
C_d	the aerodynamic drag coefficient.
A_s	the frontal (projected) surface area.
V	the vehicle velocity.
F_a	Acceleration Force.
a	the vehicle acceleration.
g_r	the gear ratio.
F_{te}	Total Tractive Effort.

General Introduction

The rapid depletion of fossil fuels and the growing global concern over environmental degradation have accelerated the transition toward sustainable transportation technologies. Among the emerging solutions, electric vehicles (EVs) have gained considerable attention as a viable alternative to conventional internal combustion engine (ICE) vehicles. EVs offer remarkable environmental and economic benefits, including zero tailpipe emissions, enhanced energy efficiency, and reduced dependency on petroleum-based fuels [1]. Furthermore, continuous advances in power electronics, battery energy density, and intelligent control systems have significantly improved the performance and affordability of modern EVs, thereby promoting their large-scale adoption [2].

At the heart of every electric vehicle lies the electric traction drive, which determines its dynamic performance, efficiency, and overall reliability. Induction motors (IMs) remain one of the most preferred choices for EV propulsion due to their ruggedness, low cost, and maintenance-free operation [3]. However, achieving optimal performance from an IM requires precise control of its electromagnetic torque and stator flux, motivating the development of various control strategies.

The scalar control (also known as V/f control) represents the earliest and simplest method used in IM drives. It maintains a constant ratio between the stator voltage and frequency to control motor speed. The main advantage of scalar control lies in its simplicity, low cost, and ease of implementation using open-loop schemes [4]. Nevertheless, it suffers from a slow dynamic response and poor torque control accuracy, making it less suitable for high-performance applications such as traction systems in EVs [5]. To overcome these limitations, the Field-Oriented Control (FOC) technique was introduced. FOC decouples the torque- and flux-producing components of the stator current, allowing the induction motor to behave similarly to a separately excited DC motor [6]. This decoupling enables precise control of torque and flux, leading to improved dynamic performance and high efficiency. However, the FOC approach requires accurate knowledge of motor parameters and complex coordinate transformations, which can increase system cost and sensitivity to parameter variations [7]. A further advancement, known as Direct Torque Control (Dtc), was later developed to enhance dynamic response and reduce computational complexity. Dtc directly regulates the electromagnetic torque and stator flux by selecting optimal voltage vectors through hysteresis controllers [8]. The method is celebrated for its simplicity, robustness, and ultra-fast torque response. Yet, it is also characterized by torque and flux ripples, as well as variable switching frequency, which can degrade performance and complicate inverter design [9].

In high-performance Ev drives, the use of mechanical sensors for speed measurement introduces additional cost, reduced reliability, and maintenance challenges. To address these issues, sensorless control techniques have emerged as a promising alternative by estimating rotor speed and position from measurable electrical quantities. Several observer and estimation-based methods have been developed for this purpose. The Model Reference Adaptive System (Mras) is one of the most widely adopted approaches due to its simple structure, low computational burden, and good steady-state accuracy [10]. However, its performance deteriorates at very low speeds, where parameter sensitivity becomes significant [11]. The Extended Kalman Filter (Ekf) technique offers improved noise immunity and estimation precision by statistically processing system uncertainties [12]; despite its high accuracy, the Ekf is computationally intensive and requires precise system modeling, limiting its suitability for low-cost embedded platforms [13]. The Sliding Mode Observer (Smo), on the other hand, provides strong robustness against parameter variations and external disturbances [14], yet it often suffers from chattering effects that may cause undesirable oscillations and torque ripples in the drive system [15].

More recently, Artificial Intelligence (AI)-based estimators have been proposed to overcome some of the limitations of classical observers. Artificial Neural Networks (ANNs) can learn the complex nonlinear mapping between measurable stator quantities (voltages and currents) and mechanical states (rotor speed and flux), enabling direct data-driven estimation without explicit reliance on analytical motor models; ANNs have shown good accuracy and adaptability to parameter variations, but they require representative training data and careful training/validation to avoid overfitting and ensure generalization across operating conditions [16]. Adaptive Neuro-Fuzzy Inference Systems (ANFIS) and other neuro-fuzzy approaches merge the learning capability of neural networks with the interpretable rule-based structure of fuzzy systems; these hybrid estimators handle nonlinearities and uncertainty effectively and often improve low-speed and transient performance compared with plain Mras schemes, albeit at the cost of increased design complexity and the need for training/tuning [17]. Data-driven and learning-based control approaches such as reinforcement learning (RL) or self-tuning fuzzy controllers (often combined with simplified FLC structures) offer promising avenues for online adaptation and reduced computational load through tailored rule sets; these methods can reduce the need for explicit model identification but typically require careful reward shaping, safety constraints during learning, and validation to avoid unsafe exploration in real hardware [18]. Finally, hybrid schemes that combine classical observers (MRAS, EKF, SMO) with AI modules-for example, ANN-based parameter adaptation or neuro-fuzzy speed estimators have demonstrated improved robustness and faster transient response by exploiting the complementary strengths of model-based and data-driven approaches; nevertheless, they inherit both the complexity of hybrid architectures and the need for dataset collection, algorithm tuning, and validation across the full operating envelope of the Ev traction drive [19]. Collectively, these AI-enhanced estimators extend the capability of sensorless control to challenging conditions (very low speed, parameter variation, noisy measurements), but successful deployment demands careful design, training, and real-time implementation strategies.

Recent research efforts have increasingly focused on improving the reliability, accuracy, and dynamic response of sensorless control schemes through advanced signal estimation and adaptive filtering techniques. Among these, the Second-Order Generalized Integrator with Frequency-Locked Loop (Sogi-Fll) has gained significant attention due to its outstanding capability in precisely extracting fundamental components of voltage and current signals, even under conditions of harmonic distortion and noise [20]. Originally developed for grid synchronization in single-phase and three-phase power systems, the Sogi-Fll provides accurate estimation of amplitude, phase, and frequency-attributes that make it highly suitable for applications involving dynamic signal tracking and phase-locked control [21]. Recognizing its robustness and fast dynamic performance, this study extends the use of the Sogi-Fll framework to the sensorless speed estimation of induction motors in electric vehicle drive systems. The estimator's inherent ability to isolate fundamental signal components allows for reliable flux and speed estimation without relying on mechanical sensors, thereby enhancing overall system robustness and reducing cost.

To further enhance estimation precision and dynamic adaptability, an improved structure known as the Multiple Enhanced Second-Order Generalized Integrator with Frequency-Locked Loop (Mesogi-Fll) is introduced. This enhanced approach incorporates multiple adaptive estimation loops and variable gain tuning mechanisms, enabling faster convergence, better noise rejection, and improved performance under varying load and speed conditions. By integrating the Mesogi-Fll into the sensorless control framework, the proposed method achieves an optimal trade-off between computational simplicity and estimation accuracy, making it highly suitable for real-time implementation in high-performance EV traction drives.

This thesis aims to develop and evaluate advanced sensorless control strategies for the IM used in EV applications. The research focuses on improving the performance of SC and DTC under sensorless operation by exploiting advanced frequency estimation techniques, namely the SOGI-FLL and MESOGI-FLL estimators. In this context, the work provides a comprehensive study of EV systems and their motor drive requirements, including powertrain modeling and the dynamic behavior of IMS. Furthermore, a sensorless speed control (SSC) strategy based on the SOGI-FLL estimator is developed as a simple and cost-effective solution for low-performance or energy-efficient applications. In parallel, a robust sensorless Direct Torque Control (SDTC) strategy using the MESOGI-FLL estimator is proposed to achieve fast torque response, without relying on mechanical sensors. Finally, the effectiveness of the proposed control strategies is validated and compared through simulation and experimental results using MATLAB/SIMULINK and real-time implementation on dSPACE MicroLabBox hardware.

To achieve the objectives of this research, the thesis is organized into four chapters. Chapter 1 provides an overview of EVs, including their architecture, components, and energy systems, and discusses motor selection and key challenges in EV drive design. Chapter 2 presents a comprehensive modeling of the EV powertrain, covering the DC-AC inverter, IM, and vehicle dynamics, and derives the dynamic behavior and control requirements of the motor mathematically. Chapter 3 details the sensorless scalar control (SSC) strategy using the SOGI-FLL estimator, including the estimation process, control algorithm, and both simulation and experimental results with thorough analysis. Chapter 4 proposes a sensorless DTC method based on the MESOGI-FLL estimator to estimate rotor speed and flux, and validates the algorithm through simulations and real-time experiments under various operating conditions. Through this research, a high-performance, cost-effective, and fully sensorless IM drive solution for modern EVs is anticipated.

Chapter 1

Overview of Electric Vehicle Technology

1.1 Introduction

The rapid depletion of fossil fuel reserves and the increasing concerns about environmental pollution have driven a significant shift toward sustainable transportation solutions. Among these solutions, electric vehicles (EVs) have emerged as a promising alternative to conventional internal combustion engine (ICE) vehicles. EVs offer several advantages, including reduced greenhouse gas emissions, higher energy efficiency, and lower operating costs [22]. The growing adoption of EVs is further supported by advancements in battery technology, power electronics, and motor control strategies [23]. However, despite these advantages, challenges related to performance, cost, and infrastructure development remain critical areas of research [24].

To understand the complexities of electric vehicle technology and its drive systems, it is essential to explore the fundamental aspects of EVs, including their architecture, configurations, key components, and motor selection criteria. This chapter provides an overview of these elements to establish a strong foundation for the subsequent chapters, which focus on improving electric drive systems for EV applications.

The architecture of electric vehicles forms the basis of their design and operation. It consists of several crucial subsystems, including the powertrain, energy storage, power conversion, and charging infrastructure [25]. Each of these subsystems plays a vital role in defining the efficiency, performance, and reliability of the vehicle. A well-structured architecture ensures optimal energy utilization and seamless interaction between the components.

Given the diversity in electric vehicle designs, multiple EV configurations have been developed to meet different application needs [26]. These configurations include Battery

Electric Vehicles (BEVs), which rely entirely on battery power; Hybrid Electric Vehicles (HEVs), which combine an internal combustion engine with an electric motor; Plug-in Hybrid Electric Vehicles (PHEVs), which offer extended electric driving capabilities with external charging options; and Fuel Cell Electric Vehicles (FCEVs), which utilize hydrogen fuel cells to generate electricity [27]. Each configuration presents unique advantages and limitations, influencing their adoption in different market segments [28].

The performance and efficiency of an electric vehicle are largely determined by its main components, which include the battery, power electronics, electric motor, transmission system, and control unit. Battery technology is a key factor in determining the vehicle's range, charging time, and energy density [29]. Advances in lithium-ion batteries, solid-state batteries, and alternative energy storage methods continue to shape the future of EVs [30]. Power electronics and inverters are essential for converting and managing electrical energy efficiently, while electric motors serve as the primary propulsion system, directly impacting vehicle performance, efficiency, and control complexity [31]. The transmission system ensures effective power delivery to the wheels, and control and energy management systems optimize the interaction between different components to enhance efficiency and driving experience [32].

A critical aspect of EV design is the selection of the appropriate electric motor. The choice of motor significantly affects the vehicle's efficiency, power output, torque characteristics, and overall driving experience. The most commonly used electric motors in EVs applications include Induction Motors (IMs), Permanent Magnet Synchronous Motors (PMSMs), and Switched Reluctance Motors (SRMs) [33]. Each motor type has distinct characteristics, influencing factors such as efficiency, cost, control complexity, and performance under various operating conditions [34]. This section provides a comparative analysis of these motor technologies and their suitability for different EV applications [35].

In summary, this chapter establishes the foundational knowledge required to understand the operation and design considerations of EVs. By exploring the architecture, configurations, key components, and motor selection criteria, this chapter provides the necessary background for the discussion in the following chapters, which focus on improving the control and performance of electric drive systems dedicated to EVs.

1.2 Electric Vehicle Architecture

Electric vehicle architecture plays a crucial role in defining the overall performance, efficiency, and reliability of the vehicle. The architecture includes key subsystems such as the powertrain, energy storage, power conversion, and charging systems, which work together to ensure optimal operation. The design of these components determines the driving range, charging time, energy efficiency, and environmental impact of the vehicle. Recent advancements in power electronics, battery technology, and control systems have significantly improved Ev architecture, making electric vehicles more competitive with Ice vehicles. This section explores the primary elements of Ev architecture, providing an in-depth analysis of the powertrain structure, energy storage and management, power conversion system, and charging infrastructure.

1.2.1 Powertrain Structure

The powertrain of an Ev comprises all components responsible for converting electrical energy stored in the vehicle's battery into mechanical energy at the wheels, thereby enabling vehicle motion. Unlike conventional vehicles, which rely on internal combustion engines, Evs use electric motors as their primary source of propulsion. The configuration and design of the powertrain significantly influence vehicle efficiency, performance, weight distribution, cost, and overall driving dynamics.

A typical electric vehicle powertrain is illustrated in Fig 1.1. As shown, the powertrain can be broadly divided into three main parts: the energy source, the power converter, and the electro-mechanical actuator. The energy source, represented by the battery pack, provides the electrical energy required for vehicle operation. The power converter, which includes the DC-DC converter, Dc-Ac inverter, energy management unit, and vehicle controller, regulates and conditions this energy, ensuring that the voltage, current, and frequency supplied to the motor are optimized for efficient operation. Finally, the electro-mechanical actuator, comprising the electric machine and mechanical transmission, transforms the electrical energy into mechanical torque and delivers it to the wheels, enabling controlled vehicle motion.

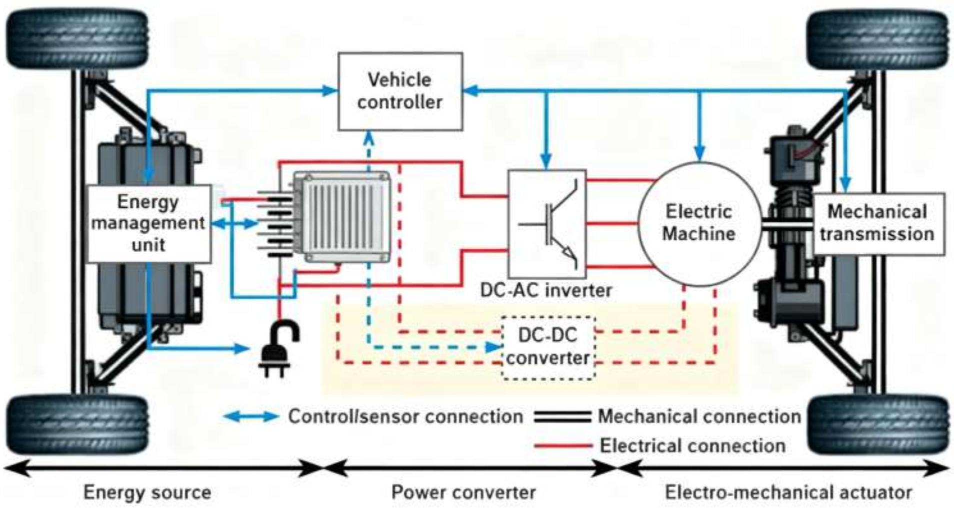

Fig 1.1. Powertrain structure of an electric vehicle.

Recent advances in motor technologies, such as PMSMand IM, have greatly improved the efficiency, reliability, and power density of electric powertrains [24]. These technological improvements, combined with optimized power electronics and energy management strategies, enable EVs to achieve high performance while maintaining low energy consumption. Therefore, the powertrain represents a central aspect of electric vehicle design, directly affecting operational capabilities and energy efficiency.

1.2.2 Energy Storage and Management

Energy storage and management are critical elements in EVs, directly influencing driving range, charging time, efficiency, and overall vehicle performance. The selection and integration of an energy storage system affect the vehicle's weight, cost, and sustainability, making it a central consideration in EV design.

The primary energy storage technology in modern EVs is the lithium-ion (Li-ion) battery, which offers high energy density, long cycle life, and relatively fast charging capabilities [36]. Lithium-ion batteries have become the standard choice due to their favorable balance between energy capacity, durability, and cost. Emerging technologies, such as solid-state batteries (SSB), promise even higher energy density and improved safety by replacing the liquid electrolyte with a solid one. Hydrogen fuel cells, employed in Fuel Cell Electric Vehicles (FCEVs), generate electricity through a chemical reaction between hydrogen and oxygen, providing an alternative approach for long-range applications. Ultra-capacitors are also utilized in conjunction with batteries to deliver high power density for applications such as regenerative braking and rapid acceleration.

A Battery Management System (BMS) is an integral component of the energy storage system. It continuously monitors battery voltage, current, temperature, and state-of-charge to ensure safe operation, optimize performance, and prolong battery life. In addition, the energy management unit of an EV coordinates the interaction between the energy storage system and the powertrain, controlling the flow of energy to meet the vehicle's dynamic demands efficiently.

Figure 1.2 illustrates the various energy sources employed in EVs and their integration through an intelligent energy management system. As depicted, modern EVs can utilize multiple types of energy storage technologies, including batteries (electrochemical storage), fuel cells (chemical storage), ultracapacitors or supercapacitors (electrical storage), and flywheels (mechanical storage). Each of these technologies serves a distinct function within the system: the battery provides steady and long-term energy supply; the fuel cell generates electricity through chemical reactions to extend vehicle range; the ultracapacitor delivers high power density for transient operations such as acceleration and regenerative braking;

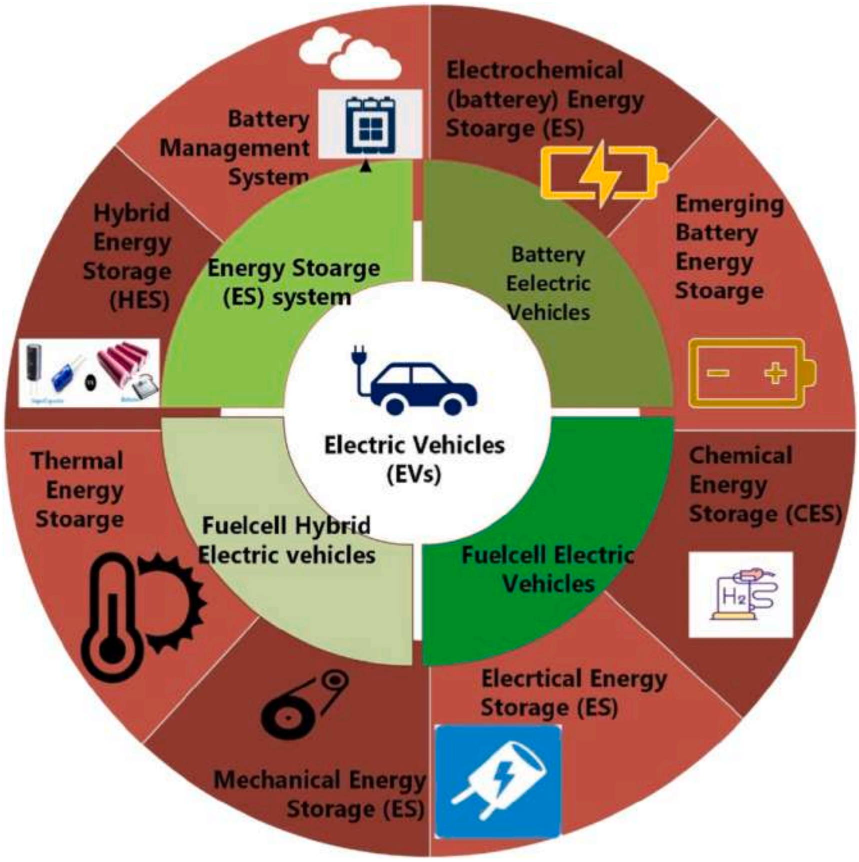

Fig 1.2. Schematic of energy storage and management in an electric vehicle.

and the flywheel contributes mechanical energy storage for rapid energy exchange. The energy management system coordinates these diverse sources to ensure optimal power sharing, efficiency, and reliability according to driving conditions. Such a hybrid energy storage configuration improves dynamic performance, extends component lifespan, and enhances the overall energy efficiency and sustainability of electric vehicles.

1.2.3 Power Conversion System

The power conversion system in an Ev is a key subsystem responsible for managing and regulating the flow of electrical energy between multiple energy sources, the traction motor, and auxiliary components. It ensures efficient power conversion and distribution under varying operating conditions, contributing to improved performance, extended driving range, and overall energy efficiency of the vehicle.

As illustrated in Fig 1.3, a typical Ev power conversion system integrates multiple energy sources-such as a fuel cell, supercapacitors, and a battery-through individual Dc-Dc converters connected to a common Dc-link. The Dc-link acts as a central energy bus that stabilizes the voltage and enables bidirectional power exchange among the vari-

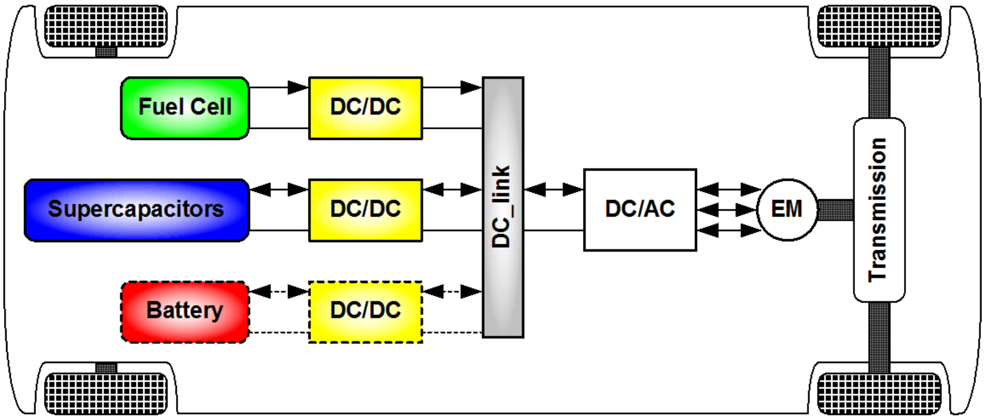

Fig 1.3. Typical configuration of a multi-source power conversion system in EVs.

ous sources. The combined electrical power is then supplied to a DC/AC inverter, which converts the direct voltage into alternating voltage to drive the electric motor. The mechanical torque generated by the motor is transmitted to the wheels through the transmission system.

In this configuration, each energy source plays a complementary role in the overall power management strategy. The fuel cell typically provides continuous base power, the battery delivers sustained energy during normal operation, and the supercapacitors handle transient high-power demands such as acceleration or regenerative braking. The coordinated control of these subsystems ensures optimal utilization of each energy source, enhances dynamic performance, and improves system reliability. Continuous advancements in power electronics, particularly with the adoption of wide bandgap semiconductor materials such as Silicon Carbide and Gallium Nitride, have further increased the efficiency, power density, and thermal stability of modern EV power conversion systems [37].

1.2.4 Charging System

The charging system is a fundamental part of electric vehicle infrastructure, directly influencing convenience, user acceptance, and the widespread adoption of EVs. It governs the process of transferring energy from the electrical grid to the vehicle battery while ensuring safety, efficiency, and battery longevity.

Figure 1.4 presents a general types of EV charging systems according to power level and mode of energy transfer. **Ac charging** utilizes standard household or dedicated charging points, typically providing power between 3 kW and 22 kW. This method is suitable for overnight or workplace charging. In contrast, **Dc fast charging** supplies high-power direct current-ranging from 50 kW up to 350 kW directly to the battery, substantially reducing charging time and enabling long-distance travel.

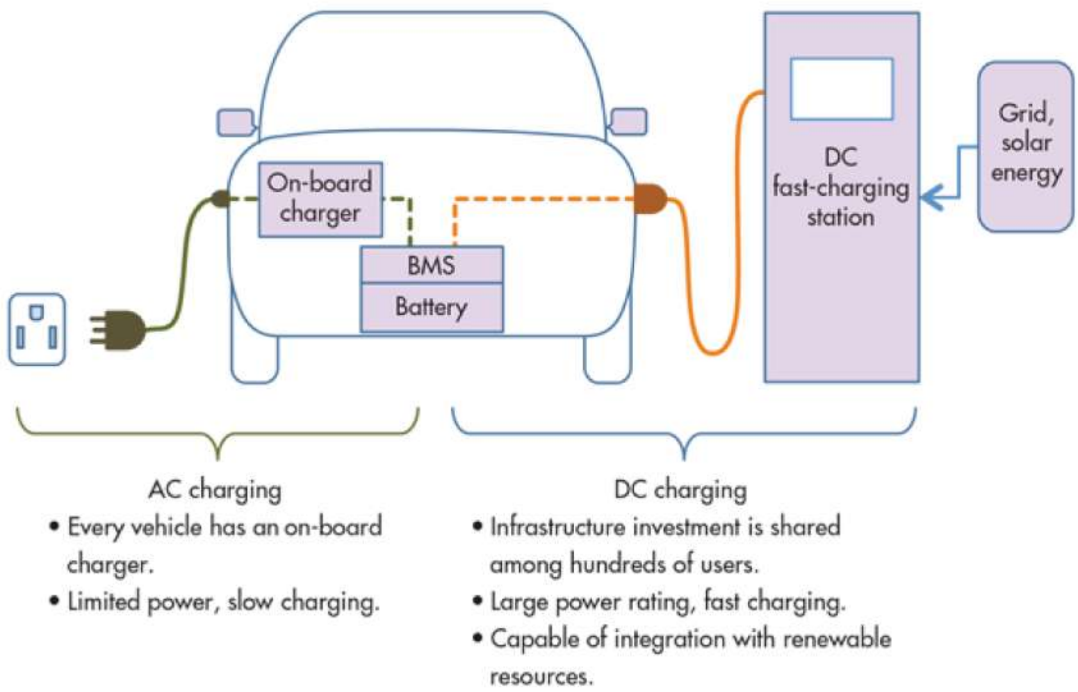

Fig 1.4. Types of general charging methods for electric vehicles.

Emerging technologies such as **wireless charging** transfer energy via inductive or resonant magnetic coupling without physical connectors, enhancing user convenience and enabling potential integration with autonomous vehicle systems. The continuous development of fast-charging infrastructure, supported by government initiatives and industrial partnerships, remains a critical factor for large-scale EV adoption. Moreover, standardization efforts in communication protocols and safety requirements are further improving the interoperability and reliability of global charging networks. [38].

1.3 Configurations of Electric Vehicles

Electric vehicles are designed in a variety of configurations, determined by how they source, store, and utilize electrical energy for propulsion. These configurations influence vehicle performance, energy efficiency, infrastructure requirements, and environmental impact. The four principal types of EVs are Battery Electric Vehicles (BEVs), Hybrid Electric Vehicles (HEVs), Plug-in Hybrid Electric Vehicles (PHEVs), and Fuel Cell Electric Vehicles (FCEVs). Each configuration embodies a distinct approach to electrification, ranging from fully electric powertrains to hybrid systems integrating conventional internal combustion engines (ICEs) with electric motors.

1.3.1 Battery Electric Vehicles (BEVs)

Battery Electric Vehicles operate solely on electrical energy stored in onboard batteries, typically lithium-ion packs. EVs produce zero tailpipe emissions and are recharged through the electrical grid. Technological advances in battery energy density, cost reduction, and fast-charging infrastructure have contributed to the widespread adoption of BEVs in the current automotive market [39].

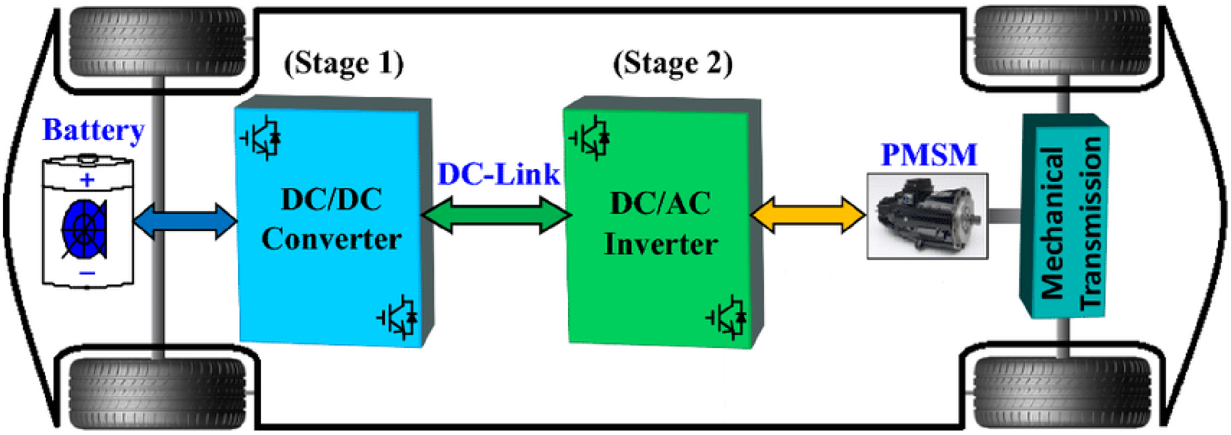

Fig 1.5. Schematic representation of a Battery Electric Vehicle (BEV) configuration.

Key Characteristics:

- Absence of an internal combustion engine.
- Regenerative braking to recover energy.
- Long-term cost efficiency and environmental benefits.

1.3.2 Hybrid Electric Vehicles (HEVs)

Hybrid Electric Vehicles combine a conventional internal combustion engine with an electric motor. The electric motor assists the ICE during acceleration and captures energy through regenerative braking, improving fuel economy and reducing emissions. Unlike BEVS or PHEVS, HEVs cannot be recharged externally; their batteries are charged solely by the ICEand regenerative braking [40].

Key Characteristics:

- Smaller battery capacity compared to BEVs and PHEVs.
- Improved fuel efficiency relative to conventional vehicles.
- Independent of external charging infrastructure.

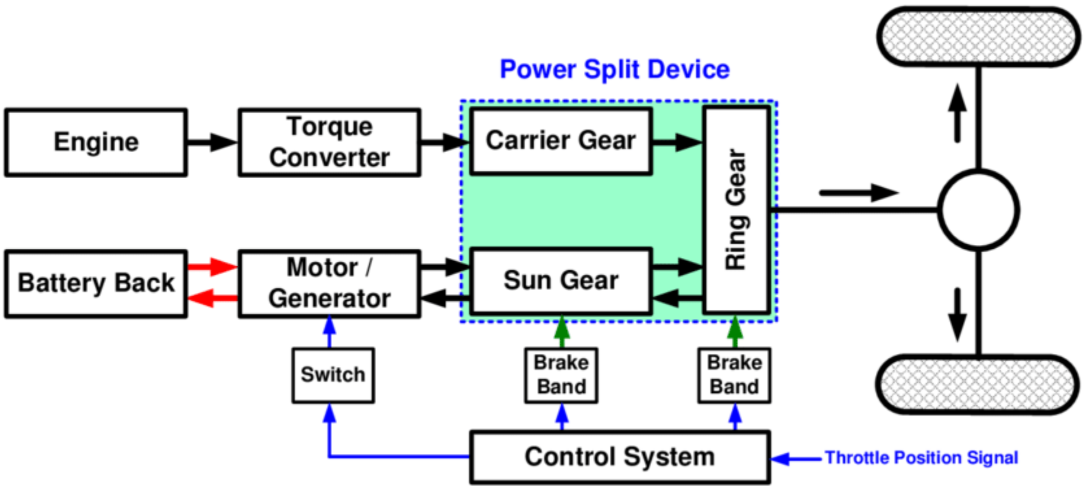

Fig 1.6. Schematic representation of a Hybrid Electric Vehicle (HEV) configuration.

1.3.3 Plug-in Hybrid Electric Vehicles (PHEVs)

Plug-in Hybrid Electric Vehicles combine an ICE with a larger battery than that of HEVs, allowing external charging. PHEVs enable electric-only operation for limited distances while using the ICE for extended range, providing a transitional option for users hesitant to adopt full electrification [41].

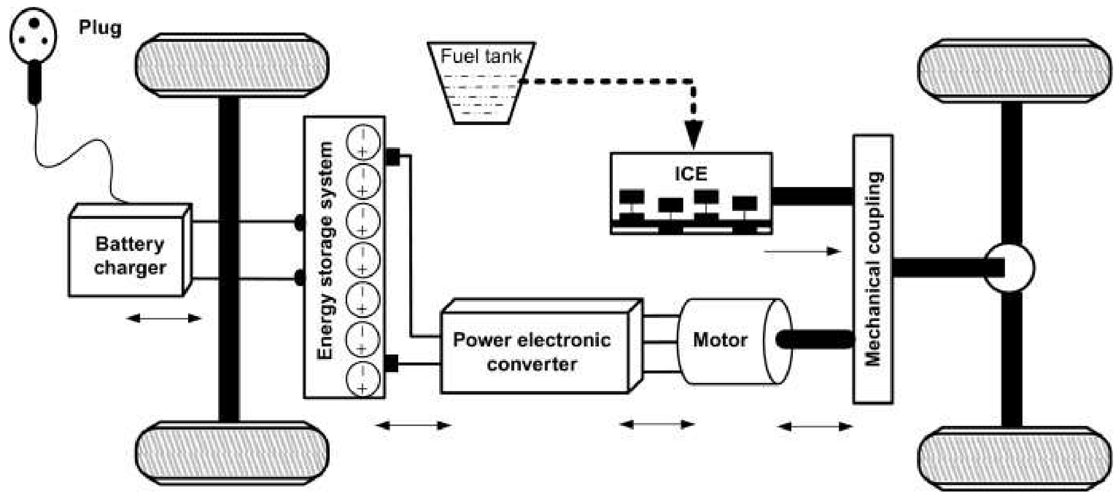

Fig 1.7. Schematic representation of a Plug-in Hybrid Electric Vehicle (PHEV) configuration.

Key Characteristics:

- Dual power sources: battery and ICE.
- Electric-only driving range typically between 20 and 80 km.
- Ability to recharge from the electrical grid.

1.3.4 Fuel Cell Electric Vehicles (FCEVs)

Fuel Cell Electric Vehicles utilize hydrogen stored onboard to generate electricity through a fuel cell, which then powers the electric motor. FCEvs provide long driving ranges and rapid refueling, making them suitable for long-distance and heavy-duty applications. Nevertheless, hydrogen refueling infrastructure is currently limited compared to battery charging networks [42].

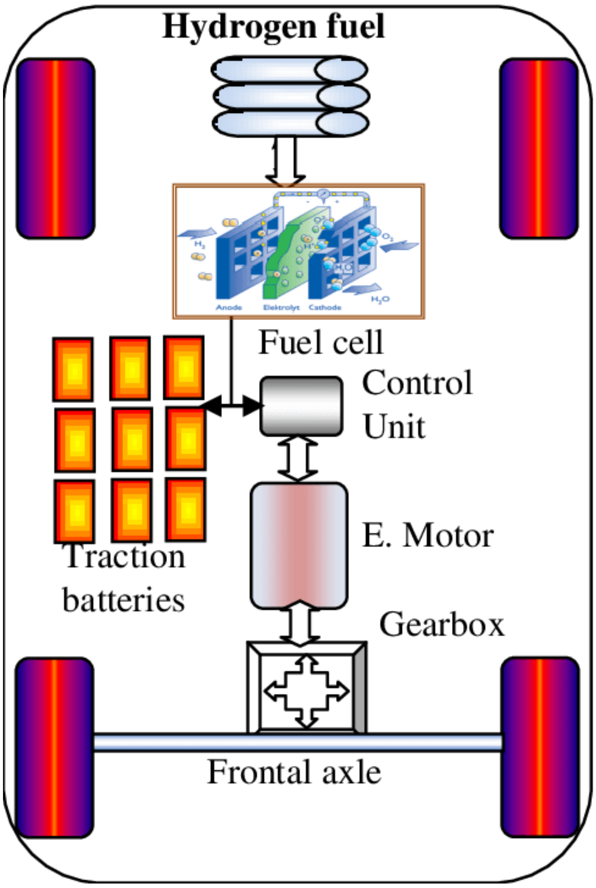

Fig 1.8. Schematic representation of a Fuel Cell Electric Vehicle (FCEV) configuration.

Key Characteristics:

- Zero tailpipe emissions (only water vapor is produced).
- High energy efficiency with rapid refueling capability.
- Deployment limited by hydrogen infrastructure and production challenges.

1.4 Electric Motor Selection for Electric Vehicles

The choice of an electric motor is one of the most critical decisions in the design of EVs. It directly influences the vehicle's efficiency, performance, cost, and reliability. Different motor technologies offer varying advantages in terms of torque characteristics, efficiency, cost, and control complexity. The optimal selection depends on vehicle type, intended use, and energy management strategies. This section explores the essential criteria for motor selection and compares the most commonly used motors in EVs: Induction Motors (IMs), Permanent Magnet Synchronous Motors (PMSMs), and Switched Reluctance Motors (SRMs).

Choosing the right motor involves evaluating several technical and economic factors. The most important selection parameters include [48]:

- Power density: Influences weight and space requirements.
- Torque-speed characteristics: Determines performance across different driving conditions.
- Efficiency: Affects driving range and energy consumption.
- Thermal performance: Impacts cooling requirements and reliability.
- Cost and availability of materials: Especially for rare earth magnets.
- Control complexity: Influences the design of the electronic control system.

1.4.1 Induction Motors (IMs)

Induction Motors are widely used due to their ruggedness, reliability, and absence of permanent magnets, which reduces material costs. They use electromagnetic induction to generate torque and are known for good thermal performance and cost-effectiveness [49].

Advantages:

- Robust and durable.
- Lower cost due to absence of magnets.
- Proven industrial reliability.

Limitations:

- Lower efficiency compared to PMSMs at low loads.
- Larger and heavier for the same power output.

1.4.2 Permanent Magnet Synchronous Motors (PMSMs)

PMSMs are the most widely adopted motors in modern EVs due to their high efficiency, power density, and excellent torque control. These motors use rare earth magnets to maintain constant magnetic fields [50].

Advantages:

- High efficiency over a wide speed range.
- Compact design with high torque-to-weight ratio.
- Superior dynamic performance and control.

Limitations:

- High cost due to rare earth materials.
- Demagnetization risk at high temperatures.

1.4.3 Switched Reluctance Motors (SRMs)

SRMs are gaining interest for EV applications due to their simple construction, absence of magnets, and high-temperature tolerance. Torque is produced by the reluctance difference between rotor and stator poles [51].

Advantages:

- Simple and robust construction.
- No permanent magnets required.
- High-speed operation and fault tolerance.

Limitations:

The main limitations of SRMs arise from their operating principle. High torque ripple occurs because torque is generated by the nonlinear reluctance variation between stator and rotor poles, leading to pulsations. These pulsations produce vibrations and acoustic noise, particularly at high speeds. Furthermore, the nonlinear and position-dependent characteristics of the motor require more complex control algorithms to achieve smooth and precise torque and speed regulation.

1.4.4 Comparison and Suitability for EV Applications

The selection of an appropriate electric motor for an EV largely depends on the intended application, such as passenger vehicles, commercial vehicles, or high-performance electric vehicles. Different motor types exhibit significant variations in torque density, efficiency, cost, reliability, and maintenance requirements, which directly influence the vehicle's overall performance, energy consumption, and operational lifespan. Table 1.1 summarizes key performance parameters for four commonly used motor types: Permanent Magnet Synchronous Motors (PMSMs), Switched Reluctance Motors (SRMs), Induction Motors (IMs), and DC motors [52].

Table 1.1. Comparison of electric motor types for EV applications

Parameter	PMSM	SRM	IM	DC Motor
Power Density	High	Moderate	Moderate	Low to Moderate
Torque Density	High	Moderate	Moderate	Moderate
Efficiency	>90%	>90%	>90%	75–85%
Cost	High	Low	Moderate	Low
Reliability	High	Very High	High	Moderate
Fault Tolerance	Low	High	Moderate	Low
Cooling Requirements	High	Moderate	Moderate	Low to Moderate
Maintenance	Low	Very Low	Low	High
Typical Applications	Passenger EVs	Commercial EVs	Passenger/Commercial EVs	Low-power or specialized EVs

Based on Table 1.1 PMSMs offer high power and torque density, excellent efficiency, and low maintenance, making them ideal for passenger EVs and high-performance applications where compactness and responsiveness are critical. However, reliance on permanent magnets increases cost and reduces fault tolerance.

SRMs provide moderate power and torque density but excel in reliability and robustness. Their simple, low-cost design suits commercial or industrial EVs, though torque ripple and noise can affect passenger comfort.

Induction motors balance performance, cost, and reliability, and are widely used in both passenger and commercial EVs. They are robust, do not require permanent magnets, and have slightly lower efficiency than PMSMs at partial loads.

DC motors, though less common, are used in low-power or specialized EVs. They are simple and low-cost but less efficient, require more maintenance, and are unsuitable for high-performance applications.

Overall, PMSMs dominate performance-critical applications, while SRMs and IMs are suitable for cost-sensitive or ruggedEVs, and DC motors remain niche for low-power uses.

1.5 Conclusion

In this introductory chapter, we have explored the foundational concepts and components that define EVs, establishing a solid base for the technical analyses that follow in this thesis. The transition from internal combustion engine vehicles to electric mobility represents a significant shift in the transportation sector, driven by environmental concerns, technological innovation, and evolving consumer preferences.

We began by examining the architecture of electric vehicles, emphasizing the integration and interaction of key systems including the powertrain, energy storage, power conversion, and charging infrastructure. Each subsystem plays a critical role in determining the performance, range, and efficiency of the vehicle.

Next, we analyzed the various configurations of EVs, such as Battery Electric Vehicles (BEVs), Hybrid Electric Vehicles (HEVs), Plug-in Hybrid Electric Vehicles (PHEVs), and Fuel Cell Electric Vehicles (FCEVs). These configurations differ not only in their energy sources and drivetrain complexity but also in their operational characteristics and suitability for different use cases.

The discussion then moved to the main components of EVs, where we outlined the essential role of the battery system, power electronics, electric motors, control systems, and transmission mechanisms. These components are continually evolving thanks to advances in materials, thermal management, and digital control strategies.

Finally, we addressed the selection of electric motors, comparing Induction Motors, Permanent Magnet Synchronous Motors, Switched Reluctance Motors, and DC Motors . The choice of motor depends heavily on the desired balance between performance, efficiency, cost, and reliability, making motor selection a crucial step in EV design.

In summary, a comprehensive understanding of EV architecture, configurations, and component functions is indispensable for developing and optimizing electric drive systems. This chapter serves as a foundation for the subsequent chapters, which will delve deeper into innovative strategies for improving the performance, efficiency, and integration of electric drive systems in modern electric vehicles.

Chapter 2

Comprehensive Modelling of EV Powertrain Components

2.1 Introduction

The accurate modeling of electric vehicle (EV) powertrain components constitutes a fundamental step toward the design, analysis, and implementation of advanced control strategies. A reliable model not only reflects the physical behavior of the system but also provides a platform for validating control algorithms prior to experimental deployment. In the context of EVs, the powertrain is a complex multi-domain system that integrates electrical, mechanical, and vehicular dynamics. Thus, a comprehensive modeling framework must capture the interactions between motor dynamics, parameter characteristics, and vehicle motion under diverse operating conditions.

This chapter focuses on the development and formulation of detailed models for the main components of the EV powertrain, with an emphasis on the traction motor and the vehicle dynamics. First, mathematical models of the induction motor are presented in both the dq and $\alpha\beta$ reference frames. These representations provide complementary perspectives that are widely used in control design and analysis, offering insights into steady-state and transient behavior. Second, attention is given to the identification of motor parameters, which play a crucial role in ensuring the accuracy of the model. Two approaches are considered: classical identification methods based on experimental measurements and analytical derivations, and direct computation using motor datasheet values and calculators. The comparison of these techniques highlights both their advantages and limitations in practical applications.

In addition to the motor subsystem, the vehicle dynamics are modeled to capture the interaction between the generated torque and the external forces acting on the EV. This includes the longitudinal dynamics of the vehicle, as well as the resistive forces such as aerodynamic drag, rolling resistance, gradient force, and inertial effects. Integrating these dynamics with the motor model provides a holistic view of the powertrain behavior, enabling realistic performance assessment under various driving conditions.

Overall, the comprehensive modeling presented in this chapter forms the foundation for subsequent control design and experimental validation. It establishes a coherent framework that links the motor's electrical and mechanical characteristics with the external dynamics of the vehicle, thereby supporting the development of robust and efficient EV drive systems.

2.2 Description of the IM

The implementation of efficient control strategies for the induction machine requires an accurate mathematical model that faithfully represents its dynamic behavior. Modern control techniques for induction motors, such as field-oriented control and direct torque control, rely on the continuous estimation of the rotor flux magnitude and phase, which are obtained through the machine's dynamic model. Maintaining a constant rotor flux is essential to achieve high energy efficiency while ensuring precise torque and speed control.

In this section, different mathematical models of the induction motor are developed to serve as the foundation for advanced control algorithm design. These models are primarily derived from Park's theory, which simplifies the analysis by transforming the three-phase system into an equivalent two-phase system through the Concordia transformation. Moreover, the application of Park's transformation converts sinusoidal time-varying quantities into continuous signals in the rotating reference frame, thereby facilitating both control design and numerical simulation [53, 54].

2.2.1 Simplifying Assumptions

The mathematical modeling of the induction motor is generally established under a set of simplifying assumptions that are widely accepted in the literature. These assumptions reduce the complexity of the system while retaining sufficient accuracy for control design and performance analysis. Following the approaches presented in [53–55], the principal assumptions can be summarized as follows:

- The air gap is considered uniform and constant, neglecting any spatial variations.
- The effects of stator and rotor slotting are disregarded.
- The supply voltage is assumed to be a perfectly balanced three-phase sinusoidal source.

- Core losses are neglected in order to simplify the equivalent circuit representation.
- Magnetic saturation in the core materials is ignored, assuming a linear magnetic circuit, since the motor is operated within its nominal flux range.
- Hysteresis losses, eddy currents, and skin effects are not taken into account.
- The leakage inductances of the stator and rotor are assumed to be constant.
- Stator and rotor resistances are considered constant, independent of temperature or frequency.
- The zero-sequence (homopolar) component is assumed to be zero, corresponding to a balanced three-phase system with no neutral current.
- The system is assumed to operate under steady thermal conditions, thus neglecting thermal transients.

These assumptions provide a simplified yet sufficiently accurate model of the induction motor, which is suitable for control strategy development, simulation studies, and performance evaluation. While they facilitate analytical tractability, it is important to note that deviations from these idealizations may arise in practical applications, particularly under conditions of high loading, deep saturation, or thermal variations [53–55].

2.2.2 Natural Model of the Induction Motor

The three-phase squirrel-cage induction motor is widely used in electric drive systems due to its robust construction, low cost, and minimal maintenance requirements. Structurally, the machine is composed of two main parts: the stator and the rotor. A symbolic representation is shown in Fig 2.1.

The stator is the stationary part of the machine and, in classical three-phase induction motors, consists of three distributed windings spatially displaced by 120 electrical degrees, although other winding configurations may be used in modern machines. When supplied by a balanced three-phase sinusoidal source, these windings establish a rotating magnetic field in the air gap. The stator windings are usually connected in star or delta configuration, and their primary function is to generate a magnetomotive force (MMF) produced by the stator currents, which establishes the magnetic flux in the air gap and induces currents in the rotor conductors. [53, 54].

The rotor in the squirrel-cage configuration is composed of conductive bars, typically aluminum or copper, embedded in a laminated iron core and short-circuited at both ends by end rings. Unlike wound-rotor designs, the squirrel-cage rotor does not require external electrical connections. When the rotating magnetic field produced by the stator sweeps across the rotor, a time-varying magnetic flux induces an electromotive force (EMF) in the rotor bars in accordance with Faradayâ€™s law, resulting in circulating currents due to the short-circuited structure. These induced currents interact with the stator magnetic field and experience electromagnetic (Lorentz) forces, whose resultant moment about the rotor axis produces the electromagnetic torque responsible for rotor rotation. [55].

This interaction between the stator's rotating field and the rotor's induced currents forms the physical basis of the induction motor's operation. From this physical structure, the natural model of the machine is derived in the *abc*-phase variables, which accurately represents the electrical and electromagnetic coupling in its most fundamental form. This natural model serves as the foundation for deriving simplified reference-frame models (e.g., dq and $\alpha\beta$) that are more suitable for control and simulation studies.

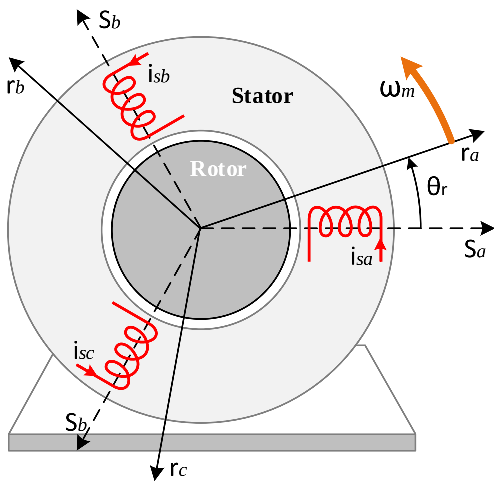

Fig 2.1. Symbolic representation of the squirrel-cage induction motor.

2.2.2.1 Electrical Equations

The electrical behavior of the induction motor in the three-phase (*abc*) reference system is described by the relationships between voltages, currents, and flux linkages in both the stator and rotor circuits. These equations account for the resistive and inductive effects under dynamic operating conditions and form the foundation of the natural model of the machine [53, 54]. The model is expressed as:

$$\begin{cases} [V_s] = [R_s][I_s] + \frac{d}{dt}[\Phi_s] \\ [V_r] = [R_r][I_r] + \frac{d}{dt}[\Phi_r] \\ [\Phi_s] = [L_s][I_s] + [M_{s-r}][I_r] \\ [\Phi_r] = [L_r][I_r] + [M_{s-r}]^T[I_s] \end{cases} \tag{2.1}$$

$$\text{with:} \begin{cases} [V_s] = [v_{sa} \ v_{sb} \ v_{sc}]^T \\ [I_s] = [i_{sa} \ i_{sb} \ i_{sc}]^T \\ [\Phi_s] = [\phi_{sa} \ \phi_{sb} \ \phi_{sc}]^T \end{cases} ; \begin{cases} [V_r] = [v_{ra} \ v_{rb} \ v_{rc}]^T \\ [I_r] = [i_{ra} \ i_{rb} \ i_{rc}]^T \\ [\Phi_r] = [\phi_{ra} \ \phi_{rb} \ \phi_{rc}]^T \end{cases} ; [R_s] = \begin{bmatrix} R_s & 0 & 0 \\ 0 & R_s & 0 \\ 0 & 0 & R_s \end{bmatrix}$$

$$[R_r] = \begin{bmatrix} R_r & 0 & 0 \\ 0 & R_r & 0 \\ 0 & 0 & R_r \end{bmatrix} ; [L_s] = \begin{bmatrix} L_s & M_s & M_s \\ M_s & L_s & M_s \\ M_s & M_s & L_s \end{bmatrix} ; [L_r] = \begin{bmatrix} L_r & M_r & M_r \\ M_r & L_r & M_r \\ M_r & M_r & L_r \end{bmatrix}$$

where:

- v_{sa}, v_{sb}, v_{sc}: stator phase voltages (V).
- v_{ra}, v_{rb}, v_{rc}: rotor phase voltages (V).
- i_{sa}, i_{sb}, i_{sc}: stator phase currents (A).
- i_{ra}, i_{rb}, i_{rc}: rotor phase currents (A).
- $\phi_{sa}, \phi_{sb}, \phi_{sc}$: stator flux linkages ($Wb$).
- $\phi_{ra}, \phi_{rb}, \phi_{rc}$: rotor flux linkages ($Wb$).
- R_s: stator resistance (Ω).
- R_r: rotor resistance (Ω).
- L_s: stator self-inductance (H).
- L_r: rotor self-inductance (H).
- M_{s-r}: magnetizing inductance (H).
- M_s: mutual inductance of stator phases (H).
- M_r: mutual inductance of rotor phases (H).

2.2.2.2 Mechanical Dynamics of the IM

The mechanical behavior of an induction motor is governed by Newton's second law of rotational motion, which relates the net torque acting on the rotor to its angular acceleration. This relationship accounts for the electromagnetic torque produced by the motor, the opposing load torque, and frictional losses. Accordingly, the mechanical equation describing the rotor acceleration can be expressed as [53, 54]:

$$\frac{d\Omega_r}{dt} = \frac{P}{J}\left(T_{em} - T_r - C_f\Omega_r\right) \tag{2.2}$$

with:
Ω_r: Rotor angular speed (rad/s).
P: Number of pole pairs.
J: Moment of inertia of the motor and load ($kg.m^2$).
T_{em}: Electromagnetic torque produced by the motor ($N{\cdot}m$).
T_r: Load torque ($N{\cdot}m$).
C_f: Friction coefficient ($N{\cdot}m{\cdot}s/rad$).

In the theory of electromagnetic fields applied to electrical machines, the electromagnetic torque (T_e) is fundamentally derived from the concept of energy conversion. Specifically, it can be expressed as the partial derivative of the stored electromagnetic energy with respect to the geometric angle. This formulation reflects the principle that torque arises from the interaction between magnetic fields and the mechanical structure of the machine, tending to minimize the stored energy by aligning magnetic forces. In addition to this energy-based expression, the electromagnetic torque can also be related to the instantaneous electromagnetic power and the mechanical angular velocity. The following equation provides the expression of T_e as a function of the electromagnetic power [53, 54]:

$$T_e = \frac{dW}{d\theta_g} = P\frac{dW}{d\theta_e} \tag{2.3}$$

with:
W: represent the storage energy.
θ_g: the geometry angle.
θ_e: the electric angle.

In the analysis of electrical machines, it is also essential to consider the absorbed power (P_a), which represents the total electrical power drawn by the machine from the electrical supply. This power includes both the useful electromagnetic power converted into mechanical form and the losses due to resistances, core effects, and other parasitic elements. The absorbed power is a crucial parameter for evaluating the efficiency and performance of the machine. It can be calculated based on the instantaneous voltages and currents at the machine terminals. The general expression for the absorbed power is given below:

$$P_a = [V_s]^T\ [I_s] \tag{2.4}$$

By substituting the expressions of voltage and current from (2.1) into the equation of absorbed power (2.4), we can derive a more detailed formulation of the absorbed power as:

$$P_a = [I_s]^T[R_s][I_s] + \frac{d}{dt}[L_s][I_s] + \frac{d}{dt}[M_{r-s}][I_r]^T[I_s] + \frac{d}{dt}[I_r]^T[M_{r-s}][I_s] \tag{2.5}$$

The obtained expression is quite complex, and it becomes increasingly difficult to continue modeling the IM in this three-phase reference frame. Due to the complexity of the equation, it is not practical to proceed with further analysis without simplifying the model.

2.2.3 Modeling of the Induction Motor in the dq Reference Frame

To facilitate the analysis and control of the induction motor, the three-phase (abc) quantities can be transformed into a two-phase rotating reference frame known as the dq-axis frame, as illustrated in Fig 2.2. This transformation, commonly referred to as the Park transformation, maps the time-varying sinusoidal stator and rotor quantities into constant or slowly varying components in the dq-frame, which rotates synchronously with a chosen reference (stator flux, rotor flux, or rotor speed) [53–55].

By performing this transformation, the induction motor model can be expressed in terms of d-axis and q-axis components, decoupling the flux-producing and torque-producing components. This approach greatly simplifies the dynamic equations, making them more suitable for the design of advanced control strategies, such as field-oriented control (FOC) and direct torque control (DTC). Mathematically, the transformation from the three-phase system defined in (2.1) to the dq-axis can be expressed as follows:

$$\begin{bmatrix} v_{ds} \\ v_{qs} \\ v_0 \end{bmatrix} = \sqrt{\frac{2}{3}} \begin{bmatrix} cos(\theta) & cos(\theta - \frac{2\pi}{3}) & cos(\theta + \frac{2\pi}{3}) \\ -sin(\theta) & -sin(\theta - \frac{2\pi}{3}) & -sin(\theta + \frac{2\pi}{3}) \\ \frac{1}{2} & \frac{1}{2} & \frac{1}{2} \end{bmatrix} \begin{bmatrix} v_{as} \\ v_{bs} \\ v_{cs} \end{bmatrix} \tag{2.6}$$

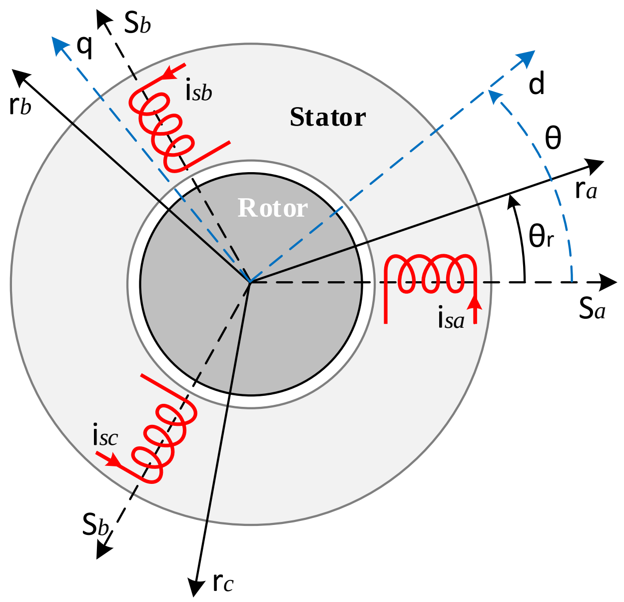

Fig 2.2. Park transformation of IM in the dq reference frame.

The dq transformation enables the stator and rotor voltage and flux equations to be represented in a form where steady-state AC quantities appear as DC quantities, facilitating control and simulation [53].

2.2.3.1 Choice of Reference Frame

To analyze the transient behavior of the three-phase induction motor, three coordinate reference frames in the (d, q) plane can be considered [56].

Stator Reference Frame In this reference frame, the (d, q) axes are fixed with respect to the stator, such that $\omega = 0$. In this case, the axis of phase S_a coincides with the d-axis. This reference frame is particularly suitable for studying instantaneous quantities, as it does not require any transformation back to the real three-phase system. Its use is advantageous for analyzing the starting and braking conditions of alternating-current machines.

Rotor Reference Frame In this reference frame, the (d, q) axes are fixed with respect to the rotor, which rotates at the mechanical angular speed ω_r; thus, $\omega = \omega_r$. This frame is commonly used to study the transient behavior of both synchronous and asynchronous machines, especially when the rotor circuits are asymmetrically connected.

Synchronously Rotating (Field-Oriented) Reference Frame In this reference frame, the (d, q) axes rotate synchronously with the rotating magnetic field produced by the stator windings, such that $\omega = \omega_s$. This reference frame is generally used for implementing control strategies such as torque or speed control, since the variables in this frame become constant (steady-state) in steady operation.

In the present work, the synchronously rotating (field-oriented) reference frame is adopted for the modeling and control of the induction motor. Under this condition, the mathematical model of the machine can be expressed as follows:

2.2.3.2 Voltages equations

The voltage equations in the dq-axis are given by:

$$\begin{cases} v_{ds} = R_s i_{ds} + \frac{d}{dt}\phi_{ds} - \omega_s \phi_{qs} \\ v_{qs} = R_s i_{qs} + \frac{d}{dt}\phi_{qs} + \omega_s \phi_{ds} \\ v_{dr} = R_r i_{dr} + \frac{d}{dt}\phi_{dr} - \omega_{sl} \phi_{qr} \\ v_{qr} = R_r i_{qr} + \frac{d}{dt}\phi_{qr} + \omega_{sl} \phi_{dr} \end{cases} \tag{2.7}$$

2.2.3.3 Flux Equations

The flux linkages in the dq-axis for both the stator and rotor are given by:

$$\begin{cases} \phi_{ds} = L_s i_{ds} + M i_{dr} \\ \phi_{qs} = L_s i_{qs} + M i_{qr} \\ \phi_{dr} = M i_{ds} + L_r i_{dr} \\ \phi_{qr} = M i_{qs} + L_r i_{qr} \end{cases} \tag{2.8}$$

Now, we can summarize both the flux and voltage equations in matrix form as follows:

$$\begin{bmatrix} v_{ds} \\ v_{qs} \\ v_{dr} \\ v_{qr} \end{bmatrix} = \begin{bmatrix} R_s & -\omega_s L_s & 0 & -\omega_s M \\ \omega_s L_s & R_s & \omega_s M & 0 \\ 0 & -\omega_{sl} M & R_r & -\omega_{sl} L_r \\ \omega_{sl} M & 0 & \omega_{sl} L_r & R_r \end{bmatrix} \begin{bmatrix} i_{ds} \\ i_{qs} \\ i_{dr} \\ i_{qr} \end{bmatrix} + \begin{bmatrix} L_s & 0 & M & 0 \\ 0 & L_s & 0 & M \\ M & 0 & L_r & 0 \\ 0 & M & 0 & L_r \end{bmatrix} \frac{d}{dt} \begin{bmatrix} i_{ds} \\ i_{qs} \\ i_{dr} \\ i_{qr} \end{bmatrix} \tag{2.9}$$

Where:

- ϕ_{ds}, ϕ_{qs} are stator fluxes in dq frame.
- ϕ_{dr}, ϕ_{qr} are rotor fluxes in dq frame.
- v_{ds}, v_{qs} are stator voltages in dq frame.
- v_{dr}, v_{qr} are rotor voltages in dq frame.
- i_{ds}, i_{qs} are stator currents in dq frame.
- i_{dr}, i_{qr} are rotor currents in dq frame.
- R_s, R_r are stator and rotor resistances.
- L_s, L_r are stator and rotor inductances.
- M is the mutual inductance.
- ω_s, ω_r, and ω_{sl} are synchronous, rotor angular speeds, and slip angular speed.

Based on (2.7), the absorbed power of the induction motor can be expressed in terms of the variables transformed into the dq reference frame. This formulation simplifies the mathematical representation of the power by eliminating time-varying components associated with the three-phase system. It provides a clearer understanding of how electrical quantities contribute to power consumption in the rotating reference frame. The absorbed power can thus be written as:

$$P_a = \underbrace{R_s(i_{ds}^2 + i_{qs}^2)}_{P_j} + \underbrace{i_{ds}\frac{d}{dt}\phi_{ds} + i_{qs}\frac{d}{dt}\phi_{qs}}_{P_{fm}} + \underbrace{\omega_s(\phi_{dr}i_{qs} - \phi_{qr}i_{ds})}_{P_{em}} \tag{2.10}$$

The electromechanical power P_{em} can be expressed in terms of the electromagnetic torque (T_{em}), the synchronous angular speed (ω_s), the rotor inductance (L_r), and the mutual inductance (M)as follows:

$$P_{em} = \frac{T_{em}\omega_s}{P}\frac{L_r}{\frac{3}{2}M} \tag{2.11}$$

By comparing the electromechanical power terms in (2.10) and (2.11), the electromagnetic torque can be expressed as:

$$T_{em} = \frac{3}{2}P\frac{M}{L_r}(\phi_{dr}i_{qs} - \phi_{qr}i_{ds}) \tag{2.12}$$

2.2.4 Modeling of the Induction Motor in the $\alpha\beta$ Axis

To analyze the behavior of the induction motor in a stationary reference frame, the three-phase system can be transformed into a two-phase orthogonal system using the Clarke transformation, as illustrated in Fig 2.3. This transformation maps the three-phase voltages, currents, and flux linkages into the stationary $\alpha\beta$ frame, which is particularly useful for control strategies such as DTC or for the preliminary stages of vector control [53–55].

The $\alpha\beta$ model allows the motor's electrical quantities to be expressed in a fixed coordinate system, eliminating the need to consider a rotating reference frame and thereby simplifying the analysis under certain conditions [53,55]. The corresponding mathematical model is given by:

$$\begin{bmatrix} v_\alpha \\ v_\beta \end{bmatrix} = \sqrt{\frac{2}{3}} \begin{bmatrix} 1 & -\frac{1}{2} & -\frac{1}{2} \\ 0 & \frac{\sqrt{3}}{2} & -\frac{\sqrt{3}}{2} \\ \frac{1}{2} & \frac{1}{2} & \frac{1}{2} \end{bmatrix} \begin{bmatrix} v_{as} \\ v_{bs} \\ v_{cs} \end{bmatrix} \tag{2.13}$$

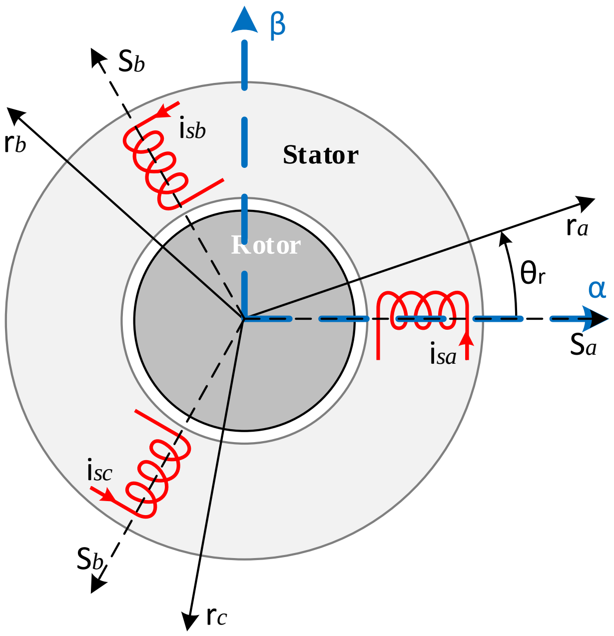

Fig 2.3. Clarke transformation of IM in the $\alpha\beta$ reference frame.

2.2.4.1 Voltage equations

In the $\alpha\beta$ reference frame, the stator and rotor voltage equations of the induction motor can be expressed as follows:

$$\begin{cases} v_{\alpha s} = R_s i_{\alpha s} + \frac{d\phi_{\alpha s}}{dt} \\ v_{\beta s} = R_s i_{\beta s} + \frac{d\phi_{\beta s}}{dt} \\ v_{\alpha r} = R_r i_{\alpha r} + \frac{d\phi_{\alpha r}}{dt} - \omega_r \phi_{\beta r} \\ v_{\beta r} = R_r i_{\beta r} + \frac{d\phi_{\beta r}}{dt} + \omega_r \phi_{\alpha r} \end{cases} \tag{2.14}$$

2.2.4.2 Flux Equations

The flux linkages are related to the currents via the following expressions:

$$\begin{cases} \phi_{\alpha s} & = L_s i_{\alpha s} + M i_{\alpha r} \\ \phi_{\beta s} & = L_s i_{\beta s} + M i_{\beta r} \\ \phi_{\alpha r} & = L_r i_{\alpha r} + M i_{\alpha s} \\ \phi_{\beta r} & = L_r i_{\beta r} + M i_{\beta s} \end{cases} \tag{2.15}$$

Substituting the flux expressions into the voltage equations leads to the compact matrix form of the model:

$$\begin{bmatrix} v_{\alpha s} \\ v_{\beta s} \\ v_{\alpha r} \\ v_{\beta r} \end{bmatrix} = \begin{bmatrix} R_s & 0 & 0 & 0 \\ 0 & R_s & 0 & 0 \\ 0 & -\omega_r M & R_r & -\omega_r L_r \\ \omega_r M & 0 & \omega_r L_r & R_r \end{bmatrix} \begin{bmatrix} i_{\alpha s} \\ i_{\beta s} \\ i_{\alpha r} \\ i_{\beta r} \end{bmatrix} + \begin{bmatrix} L_s & 0 & M & 0 \\ 0 & L_s & 0 & M \\ M & 0 & L_r & 0 \\ 0 & M & 0 & L_r \end{bmatrix} \frac{d}{dt} \begin{bmatrix} i_{\alpha s} \\ i_{\beta s} \\ i_{\alpha r} \\ i_{\beta r} \end{bmatrix} \tag{2.16}$$

2.3 Induction Motor Parameter Identification

Accurate identification of induction motor parameters is essential for precise modeling, performance analysis, and implementation of advanced control strategies in electric drive systems. The parameters of the motor, such as stator and rotor resistances, leakage and magnetizing inductances, play a fundamental role in predicting the machine's electromagnetic and mechanical behavior. In this section, two complementary identification approaches are considered. The first is based on classical experimental methods, where parameters are derived from standard tests such as the no-load and locked-rotor tests, followed by analytical computation. The second utilizes the automatic identification functions available in ABB variable-speed drives, which estimate the machine parameters through dynamic self-commissioning procedures. Recent studies have demonstrated significant progress in improving the accuracy of parameter estimation using both classical and data-driven optimization-based approaches [57–60]. The combination of these methods ensures a comprehensive and reliable parameter set for subsequent simulation and control applications.

2.3.1 Classical Induction Motor Parameter Identification

Classical experimental methods for induction motor parameter identification have been widely employed owing to their simplicity, reliability, and direct physical interpretation. These tests are based on standard electrical measurements that provide fundamental information about the motor's electrical and magnetic characteristics, such as stator and rotor resistances, leakage and magnetizing inductances, and core losses. By applying controlled voltages and recording the resulting currents, voltages, and power, the parameters can be determined with reasonable accuracy. Despite the emergence of advanced computational and drive-based identification techniques, classical methods remain essential for validation, bench-marking, and preliminary parameter estimation in both academic research and industrial practice [57–59].

2.3.1.1 Two-Phase DC Method for Stator Resistance Measurement

The two-phase DC method is a classical experimental approach used to determine the stator resistance of an induction motor. In this technique, a direct current is applied simultaneously to two stator phases, while the third phase remains open-circuited. This configuration ensures that only the resistive components of the stator windings are excited, effectively eliminating the influence of mutual inductance and core losses. Consequently, this method provides an accurate estimation of the stator resistance, which is a fundamental parameter for precise motor modeling and control [57, 58].

In the present work, a Programmable DC Power Source was connected to two stator phases of the induction motor, as illustrated in Fig 2.4. The supply voltage was gradually increased until indicates the nominal phase current of the motor. Once the nominal current was reached, the adjustment of the DC source was stopped, and both the applied voltage E and the corresponding current I_n were recorded. These measured values were then used to compute the stator resistance according to Ohm's law:

$$R_s = \frac{E}{2I_n} = \frac{62}{2 \times 2.48} \Longrightarrow \boxed{R_s = 12.5\ \Omega}. \tag{2.17}$$

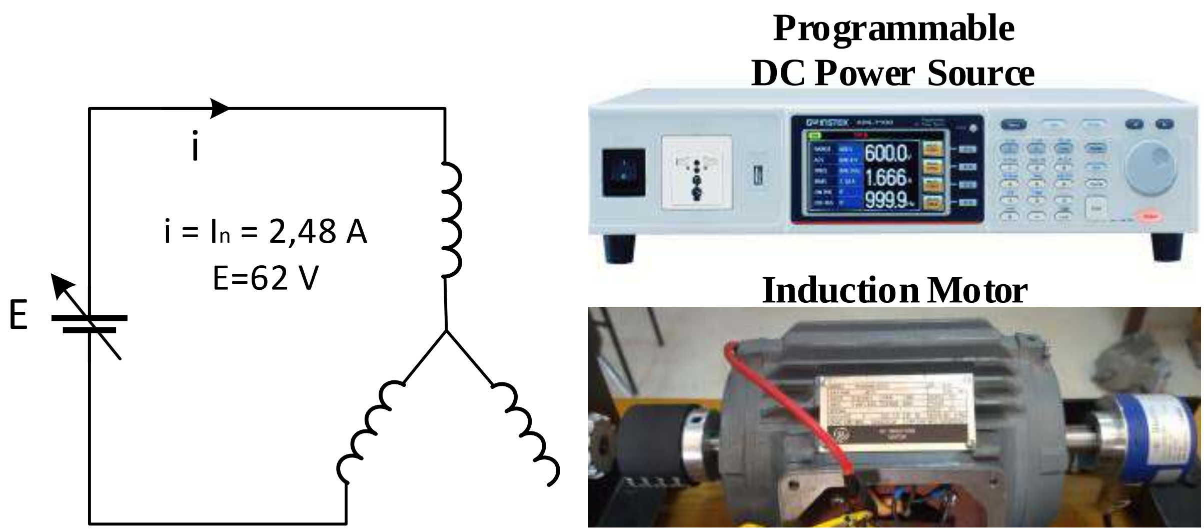

(a) (b)

Fig 2.4. Two phase DC test: (a) schematic diagram, and (b) experimental setup.

Here, R_s denotes the stator resistance, E is the applied DC voltage across two stator phases, and I_n represents the nominal phase current. This straightforward yet effective method provides reliable results for parameter identification and forms the basis for subsequent modeling and control strategies of the induction motor.

2.3.1.2 No-Load Test for Stator Inductance Calculation

In this test, the induction motor is supplied with its nominal line-to-line voltage $U = V_n$ while the rotor is allowed to rotate freely without any mechanical load. The objective of the no-load test is to determine the magnetizing characteristics of the machine and calculate the stator inductance L_s.

The experimental setup for the no-load test is shown in Fig 2.5. The three-phase power supply is connected to the stator terminals, and a Power & Harmonics Analyzer is employed to measure the input electrical quantities-namely the phase current I_0, the active power P_0, and the reactive power Q_0 under steady-state conditions at rated voltage and frequency.

Since the motor operates without a mechanical load, the total input power P_0 mainly consists of core (iron) losses (P_{fer}), mechanical losses (P_{mec}) (friction and windage), and a small portion of stator copper losses (P_{js}). The reactive power Q_0, in contrast, is predominantly associated with the magnetizing current and is directly related to the stator inductance L_s.

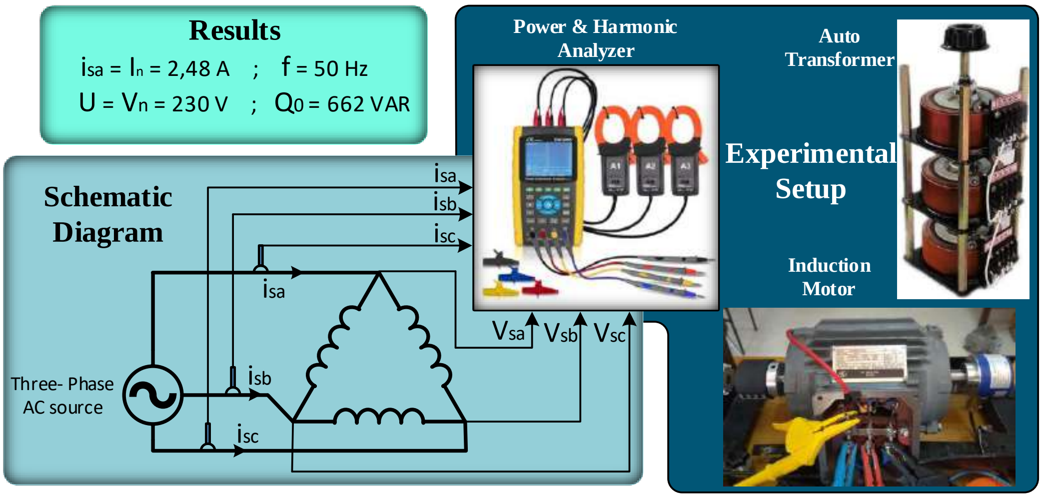

Fig 2.5. Schematic diagram and experimental setup of the no-load test.

The measured quantities are used to determine the stator inductance as follows:

$$Q_0 = \frac{3U^2}{L_s \omega_s}. \tag{2.18}$$

Rearranging for L_s:

$$L_s = \frac{3U^2}{Q_0 \omega_s} = \frac{3 \times 230^2}{662 \times 2\pi \times 50} \implies \boxed{L_s = 0.70 \text{ H}}. \tag{2.19}$$

To validate this result, the stator inductance was also measured directly using an LCR meter, which yielded $L_s = 0.71$ H. This close agreement between the two methods confirms the accuracy of the experimental procedure and validates the reliability of the calculated stator inductance.

2.3.1.3 Short-Circuit Test for Rotor and Mutual Inductance Estimation

The short-circuit (or blocked-rotor) test is a standard procedure used to determine the rotor resistance (R_r), and mutual inductance (M) of an induction motor. In this test, the rotor is mechanically locked to prevent rotation, and a reduced three-phase AC voltage is applied to the stator windings. The supply voltage is gradually increased until the stator current reaches its rated value. During the experiment, the line voltage (V_{cc}), line current (I_{cc}), active power (P_{cc}), and reactive power (Q_{cc}) are recorded using the Power & Harmonics Analyzer.

In this test, the same experimental setup as that used for the no-load test (shown in Fig 2.5) was employed. The measured quantities are as follows:

$$V_{cc} = 57,5\ V\ ;\ I_{cc} = I_n = 2.48\ A\ ;\ P_{cc} = 142.33\ W\ ;\ Q_{cc} = 185.5\ VAR\ ;\ f = 50\ Hz$$

The total active power absorbed by the induction machine under short-circuit conditions is expressed as:

$$P_{cc} = 3R_{\text{eq}} \left(\frac{I_{cc}}{\sqrt{3}} \right)^2, \tag{2.20}$$

which can be simplified to obtain the equivalent resistance:

$$R_{\text{eq}} = \frac{P_{cc}}{I_{cc}^2} = \frac{142.33}{(2.48)^2} \Longrightarrow \boxed{R_{\text{eq}} = 23.14\ \Omega}. \tag{2.21}$$

The rotor resistance referred to the stator side is thus:

$$R_r = R_{\text{eq}} - R_s = 23.14 - 12.5 \Longrightarrow \boxed{R_r = 10.64\ \Omega}. \tag{2.22}$$

The equivalent leakage inductance per phase can be determined from the reactive power component:

$$L_{eq} = \frac{Q_{cc}}{3\omega_s I_{cc}^2} = \frac{185.5}{3 \times 2\pi \times 50 \left(\frac{2.48}{\sqrt{3}} \right)^2} \Longrightarrow \boxed{L_{eq} = 0.096\ \text{H}}, \tag{2.23}$$

where $\omega_s = 2\pi f$ is the synchronous angular frequency.

In the equivalent two-winding model of the induction motor, the voltage equations are expressed as:

$$\begin{bmatrix} V_s \\ V_r \end{bmatrix} = j\omega_s \begin{bmatrix} L_s & M \\ M & L_r \end{bmatrix} \begin{bmatrix} I_s \\ I_r \end{bmatrix}. \tag{2.24}$$

When the rotor is short-circuited ($V_r = 0$), eliminating the rotor current yields the equivalent inductance seen from the stator terminals:

$$L_{eq} = L_s - \frac{M^2}{L_r}. \tag{2.25}$$

Assuming approximately equal stator and rotor leakage inductances ($L_s \approx L_r$), the mutual inductance can be obtained as:

$$M = \sqrt{L_s^2 - (L_{eq}L_s)} = \sqrt{0.71^2 - (0.096 \times 0.71)} \Longrightarrow \boxed{M = 0.66 \text{ H}}. \tag{2.26}$$

The magnetic coupling coefficient between the stator and rotor circuits is calculated as:

$$k = \frac{M}{\sqrt{L_s L_r}} = \frac{0.66}{\sqrt{0.71 \times 0.712}} = 0.93. \tag{2.27}$$

The obtained inductance values are consistent with the expected electromagnetic behavior of an induction machine. The magnetizing inductance ($M = 0.66$ H) is significantly higher than both the stator and rotor leakage inductances ($L_{ls} = 0.05$ H and $L_{lr} = 0.05$ H), confirming a strong magnetic coupling between the stator and rotor circuits. The coupling coefficient ($k = 0.93$) further supports this observation, indicating efficient magnetic energy transfer. Moreover, the condition $M^2 < L_s L_r$ is satisfied, ensuring the physical validity of the identified parameters. The equivalent inductance ($L_{eq} = 0.096$ H) is lower than the magnetizing inductance, as expected under short-circuit conditions, where leakage flux predominates. Overall, these results are physically reasonable and validate the accuracy of the parameter identification process, confirming that the adopted experimental methodology and computational approach yield reliable and consistent inductance estimations for the studied induction motor model.

2.3.1.4 Determination of Motor Inertia J and Friction Coefficient C_f

The mechanical parameters of the induction motor, namely the moment of inertia (J) and the viscous friction coefficient (C_f), play a crucial role in accurately modeling and simulating the dynamic behavior of electrical machines. These parameters directly influence the transient response, torque development, and overall efficiency of the motor. In this work, both parameters were experimentally determined using a combination of a no-load test and a deceleration test, which are widely recognized and reliable experimental methods for mechanical parameter identification of induction motors [66–68].

No-Load Test: In this test, the same experimental setup as that used for the no-load test (shown in Fig 2.5) was employed. Unlike the previous test, where only a single voltage value was applied, several voltage levels were used in this case. For each applied voltage, the corresponding active power P_0, no-load current I_0, and voltage V_0 were measured. The obtained results are presented in Table 2.1.

In addition, the stator copper losses P_{js} and the mechanical losses at each voltage were calculated for each measurement using:

$$P_{\text{js}} = R_s \, I_0^2, \tag{2.28}$$

and the sum of iron and mechanical losses P_f at each voltage were obtained as:

$$P_f = P_0 - P_{\text{js}}. \tag{2.29}$$

The squared applied voltage V_0^2 was also calculated and included in the table.

Table 2.1. Results of the no-load test, including measured and calculated values.

V_0	i_0	P_0	P_{js}	P_f	V_0^2
30	0.29	24	1.05	22.95	900
50	0.31	36	1.2	34.8	2500
80	0.433	51	2.34	48.66	6400
120	0.67	72	5.61	66.39	14400
160	0.953	94	11.35	82.65	25600
200	1.387	122	24.04	97.96	40000
220	1.71	145	36.55	108.45	48400

Table 2.1 summarizes the results of the no-load test for various applied voltage levels. It includes the measured no-load current i_0, absorbed active power P_0, the stator Joule losses P_{js}, the iron and mechanical losses P_f, and the square of the applied voltage V_0^2. The data illustrate the dependence of the motor's no-load behavior and losses on the applied voltage.

Determination of Mechanical Losses P_{mec}: During the no-load operation, the induction motor absorbs a power (P_0), which corresponds to the sum of the mechanical losses P_{mec}, iron (core) losses P_{fer}, and stator copper losses P_{js}. By plotting the curve of P_f as a function of the square of the supply voltage V_0^2, as illustrated in Fig 2.6, a straight line is generally obtained. The extrapolation of this line to zero voltage gives the mechanical losses.

Using Matlab, the total losses excluding the stator copper losses, denoted as P_f, were plotted as a function of the squared supply voltage, V_0^2, i.e., $P_f = f(V_0^2)$. The resulting plot exhibited an approximately linear relationship between P_f and V_0^2. A linear regression line was then fitted to the experimental data, as illustrated in Fig 2.6, and expressed by the equation:

$$y = 0.0019\, V_0^2 + 21. \tag{2.30}$$

From this linear representation, the intercept at $V_0 = 0$ corresponds to the mechanical losses at nominal speed, denoted as P_m. As observed in the figure, this value was found to be $P_m = 21\,W$. The slope of the line, on the other hand, reflects the iron (core) losses, which vary proportionally with the square of the supply voltage.

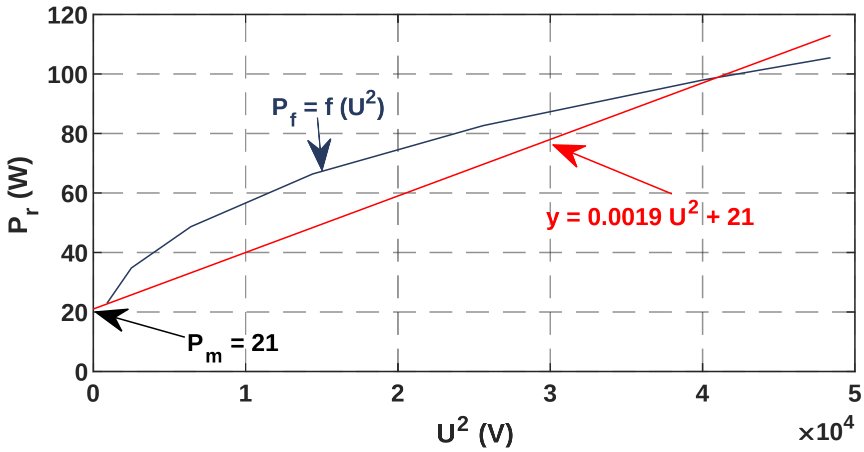

Fig 2.6. Variation of losses P_f with squared supply voltage V_0^2.

Deceleration Test: Subsequently, a deceleration test was performed. The motor was supplied with its nominal voltage and allowed to reach its synchronous speed. The supply was then cut off, and the rotor speed was recorded using the dSPACE MicroLabBox and an encoder. The recorded speed curve is shown in Fig 2.7.

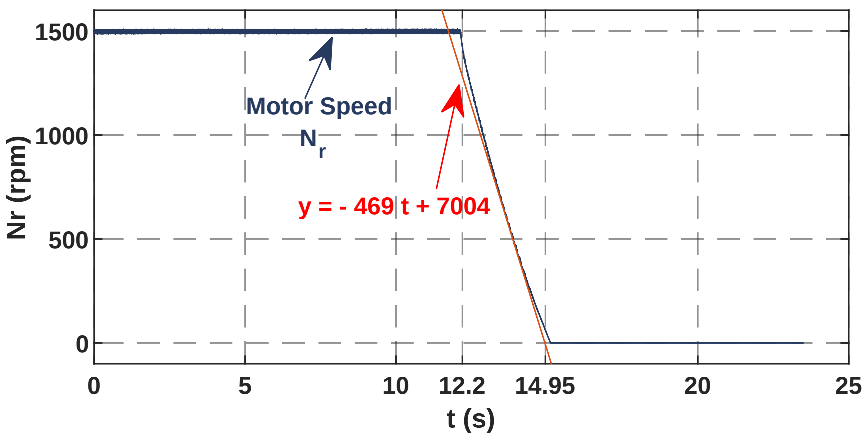

Fig 2.7. Deceleration test of the induction motor used to determine J and C_f.

A tangent line was drawn along the deceleration curve to determine the slope $\frac{d\omega}{dt}$ at nominal speed. The moment of inertia J was then calculated using:

$$J = \frac{P_{mec}}{\omega\,\frac{d\omega}{dt}} = \frac{21}{157 \cdot 57.12} \Longrightarrow \boxed{J = 0.0023\ \text{kg}{\cdot}\text{m}^2} \tag{2.31}$$

where $P_m = 21$ W, $\omega = 157$ rad/s, and $\frac{d\omega}{dt} = 57.12\ rad/s^2$.

Finally, the viscous friction coefficient C_f was determined from:

$$C_f = \frac{J}{\Delta t} = \frac{0.0023}{2.75} \Longrightarrow \boxed{C_f = 0.0008 \text{ N·m·s/rad}} \tag{2.32}$$

where $\Delta t = 14.95 - 12.2 = 2.75$ s is the characteristic time interval of deceleration. This combined approach, using both no-load and deceleration tests, allows accurate determination of the motor's mechanical parameters, which are essential for modeling its dynamic behavior.

2.3.2 IM Parameter Identification Using the ABB-VSD

In addition to the classical experimental tests, the induction motor parameters were also identified using an ABB variable-speed drive (VSD). This modern approach provides a practical and automated means of determining the electrical and magnetic characteristics of the motor, including stator and rotor resistances (R_s and R_r), leakage inductances, and magnetizing inductance [61,62]. The parameter estimation process is performed directly by the drive through a dedicated identification routine, ensuring high precision and consistency under controlled operating conditions [63] .

The experimental setup employed for this procedure is illustrated in Fig 2.8. It consists of the tested induction motor coupled to an ABB variable-speed drive, which is connected to a personal computer (PC) for real-time control, measurement, and data acquisition. The drive operates under the Direct Torque Control (DTC) mode, allowing precise regulation of the electromagnetic torque and stator flux, which enhances the reliability of the identification results [64].

Two distinct parameter identification methods available in the ABB drive software were utilized in this study [63, 65]:

- **Full Identification Run**: Called Full ID Run (FIR) is a complete dynamic test performed while the motor is allowed to rotate freely.
- **Identification Run at Standstill**: called ID Run at Standstill (IRS) is a static identification procedure conducted with the rotor locked.

Both methods were executed sequentially, and the obtained parameters were compared with the values derived from classical tests to validate the consistency and accuracy of the drive-based estimation process.

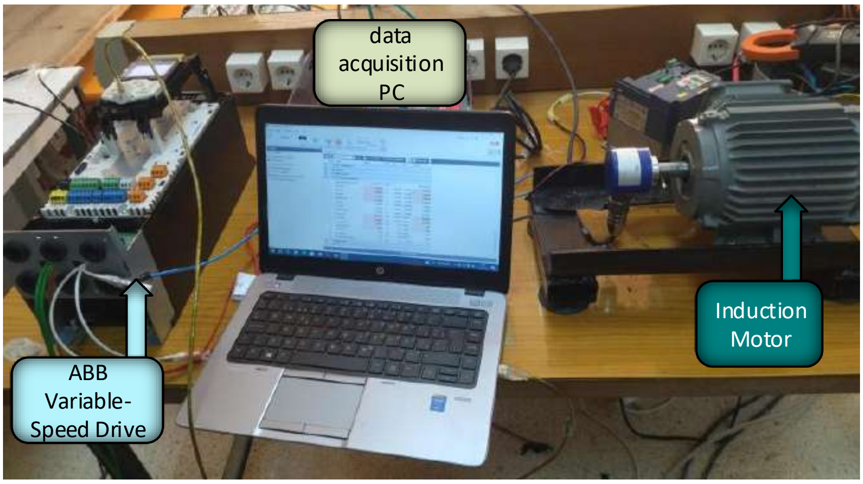

Fig 2.8. Experimental setup for IM parameter identification using the ABB VSD.

2.3.2.1 Full Identification Run

The Full ID Run (FIR) method is an automatic identification routine carried out with the motor shaft free to rotate. During this test, the ABB drive applies a sequence of controlled voltage and frequency variations, allowing the motor to operate under no-load conditions. The drive measures and analyzes the resulting electrical and mechanical responses to estimate the stator resistance, rotor resistance, magnetizing inductance, and leakage inductances.

This method provides highly accurate parameter estimation by capturing both steady-state and transient responses while the motor is rotating, accounting for magnetization, saturation, and rotor dynamics. The resulting values are suitable for dynamic control applications such as DTC and Field-Oriented Control (FOC) [63]. However, the motor must be mechanically uncoupled from any load and safely mounted to allow free rotation. The parameters identified through the FIR procedure are presented in Table 2.2.

Table 2.2. Identified induction motor parameters using the FIR method.

Parameter	Symbol	Unit	Value
Stator Resistance	R_s	Ω	11.95
Rotor Resistance	R_r	Ω	10.45
Magnetizing Inductance	M	H	0.64
Equivalent Inductance	L_{eq}	H	0.098
Stator Inductance	L_s	H	0.69
Rotor Inductance	L_r	H	0.69

2.3.2.2 Identification Run at Standstill

The ID Run at Standstill (IRS) method is an alternative identification routine that can be performed without allowing the motor shaft to rotate. In this approach, the ABB drive injects low-frequency test signals into the stator windings while the rotor remains mechanically locked. The resulting voltage and current responses are used to estimate the main motor parameters under static conditions [62, 65].

This test offers the advantage of being faster and safer, especially in cases where the motor cannot be decoupled from its mechanical load or where rotation must be avoided for safety reasons. However, since the rotor is stationary, the identification of certain dynamic parameters-such as the rotor resistance (R_r) and magnetizing inductance (M) may be less accurate compared to the FIR test [62]. Consequently, the results obtained from the IRS test are typically used for preliminary setup or verification rather than precise control tuning. The parameters identified through the IRS procedure are listed in Table 2.3.

Table 2.3. Identified induction motor parameters using IRS method.

Parameter	Symbol	Unit	Value
Stator Resistance	R_s	Ω	11.89
Rotor Resistance	R_r	Ω	7.66
Magnetizing Inductance	M	H	0.578
Equivalent Inductance	L_{eq}	H	0.098
Stator Inductance	L_s	H	0.629
Rotor Inductance	L_r	H	0.629

A comparison of the results in Table A.1 shows that the Full ID Run (FIR) produces parameters very close to those from classical experimental tests. The stator and rotor resistances, magnetizing inductance, and phase inductances exhibit only minor deviations, demonstrating that the ABB variable-speed drive accurately replicates the motor's characteristics under dynamic conditions. In contrast, the ID Run at Standstill (IRS) shows larger discrepancies, particularly in the rotor resistance (R_r) and magnetizing inductance (M), deviating more from the classical values. This confirms that while both routines are useful, the Full ID Run provides results highly consistent with classical measurements, whereas the Standstill Run is less accurate due to limitations of testing the motor without rotation. Based on this analysis, the parameters from the classical tests were selected for subsequent modeling and control of the induction motor.

Table 2.4. Summary of induction motor parameters obtained from different methods.

Parameters	Symbol	Unit	Classic	FIR	IRS
Stator Resistance	R_s	Ω	12.5	11.95	11.89
Rotor Resistance	R_r	Ω	10.64	10.45	7.66
Magnetizing Inductance	M	H	0.66	0.64	0.578
Equivalent Inductance	L_{eq}	H	0.098	0.098	0.098
Stator Inductance	L_s	H	0.7 / 0.71	0.69	0.629
Rotor Inductance	L_r	H	0.7 / 0.71	0.69	0.629
Moment of Inertia	J	$kg.m^2$	0.0023	/	/
Friction Coefficient	C_f	$N{\cdot}m{\cdot}s/rad$	0.0008	/	/

2.3.3 Validation of the Induction Motor Model

To ensure the accuracy of the developed IM model and the identified parameters, a validation study was carried out using MATLAB/SIMULINK. The purpose of this step is to verify that the simulated dynamic behavior of the IM is consistent in both frames (dq and $\alpha\beta$), and that it reflects the expected physical characteristics under load variations.

Two simulation models were implemented: one based on the Park transformation (in the dq reference frame) and the other using the Clarke transformation (in the $\alpha\beta$ reference frame), as illustrated in Fig 2.9. Both models were supplied with the same nominal stator voltage of $V_n = 230$ V. To assess the dynamic response, a load torque of $T_r = 4$ N $\cdot$ m was applied at $t = 2.5$ s. The simulation results of the two models are presented in Fig 2.10

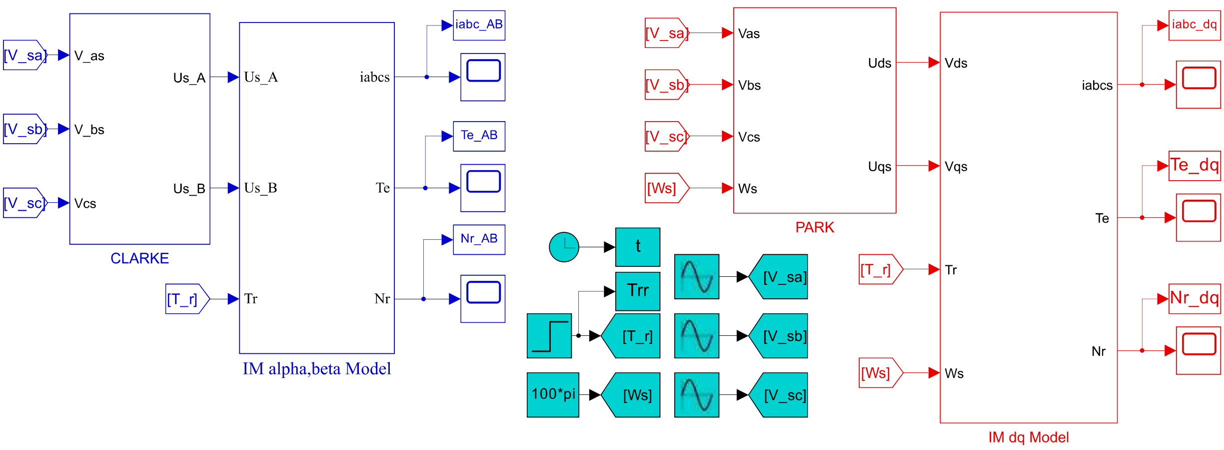

Fig 2.9. Simulation block of the IM in MATLAB/SIMULINK.

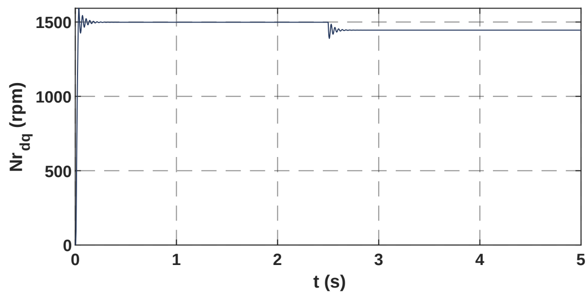

(a) Motor speed $N_{r_{dq}}$

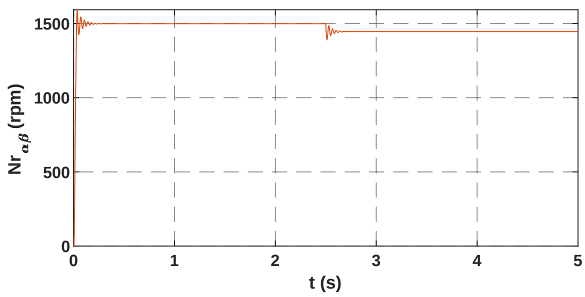

(b) Motor speed $N_{r_{\alpha\beta}}$

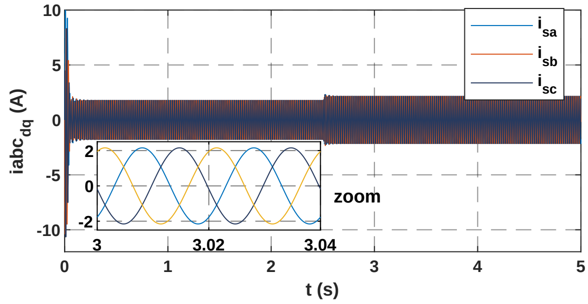

(c) Three-phase current $i_{abc_{dq}}$

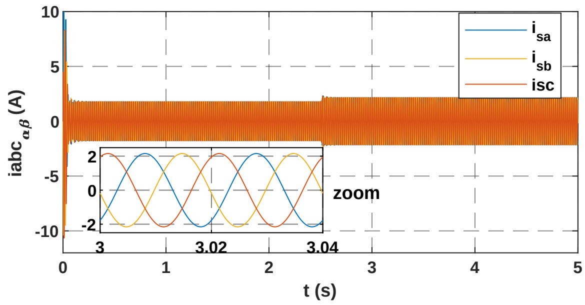

(d) Three-phase current $i_{abc_{\alpha\beta}}$

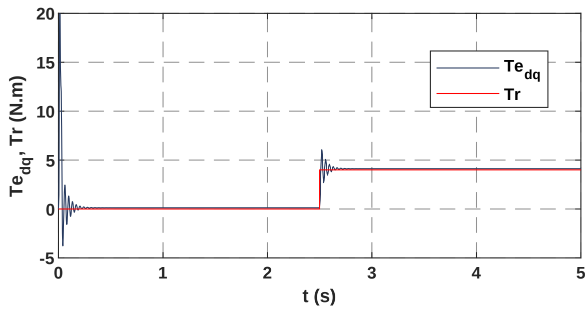

(e) Electromagnetic and load torques in dq frame

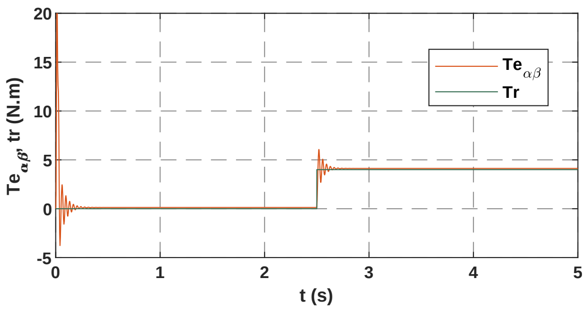

(f) Electromagnetic and load torques in $\alpha\beta$ frame

Fig 2.10. Simulation results of the IM model in the dq and $\alpha\beta$ reference frames.

Fig 2.10 summarizes the main results obtained from the simulations. Figures 2.10(a) and 2.10(b) show the evolution of the rotor speed for the dq and $\alpha\beta$ models, respectively. In both cases, the motor speed increases smoothly during the transient phase before reaching steady state, confirming the consistency of the mechanical model. When the load torque of 4 $\mathrm{N \cdot m}$ is applied at $t = 2.5$ s, the motor speed decreases slightly before stabilizing at the rated operating point, as expected.

Figures 2.10(c) and 2.10(d) illustrate the stator phase currents obtained from the two models. The current waveforms are nearly identical in amplitude and frequency, demonstrating that the electrical model behaves equivalently in both reference frames. A small transient oscillation is observed immediately after load application, which is typical of the torque disturbance response in induction motors.

Finally, Figures 2.10(e) and 2.10(f) present the electromagnetic torque (T_e) and the applied load torque (T_r) in both reference frames. The electromagnetic torque tracks the load torque with high fidelity, confirming that the model and the identified parameters accurately reproduce the motor's electromagnetic dynamics.

Overall, the results indicate a very good agreement between the dq and $\alpha\beta$ reference frame simulations. This consistency validates both the developed mathematical model and the parameters obtained through the identification procedures. Therefore, the implemented model can be confidently used in the subsequent control system design and performance evaluation stages.

2.4 Vehicle Dynamic Model

The dynamic behavior of an electric vehicle (EV) is governed by the interaction between the traction force generated by its powertrain and the various resistive forces that oppose motion. Developing an accurate vehicle dynamic model is therefore essential for control design, performance analysis, and energy optimization. This model establishes the relationship between the forces acting on the vehicle, its motion, and the corresponding mechanical power and torque requirements at the motor shaft.

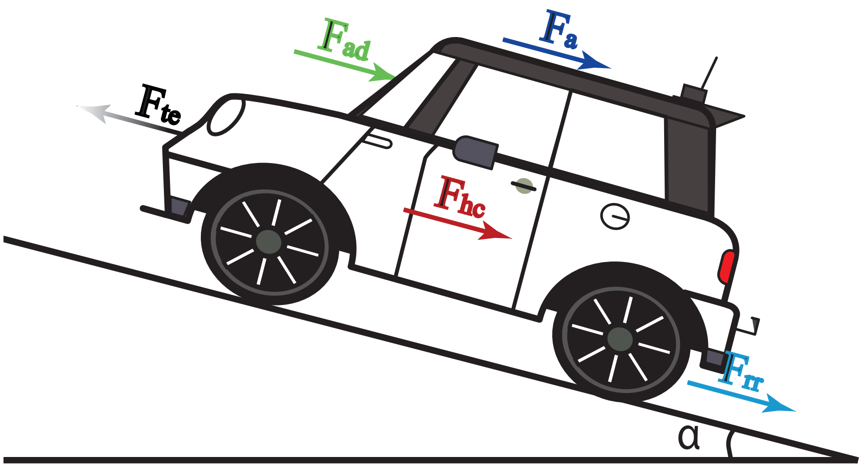

Fig 2.11. Types of forces applied to the vehicle.

As illustrated in Fig 2.11, the motion of the vehicle is primarily influenced by four forces: the rolling resistance force (F_{rr}), the hill climbing (grade) force (F_{hc}), the aerodynamic drag force (F_{ad}), and the acceleration (inertial) force (F_a). The combination of these forces determines the total tractive effort required for propulsion (F_{te}). Each of these forces can be described mathematically as follows [69].

2.4.1 Rolling Resistance Force

The rolling resistance force F_{rr} accounts for the losses caused by tire deformation and the friction between the tire and the road surface. It can be expressed as:

$$F_{rr} = K_r mg \tag{2.33}$$

where K_r is the tire rolling resistance coefficient, m is the total mass of the vehicle, and g is the gravitational acceleration. Typical values of K_r range between 0.008 and 0.015 for passenger cars on paved roads. Although small, rolling resistance significantly affects the vehicle's energy consumption during low-speed driving and urban operation.

2.4.2 Hill Climbing Force

When the vehicle moves on an inclined surface, a component of its weight acts along the direction of motion, opposing or assisting the vehicle depending on the slope angle. The hill climbing (or gradient) force is given by:

$$F_{hc} = mg\sin(\alpha) \tag{2.34}$$

where α is the slope angle. This force increases linearly with the road gradient and becomes dominant in mountainous terrain or steep roads.

2.4.3 Aerodynamic Drag Force

The aerodynamic drag F_{ad} represents the resistance due to air friction and pressure differentials acting on the vehicle body. It is expressed as:

$$F_{ad} = \frac{1}{2}\rho C_d A_s V^2 \tag{2.35}$$

where ρ is the air density, C_d is the aerodynamic drag coefficient, A_s is the frontal (projected) surface area, and V is the vehicle velocity. The drag coefficient typically ranges from 0.25 for modern EVs to 0.35 for conventional vehicles. Since F_{ad} increases quadratically with velocity, it becomes the dominant resistive force at high speeds.

2.4.4 Acceleration Force

The acceleration or inertial force F_a corresponds to the effort required to increase the vehicle speed. It is related to the equivalent mass M_e, which accounts for both translational and rotational inertias of the moving components (such as wheels, shafts, and the motor rotor):

$$\begin{aligned} F_a &= M_e a \\ M_e &= 1.04 + 0.0025 g_r^2 \end{aligned} \tag{2.36}$$

where a is the vehicle acceleration and g_r is the gear ratio. The factor M_e slightly increases the apparent mass of the vehicle to include the effect of rotating elements.

2.4.5 Total Tractive Effort and Vehicle Motion

The total tractive effort F_{te} required at the wheels to maintain or change the vehicle speed is obtained by summing all resistive and acceleration forces:

$$F_{te} = F_{ad} + F_{rr} + F_{hc} + F_a \tag{2.37}$$

Applying Newton's second law along the longitudinal axis of the vehicle, the motion equation can be expressed as:

$$m\frac{dV}{dt} = F_{te} - (F_{ad} + F_{rr} + F_{hc}) \tag{2.38}$$

At steady-state operation ($dV/dt = 0$), the traction force equals the sum of resistive forces, representing the equilibrium driving condition.

2.4.6 Powertrain Torque and Power Relations

The mechanical power developed by the traction motor P_m and the torque transmitted to the motor shaft T_r can be determined from the total tractive effort:

$$\begin{aligned} P_m &= \frac{1}{\eta} F_{te} V \\ T_r &= (F_{ad} + F_{rr} + F_{hc}) \frac{R}{g_r} \end{aligned} \tag{2.39}$$

where R is the wheel radius and η represents the overall drivetrain efficiency. These expressions establish the direct link between vehicle-level longitudinal dynamics and motor-level mechanical quantities, forming the foundation for powertrain control and energy management strategies.

2.4.7 Vehicle Parameters

The vehicle parameters listed in Table 2.5 were initially taken from [69], which were developed for a 1.1 kW electric motor. Since the motor used in this work has a lower rated power of 0.55 kW, some of the vehicle parameters were carefully adjusted to ensure compatibility with the reduced motor capacity. These adjustments include modifications to the vehicle mass, aerodynamic coefficients, and rolling resistance to ensure that the resulting motor speed, torque, and power remain within the operational limits of the selected motor. As a result, the vehicle model provides a realistic representation of the dynamic behavior of the vehicle under typical driving conditions, including acceleration, deceleration, and steady cruising. This carefully adapted model serves as a reliable foundation for subsequent simulation studies, allowing accurate evaluation of the electric drive performance and the design of effective motor control strategies.

Table 2.5. Vehicle parameters used in the dynamic model.

Parameter	Symbol	Unit	Value
Vehicle mass	m	80	kg
Wheel radius	R	0.23	m
Rolling resistance coefficient	K_r	0.015	/
Drag coefficient	C_d	0.2	/
Frontal surface area	A_s	0.6	m^2
Air density	ρ	1.2	kg/m^3
Gear ratio	g_r	2	/
Drivetrain efficiency	η	0.95	/

2.4.8 Vehicle Model Validation

To validate the accuracy of the proposed vehicle model, a simulation was performed using Matlab/Simulink. The simulation block diagram of the vehicle model is shown in Fig 2.12. This setup allows the analysis of the vehicle's dynamic response under various driving conditions.

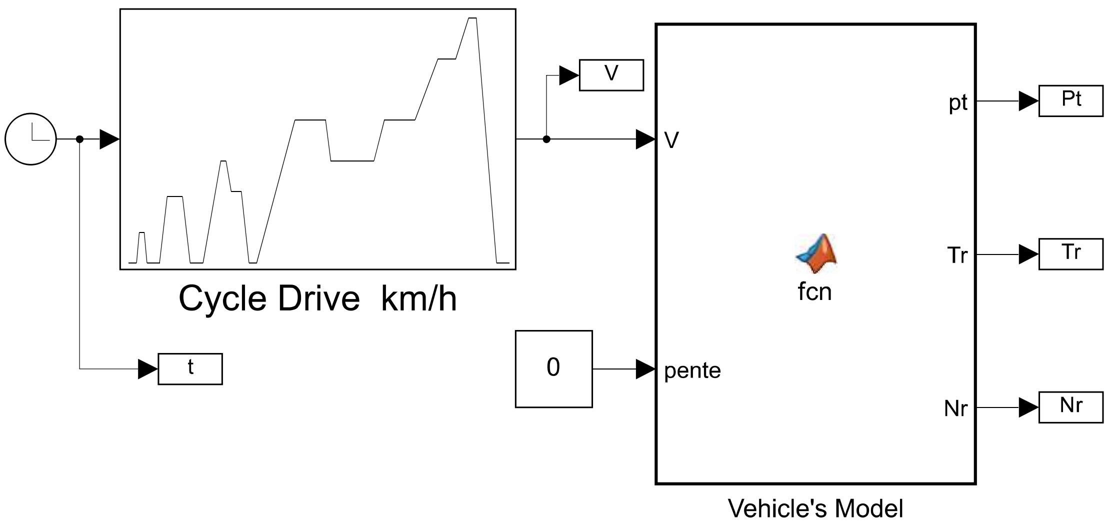

Fig 2.12. Simulink implementation of the vehicle model.

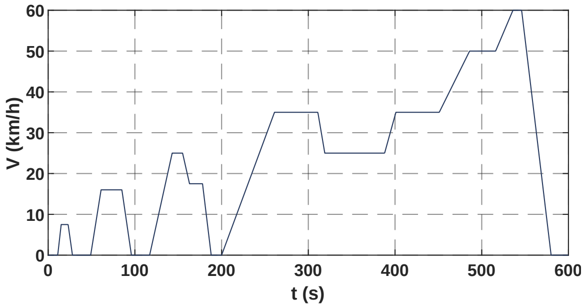

(a) Vehicle speed V

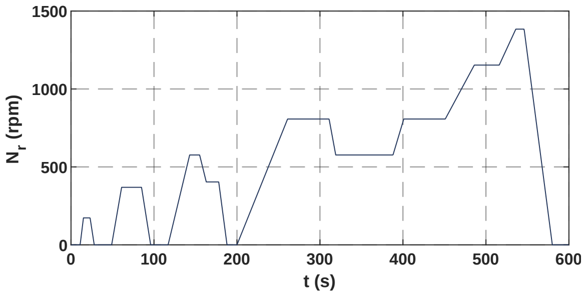

(b) Motor speed Nr

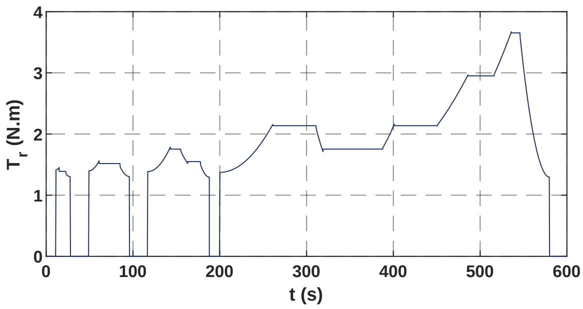

(c) Torque applied to the motor Tr

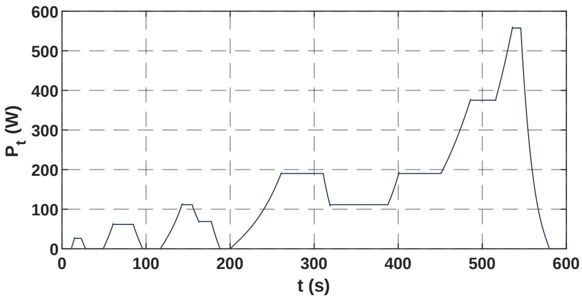

(d) Mechanical power required from the motor Pt

Fig 2.13. Simulation results of the vehicle model.

The simulation results, presented in Fig 2.13, show the vehicle speed V, motor speed Nr, torque applied to the motor Tr, and mechanical power required from the motor Pt. These results confirm that the vehicle model is properly aligned with the selected motor parameters: the maximum motor power is limited to 0.55 kW, the maximum motor speed reaches 1390 rpm, and the peak torque is 3.77 $N{\cdot}m$, while the vehicle achieves a maximum speed of 60 km/h. This demonstrates that the model provides a realistic representation of the vehicle's dynamic behavior within the operational limits of the motor, ensuring accurate evaluation of the electric drive performance under the intended driving conditions.

Conclusion

This chapter presented the complete modeling and validation of the main components of the electric vehicle powertrain. It began with the detailed modeling of the induction motor in both the stationary ($\alpha\beta$) and rotating (dq) reference frames. The mathematical equations were derived using the Clarke and Park transformations, providing a clear description of the electromagnetic and mechanical dynamics of the machine. These models constitute the analytical foundation for the control strategies developed in the subsequent chapters.

The parameters of the induction motor were then identified using two complementary methods: the classical approach based on standard experimental tests and the identification process integrated in the Abb variable-speed drive. The results obtained from both methods showed close agreement, confirming the accuracy and consistency of the identified parameters.

To validate the modeling and identification results, a simulation study was conducted using Matlab/Simulink. The two models (dq and $\alpha\beta$) were supplied with the same nominal voltage and subjected to a load torque variation. The results demonstrated excellent correspondence between both reference frames in terms of speed, current, and torque evolution, which validates the developed mathematical models and the identified parameters.

Finally, the vehicle dynamic model was established to describe the longitudinal motion of the electric vehicle. The model takes into account the main resistive forces acting on the vehicle, including rolling resistance, aerodynamic drag, and the slope component of gravitational force. The dynamic equations were implemented and validated by simulation in Matlab/Simulink, confirming that the vehicle's acceleration and speed responses are consistent with theoretical expectations.

In conclusion, this chapter provided a validated representation of both the electrical and mechanical subsystems of the electric vehicle. The developed models form a solid basis for the design and implementation of advanced control strategies, which will be addressed in the next chapter.

Chapter 3

Sensorless Scalar Control Using SOGI-FLL Estimator

3.1 Introduction

THIS chapter introduces the basic Second-Order Generalized Integrator (SOGI) and Frequency-Locked Loop (FLL), along with integration for speed estimation of the induction motor. This estimation techniques is widely used in various power and control systems, particularly in applications involving synchronization, signal extraction, and frequency tracking.

the classical Phase-Locked Loop (PLL) is a fundamental tool in control systems, designed to synchronize with the phase and frequency of a periodic input signal. It has been extensively used in grid-connected converters and communication systems due to its simplicity and effectiveness [70, 71]. However, PLLs can suffer from performance issues under conditions such as DC offset, harmonics, or unbalanced voltages [72].

To overcome these limitations, the SOGI-FLL structure has emerged as a robust alternative. The SOGI acts as a resonant filter that separates the input signal into in-phase and quadrature components, while the FLL dynamically estimates the signal frequency [73, 74]. Unlike PLLs, the SOGI-FLL can maintain stable and accurate tracking even under distorted grid conditions or frequency variations [75].

SOGI-FLL has proven especially useful in grid-connected systems and microgrids, where precise phase and frequency detection are critical. For instance, in photovoltaic (PV) or wind systems, it is used to extract the grid voltage phase for inverter synchronization [76, 77]. It also enables accurate signal reconstruction in single-phase systems, supporting power quality monitoring and fault detection [74, 78].

Most of the existing literature focuses on the use of SOGI-FLL in these power electronics and grid-related applications. However, its application to induction motor control, particularly under scalar (V/f) control, remains largely unexplored. Scalar control is widely adopted for its simplicity and cost-effectiveness, but lacks the dynamic performance and accuracy found in vector control methods [79].

This chapter proposes a novel contribution by integrating the basic SOGI-FLL structure into a scalar-controlled induction motor system, with the aim of estimating rotor speed sensorlessly using only one current sensor. This approach leverages the simplicity of scalar control while adding the robustness and signal processing capabilities of SOGI-FLL. The technique is validated through simulation and experimental results, demonstrating its feasibility in real-time motor drive systems.

3.2 Scalar Control of IM

Scalar control is one of the earliest and most commonly used methods for controlling induction motors. It is based on the control of scalar quantities such as voltage, frequency, and current, rather than vector quantities like flux and torque. This approach does not require complex coordinate transformations or real-time feedback of rotor position, making it a straightforward and easy-to-implement solution for many applications [80, 81]. Although it does not offer the high dynamic performance of more advanced methods like vector control, scalar control remains effective for a wide range of systems where simplicity and reliability are preferred [82]. The most widely adopted form of scalar control is the voltage-to-frequency (V/f) method, which maintains an appropriate relationship between the stator voltage and supply frequency to achieve acceptable motor performance [83].

3.2.1 Principle of V/f Control

The principle of scalar control is based on maintaining a constant ratio between the stator voltage and the supply frequency (V/f), which ensures that the magnetic flux in the motor remains approximately constant. This control method adjusts the supply frequency and voltage simultaneously to regulate the motor speed without requiring rotor position feedback. It is generally implemented using an open-loop or closed-loop configuration, where frequency is determined based on the desired speed and voltage is adjusted accordingly [80]. The block diagram typically includes a speed reference, a frequency generator, a voltage generator using the V/f law, and a pulse-width modulation (PWM) inverter for supplying the motor [81, 84].

The scalar control method regulates the magnitude and frequency of the supply voltage

(v_s) to maintain a constant V/f ratio, ensuring constant magnetic flux in the motor. The basic principle can be expressed as:

$$|\phi| = \frac{v_s}{f} = \text{constant} \tag{3.1}$$

This ensures that the magnetic flux $|\phi|$ remains constant, preventing saturation and torque instability. on the other hand, the electromagnetic torque and speed can be expressed as follows:

$$T_e = \frac{3}{2} P \frac{M}{L_r} (i_{dr} i_{qs} - i_{qr} i_{ds}) \tag{3.2}$$

$$\Omega_r = (T_e - T_r) \frac{1}{Js + C_f} \tag{3.3}$$

such as:

T_e is the electromagnetic torque, P is the number of pole pairs, Ω_r is the rotor speed, T_r is the load torque, J is the moment of inertia, C_f is the coefficient of friction, and s is the Laplace operator.

The regulator is of type PI makes it possible to estimate the value of the reference slip speed ω_{sl}^*. Also, we can get the stator speed pulsation ω_s^* by adding the estimated rotor speed pulsation $\omega_{r_{est}}$ to ω_{sl}^* us follow:

$$\omega_s^* = \omega_{r_{est}} + \omega_{sl}^* \tag{3.4}$$

In the following equation we note that the voltage V_s is the same whatever is the reference considered.

$$\bar{V_s} = R_s \bar{i_s} + j\omega_s \bar{\Phi}_s \tag{3.5}$$

where i_s represent the stator current, R_s is the phase stator resistance. To keep the flux constant, the voltage V_s efficiency must be proportional to the supply frequency of the stator f_s , at high speed $R_s i_s$ is too small compared to ω_s, so we can write as follows:

$$\Phi_s = \frac{v_s}{\omega_s} = \frac{v_s}{2\pi f_s} \tag{3.6}$$

However, this relation is not valid for low value of the pulsation ω_s, because the voltage drop $R_s i_s$ due to the resistance of the stator windings is no longer negligible compared to the term $\omega_s \Phi_s$. the diagram block of scalar control is presented in Fig. 3.1.

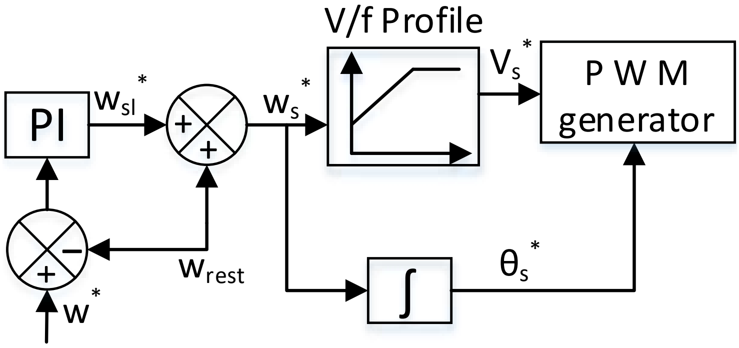

Fig 3.1. Scalar control block

3.3 SOGI-FLL Estimator

The Second-Order Generalized Integrator with Frequency-Locked Loop (Sogi-Fll) is a widely recognized signal processing structure initially developed for applications in grid synchronization and power system monitoring [85, 86]. In such systems, the accurate estimation of signal frequency, amplitude, and phase is essential for tasks like phase-locked control, fault detection, and grid-tied inverter synchronization [87]. The Sogi component serves as a resonant filter that can extract the fundamental component of an input signal and generate its orthogonal counterpart in real time. This allows for the decomposition of grid voltages or currents into in-phase and quadrature signals, which are crucial for phase and frequency tracking [86, 88].

The Frequency-Locked Loop (Fll) complements the Sogi by providing a dynamic adjustment mechanism that continuously tracks the frequency of the input signal. Unlike the traditional Phase-Locked Loop (Pll), the Fll is particularly robust in the presence of frequency variations and harmonics, making it suitable for distorted or unbalanced grid conditions [89]. The combination of Sogi and Fll results in a system that is both fast and accurate, with relatively low computational requirements. Due to these advantages, the Sogi-Fll has become a popular choice in control and measurement systems within the field of electrical power engineering [90].

In this work, the Sogi-Fll estimator is applied for the purpose of estimating the rotor speed of an induction motor within a scalar control framework. Unlike conventional approaches that rely on mechanical sensors or multiple electrical measurements, the proposed method utilizes only a single-phase stator current measurement. The Sogi-Fll is employed to extract the fundamental frequency component of the measured current signal, from which the motor's synchronous frequency can be inferred. This estimated frequency is then used to indirectly determine the rotor speed, enabling a sensorless control scheme that maintains the simplicity of scalar control while eliminating the need for physical speed sensors. The overall objective is to develop a cost-effective and reliable solution for speed estimation that preserves ease of implementation and remains suitable for applications with moderate performance requirements.

Fig. 3.2 represent the Sogi-Fll method, where the closed loop transfer functions of the output signals is given by [91]:

$$F_\alpha(s) = \frac{k\omega_{s_{est}} s}{s^2 + k\omega_{s_{est}} s + \omega_{s_{est}}^2} \tag{3.7}$$

$$F_\beta(s) = \frac{k\omega_{s_{est}}^2}{s^2 + k\omega_{s_{est}} s + \omega_{s_{est}}^2} \tag{3.8}$$

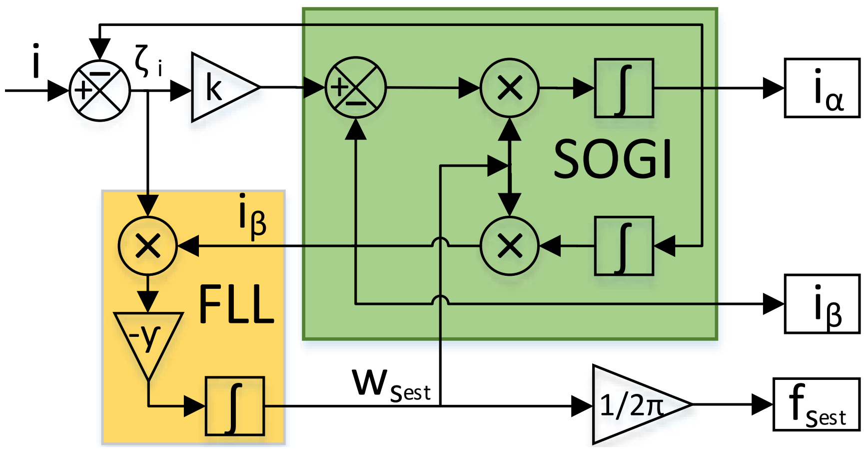

Fig 3.2. Sogi-Fll diagram

The principle of Sogi diagram described in Fig. 3.2 on green, is to generate two output signals; the in-phase (i_α) and the in-quadrature (i_β), where i_β is always 90° lagged from i_α. However, this method can't estimate the frequency directly [92]. So we need the Fll approach, which is described in Fig. 3.2 on yellow, where his principle is to estimate the frequency ($\omega_{s_{est}}$) of the current i by multiplying the error (ζ_i) between the input signal (i) and the in-phase (i_α) by the in-quadrature signal (i_β), and then amplified the resulting by the factor ($-\gamma$), where γ it's a constant gain given by [93, 94]:

$$\gamma = \frac{k\omega_{s_{est}}}{i_{\alpha\beta}^2}\Gamma \tag{3.9}$$

where, k and Γ are constants; k=0.4, Γ=40, $i_{\alpha\beta}$ is the amplitude of current given by:

$$i_{\alpha\beta} = \sqrt{i_\alpha^2 + i_\beta^2} \tag{3.10}$$

3.4 Integration of SOGI-FLL into Scalar Control

To enhance the performance of conventional scalar control, particularly in variable-frequency applications and sensorless scenarios, the integration of the SOGI-FLL estimator becomes essential. Having previously detailed the principles of scalar control and the operation of the SOGI-FLL, this section presents the methodology adopted to combine both techniques in a unified control scheme. The SOGI-FLL is employed here to provide a real-time and accurate estimation of the supply frequency, which replaces the fixed reference frequency typically used in open-loop scalar control. This dynamic estimation allows for better adaptation to input variations, improving both the robustness and dynamic response of the drive system. In the following, we detail the integration strategy through the mathematical formulations and present the corresponding global block diagram.

The control strategie is shown in Fig. 3.3. as shown the estimated frequency from the SOGI-FLL replaces the sensor-based speed feedback. The control loop is closed using this estimated value to regulate the V/f ratio.

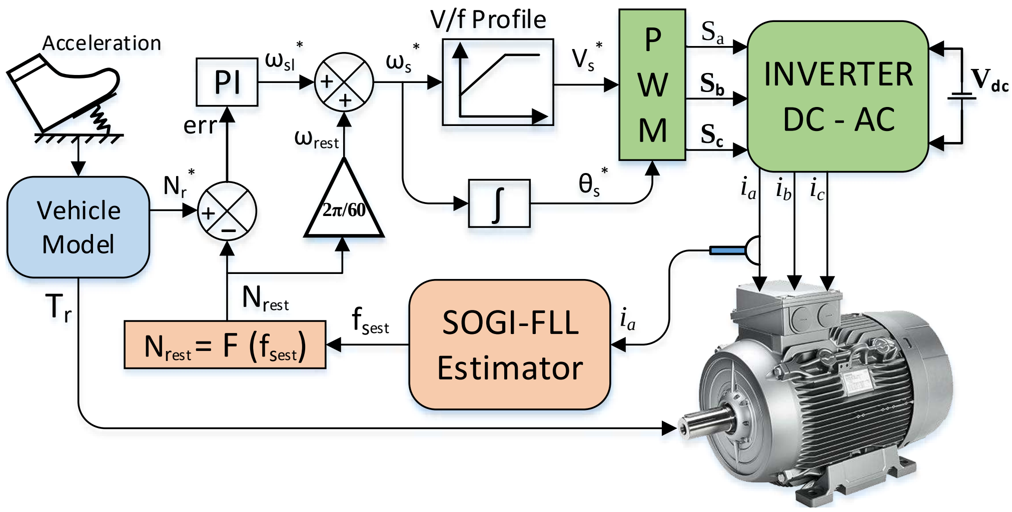

Fig 3.3. Schematic diagram of the IM system with the controller-based SOGI-FLL method

Equation (3.11) illustrates the method used to estimate the rotor speed of the induction motor based on the output of the SOGI-FLL estimator. By extracting the fundamental frequency component from the stator current, the synchronous frequency is determined. This value is then used to calculate the motor's estimated speed, enabling a sensorless control approach. This method offers a simple yet effective alternative to mechanical speed sensors. the estimated speed N_{rest} is given by:

$$N_{rest} = \frac{(1-s)(60 f_{s_{est}})}{p} \tag{3.11}$$

Where $f_{s_{est}}$ is the estimated frequency of the current, s represents the motor slip, and p is a number of pole pairs.

In scalar control, the induction motor typically operates at high speeds where the difference between the synchronous speed and the rotor speed becomes minimal. As a result, the slip s, which represents the relative difference between these two speeds, approaches zeros. To simplify the control strategy and avoid the need for real-time slip computation, a fixed slip value is assumed. In this work, a constant slip of $s = 0.98$ is used as an approximation, which reflects a typical operating condition for high-speed induction motor applications under scalar control.

The estimated rotor speed is obtained using (3.11). It is important to note that the Sogi-Fll algorithm provides frequency estimation only for the positive direction of motor rotation. To enable operation in the reverse direction, an effective solution is implemented by incorporating a Sign block in Matlab. This block determines the sign of the reference speed, allowing the control system to correctly handle bidirectional motor operation.

3.5 Stability Analysis and Robustness Assessment

This section presents the stability evaluation of the proposed system, which serves as the basis for selecting appropriate gains for the PI speed controller. Additionally, the controller's robustness is analyzed under variations in key system parameters.

3.5.1 Stability Analysis

As illustrated in Fig 3.4, the block diagram represents the simplified closed-loop configuration, comprising the induction motor (Im) model, the transfer function of the Fll estimator, and the pi controller. Using this structure, the closed-loop transfer function governing the speed control loop is formulated as follows:

$$G_{s_{cl}} = \frac{N_r^*}{N_{r_{est}}} = \frac{G_p \cdot G_m}{1 + G_p \cdot G_m \cdot G_f} \tag{3.12}$$

Here, G_m denotes the Im transfer function, G_p is the pi controller, and G_f represents the simplified dynamic model of the Fll estimator used for frequency detection. These are expressed as:

$$G_m = \tfrac{1}{Js+C_f} \quad ; \quad G_f = \tfrac{\Gamma}{s+\Gamma} \quad ; \quad G_p = k_p + \tfrac{k_i}{s}$$

By combining (3.12) and (3.5.1), the complete closed-loop transfer function is given by:

$$G_{s_{cl}} = \frac{(k_p s + k_i)(s + \Gamma)}{(Js^2 + C_f s)(s + \Gamma) + (k_p s + k_i)\Gamma} \tag{3.13}$$

The location of the poles for this closed-loop system, derived from (3.13), was analyzed using MATLAB across varying values of the PI gains k_p and k_i. The plots in Fig. 3.5 confirm system stability under the following conditions:

- For $k_i = 0.0001$, the system remains stable across $0.001 < k_p < 10$.
- For $k_p = 0.0024$, stability is guaranteed when $k_i < 0.162$.

Therefore, the controller parameters were selected as $k_p = 0.0024$ and $k_i = 0.0001$ to ensure stability.

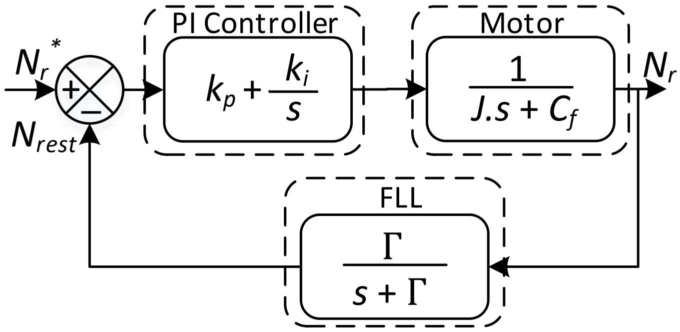

Fig 3.4. Simplified closed-loop configuration of the IM drive.

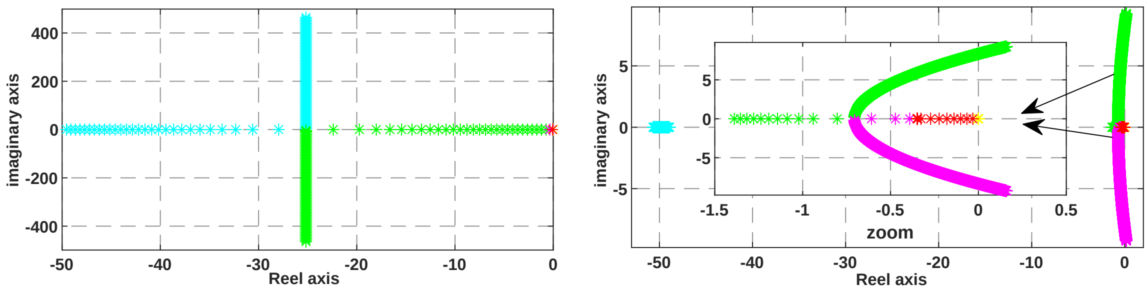

(a) $k_i = 0.0001$; $0.001 < k_p < 10$ (b) $k_p = 0.0024$; $0.0001 < k_i < 0.2$

Fig 3.5. Pole trajectories for variations in k_p and k_i.

3.5.2 Robustness Assessment

To evaluate the robustness of the selected controller, the system's closed-loop behavior described by (3.13) was examined under different values of the inertia J and friction coefficient C_f. The analysis, performed using MATLAB, utilized the selected parameters $k_p = 0.0024$, $k_i = 0.0001$, and $\Gamma = 50$. The simulation results are shown in Fig. 3.6. The analysis reveals that for all tested values of J and C_f, the system maintains stability when the controller gains are fixed at $k_p = 0.0024$ and $k_i = 0.0001$, demonstrating robust performance despite parameter uncertainties.

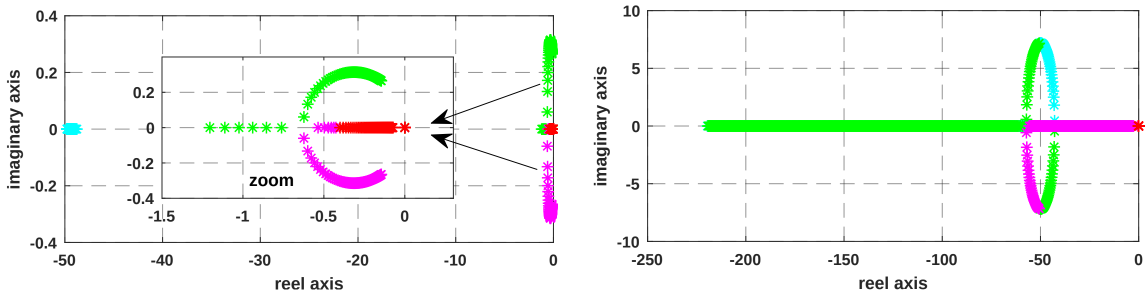

(a) $C_f = 0.0008$; $0.001 < J < 0.01$ (b) $J = 0.0023$; $0.005 < C_f < 0.5$

Fig 3.6. Pole behavior under varying J and C_f values.

3.6 Results and Discussion

This section presents the results obtained from both simulation and experimental evaluations of the proposed sensorless scalar control strategy for the induction motor using the SOGI-FLL estimator. The primary objective is to assess the performance of the control scheme in estimating motor speed and maintaining stable operation using only a single stator current sensor.

The simulation results were carried out using MATLAB/SIMULINK to validate the theoretical framework and verify the effectiveness of the control algorithm under various operating conditions. These results provide initial insights into the behavior of the system in a controlled, noise-free environment.

Following the simulations, experimental results obtained from a laboratory test bench are presented. These tests were conducted to validate the practical applicability of the proposed method in a real-time environment, where non-idealities such as measurement noise, switching effects, and hardware limitations are present. A comparative discussion highlights the consistency and differences observed between the simulation and experimental outcomes.

3.6.1 Simulation Results

This part presents the simulation results generated using MATLAB/SIMULINK. The simulation model incorporates the induction motor, scalar control loop, and the SOGI-FLL estimator for frequency and speed estimation. The system was tested under different operating conditions, including three tests as shown below:

3.6.1.1 the first test (reverse the speed direction)

Fig. 3.7 Shows the simulation results of this test which is for reversing the motor direction, where the reference speed scenario is as bellow:

- if $t \in [0, 3]s \Rightarrow N_r^* = 1000\ rpm$.
- if $t \in [3, 6]s \Rightarrow N_r^* = -1000\ rpm$.

From Fig. 3.7(a), we observe that the motor speed accurately follows its reference signal, indicating good dynamic behavior. Similarly, in Fig. 3.7(b), the stator current (i_a) shows a high value during the reversal process, with a longer rise time due to the extended transitional regime. This behavior is expected when the motor undergoes a directional change. As shown in Fig. 3.7(c), the electromagnetic torque (T_e) follows the same pattern as the current, which confirms that the torque is proportional to a phase stator current (i_a) in this operating mode.

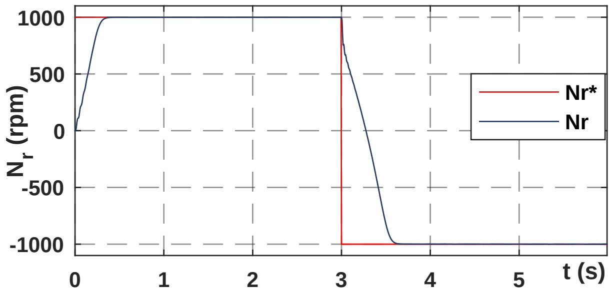

(a) Motor speed N_r

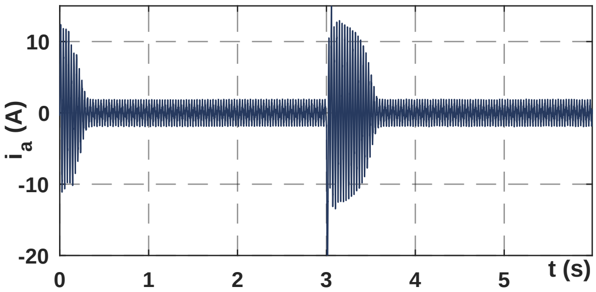

(b) Current i_a

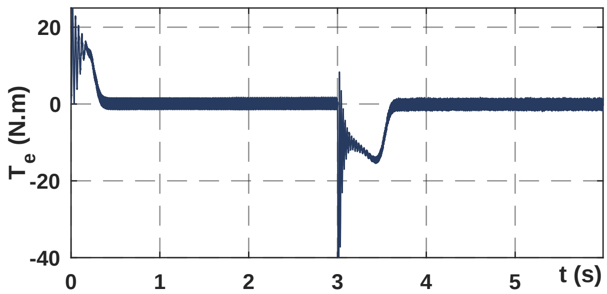

(c) Electromagnetic torque T_e

Fig 3.7. Reverse speed direction test

3.6.1.2 the second test (variable speed)

In this test, the motor's response is evaluated by applying a sequence of varying reference speed values. This scenario is designed to assess the system's ability to follow dynamic speed changes. The reference profile includes multiple levels to simulate realistic operating conditions. The corresponding simulation results are presented in Fig. 3.8, illustrating the motor's tracking performance.

- if $t \in [0, 2]s \Rightarrow N_r^* = 1200\ rpm$.
- if $t \in [2, 4]s \Rightarrow N_r^* = 1400\ rpm$.
- if $t \in [4, 6]s \Rightarrow N_r^* = 1000\ rpm$.

In Fig. 3.8(a), the motor speed precisely tracks the reference across varying conditions, demonstrating effective control under speed profiling. The estimated frequency ($f_{s_{est}}$), shown in Fig. 3.8(b), also follows its reference accurately, validating the performance of the SOGI-FLL estimator in this scenario. As illustrated in Fig. 3.8(d), the current i_a reaches approximately twice the rated value during start-up ($ia \approx 2In$), and transient peaks are observed each time the reference speed changes. The electromagnetic torque (T_e), presented in Fig. 3.8(e), follows these current variations accordingly.

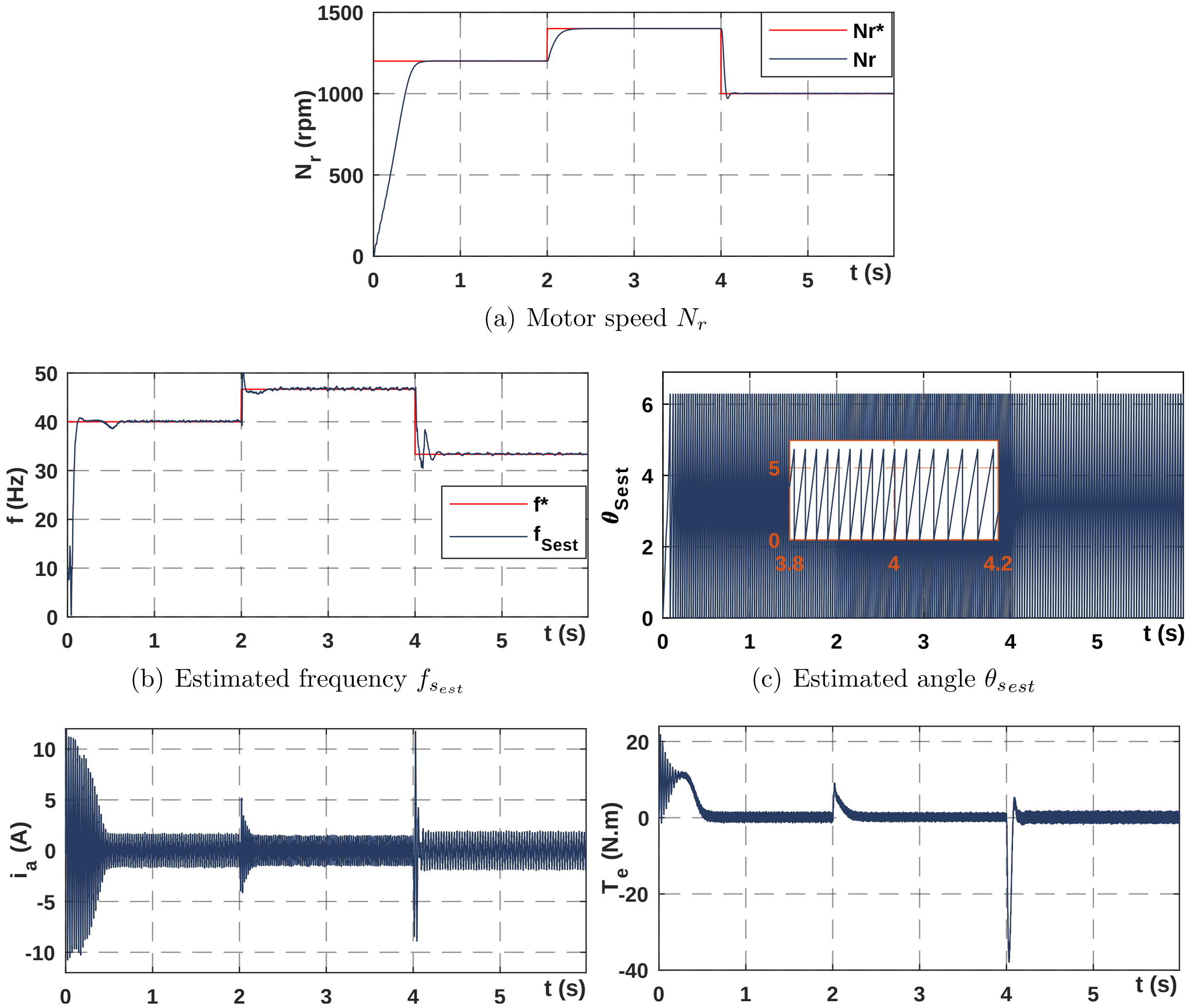

(a) Motor speed N_r

(b) Estimated frequency $f_{s_{est}}$

(c) Estimated angle θ_{sest}

(d) Current i_a

(e) Electromagnetic torque T_e

Fig 3.8. Experimental results of the IM under variable-speed operation

3.6.1.3 the third test (Vehicle dynamics application)

In this test, we applied vehicle dynamics to the motor; by using the cycle drive shown in Fig. 3.9(a), and the load torque applied by the vehicle to the motor, which is represented in Fig3.9(c). The simulation results of this test are shown in Fig. 3.9.

Fig. 3.9(e) and 3.9(d) present the electromagnetic torque T_e and the stator current i_a, respectively. Both variables exhibit variations over time, responding to changes in the load torque. This dynamic behavior aligns with the expected response since the electromagnetic torque is directly proportional to the motor current.

The load torque (Tr) applied in this test is illustrated in Fig. 3.9(c), where its changes correlate with the variations in T_e and i_a. This confirms that the control system responds appropriately to load disturbances by adapting the current and torque accordingly.

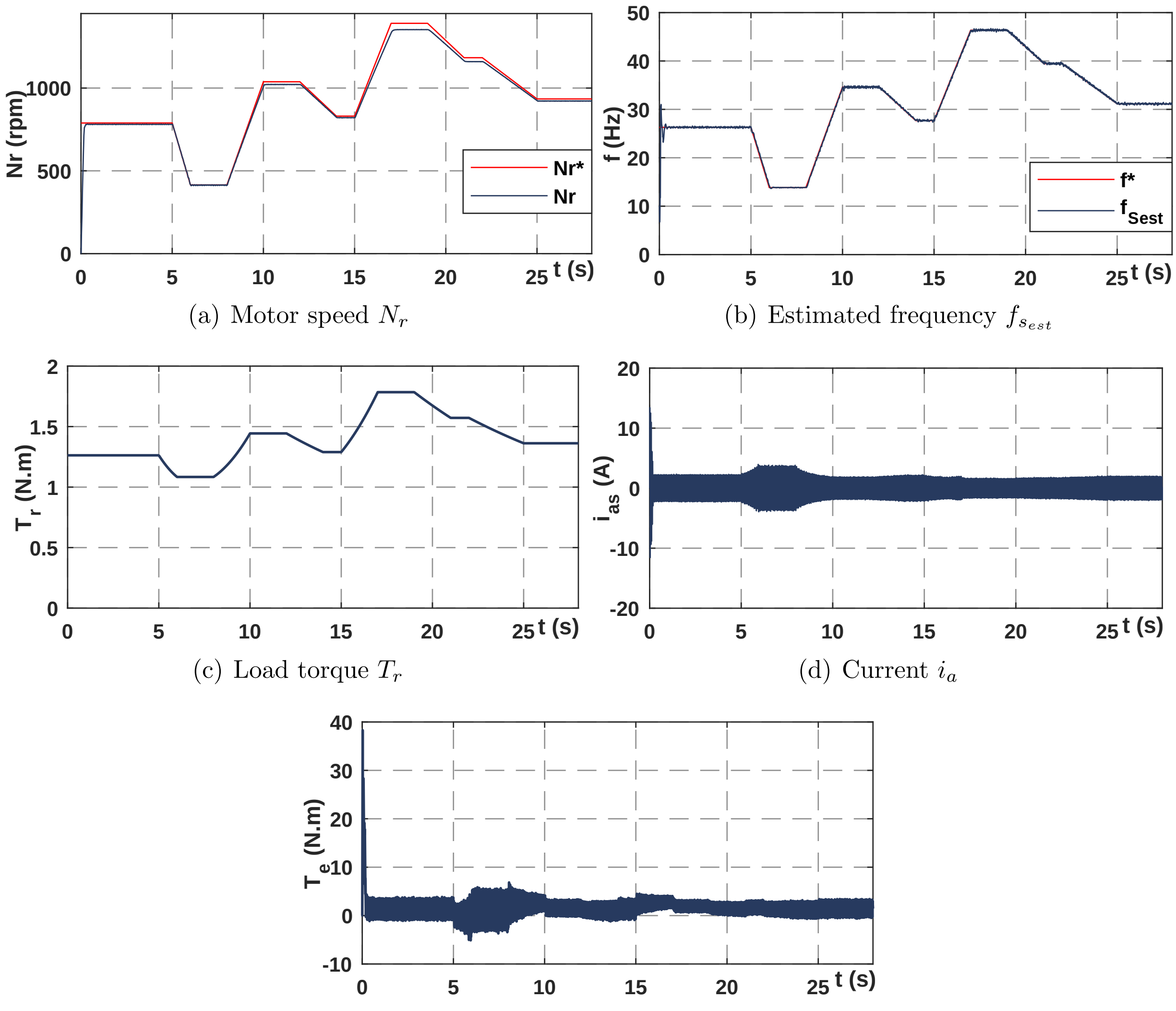

(a) Motor speed N_r

(b) Estimated frequency $f_{s_{est}}$

(c) Load torque T_r

(d) Current i_a

(e) Electromagnetic torque T_e

Fig 3.9. Vehicle dynamics application test

3.6.2 Experimental Results

In this part, the experimental validation of the proposed control strategy is presented. The experimental results were obtained based on dSPACE MicroLabBox, by using the test bench shown in Fig. 3.10, which consists of:

- three-phase induction motor.
- dSPACE MicroLabBox, DS1202 with control desk software.
- Powder brake with torque control unit.
- Semikron inverter composed of IGBT, and a rectifier.
- Incremental encoder speed sensor, DC 5V-24V 4096 P/R.
- adaptation and isolation card (5V-15V).
- current sensors based on LA 55-P.
- DC power supply 15V.

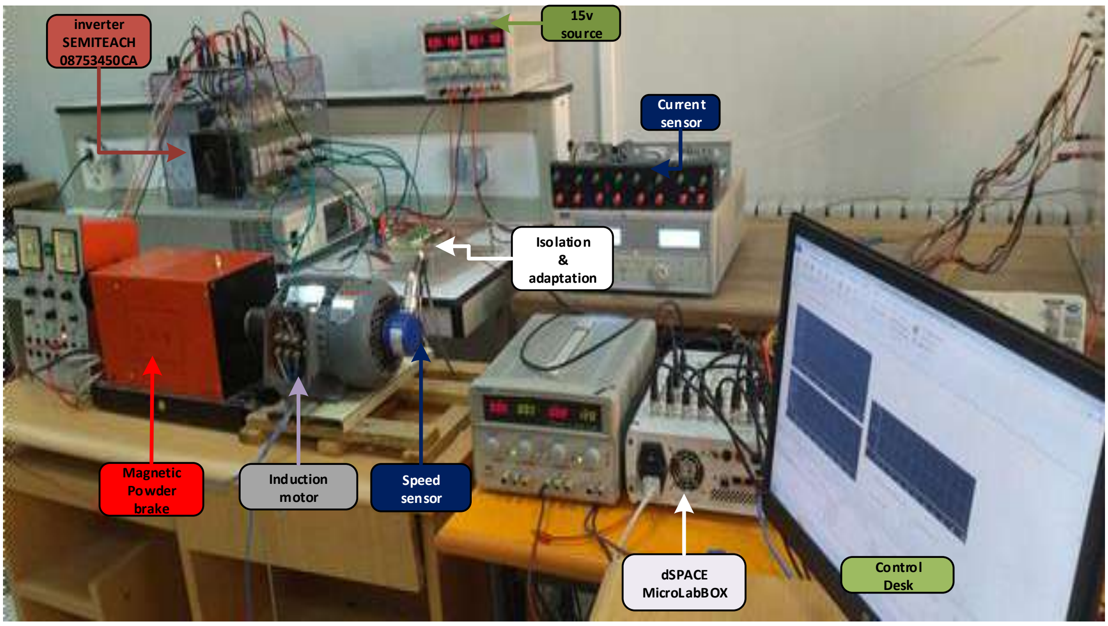

Fig 3.10. Experiment prototype for laboratory

The experiment results data have been registered using Control Desk software, and plotted using MATLAB. Where the effectiveness, robustness, and quality study of the proposed control are based on fort tests applied to the induction motor as follows:

- variable speeds test.
- reverse speed direction test.
- EV cycle test.
- Reduced-speed operation test.

3.6.2.1 Variable Speeds Test

In this test, the rotor speed N_r shown in Fig. 3.11(a) closely tracks the reference speed trajectory, which includes multiple variations, demonstrating the ability of the scalar control combined with the SOGI-FLL estimator to manage dynamic conditions effectively. As observed in Fig. 3.11(b), the estimated stator frequency $f_{s_{est}}$ follows the changes without introducing oscillations or steady-state errors, confirming the robustness of the FLL. The estimated angle $\theta_{s_{est}}$, presented in Fig. 3.11(c), evolves smoothly and continuously, even during rapid speed transitions, indicating accurate phase estimation. Fig. 3.11(d) displays the stator phase current i_a, which remains sinusoidal and stable throughout the test. A detailed view in Fig. 3.11(e) confirms that the current waveform retains a clean and regular profile, free of high-frequency noise or distortions. Overall, the results validate the reliability and dynamic response of the proposed control under variable speed conditions.

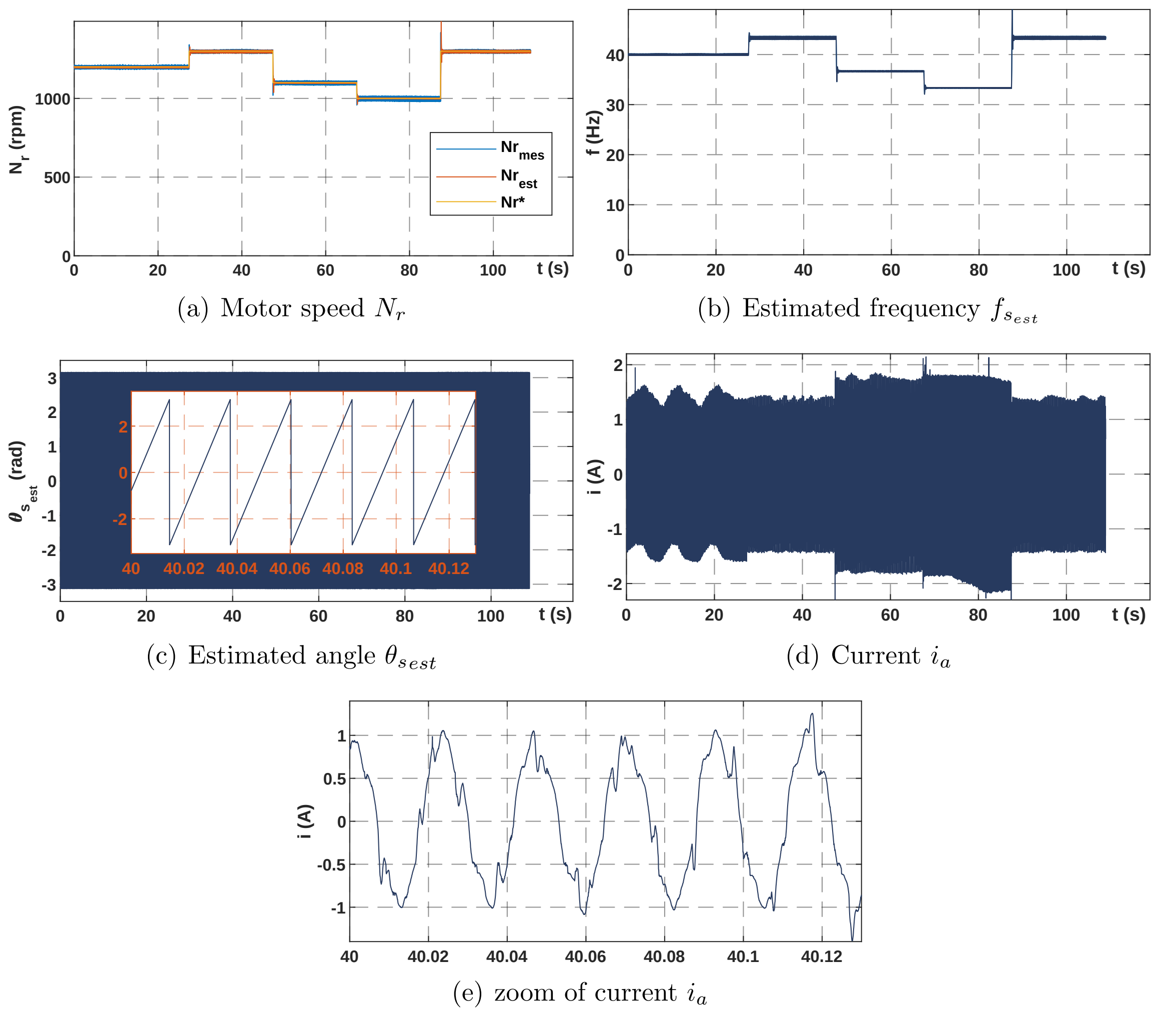

(a) Motor speed N_r

(b) Estimated frequency $f_{s_{est}}$

(c) Estimated angle θ_{sest}

(d) Current i_a

(e) zoom of current i_a

Fig 3.11. Variable Speeds Test

3.6.2.2 reverse Speed Test

The reverse speed test evaluates the system's performance during direction change. As illustrated in Fig. 3.12(a), the motor speed N_r transitions through zero and achieves the negative speed setpoint without oscillations or instability, showcasing the system's robustness during reversal. The estimated frequency $f_{s_{est}}$ in Fig. 3.12(b) properly reflects the change in direction, maintaining a continuous and symmetrical behavior. Fig. 3.12(c) shows the angle $\theta_{s_{est}}$ evolving steadily in the opposite direction after reversal, which confirms that the SOGI-FLL maintains synchronization even during sign changes. The stator current i_a in Fig. 3.12(d) remains stable and symmetrical throughout the process, and the zoomed-in waveform in Fig. 3.12(e) indicates a smooth and noise-free reversal. These results demonstrate that the proposed control scheme can effectively handle bidirectional operation with consistent performance.

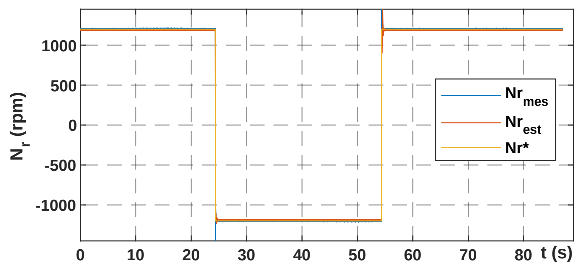

(a) Motor speed N_r

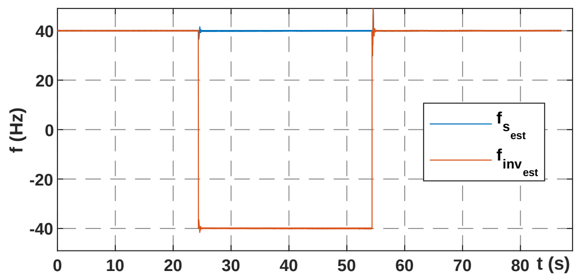

(b) Estimated frequency $f_{s_{est}}$

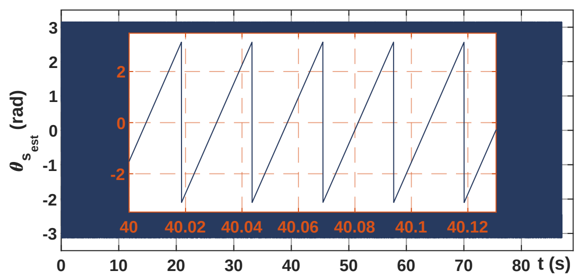

(c) Estimated angle $\theta_{s_{est}}$

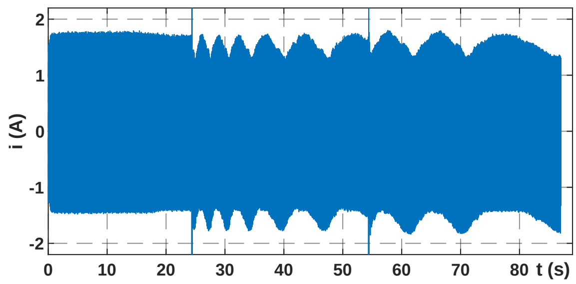

(d) Current i_a

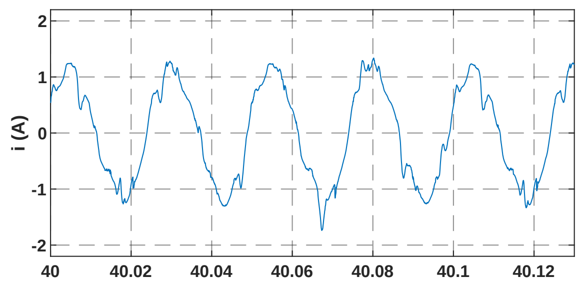

(e) zoom of current i_a

Fig 3.12. reverse Speed Test

3.6.2.3 EV Cycle Drive Test

This test simulates a real electric vehicle driving profile. In Fig. 3.13(a), the rotor speed N_r follows a complex time-varying reference, typical of acceleration and deceleration phases seen in EV operation. The estimated frequency $f_{s_{est}}$, depicted in Fig. 3.13(b), adapts well to the changing speed, maintaining accurate tracking without instability. The angle $\theta_{s_{est}}$ in Fig. 3.13(c) remains smooth and continuous, confirming precise phase tracking even under frequent dynamic changes. Fig. 3.13(d) shows that the stator current i_a remains sinusoidal throughout the driving cycle, while the zoomed-in view in Fig. 3.13(e) highlights the quality of the current waveform under variable load conditions. Furthermore, Fig. 3.13(f) presents the load torque (T_r) illustrates a realistic torque variation, which is well-managed by the control system without degradation in performance. These results validate the proposed method's suitability for high speeds EV that require rapid speed and torque changes.

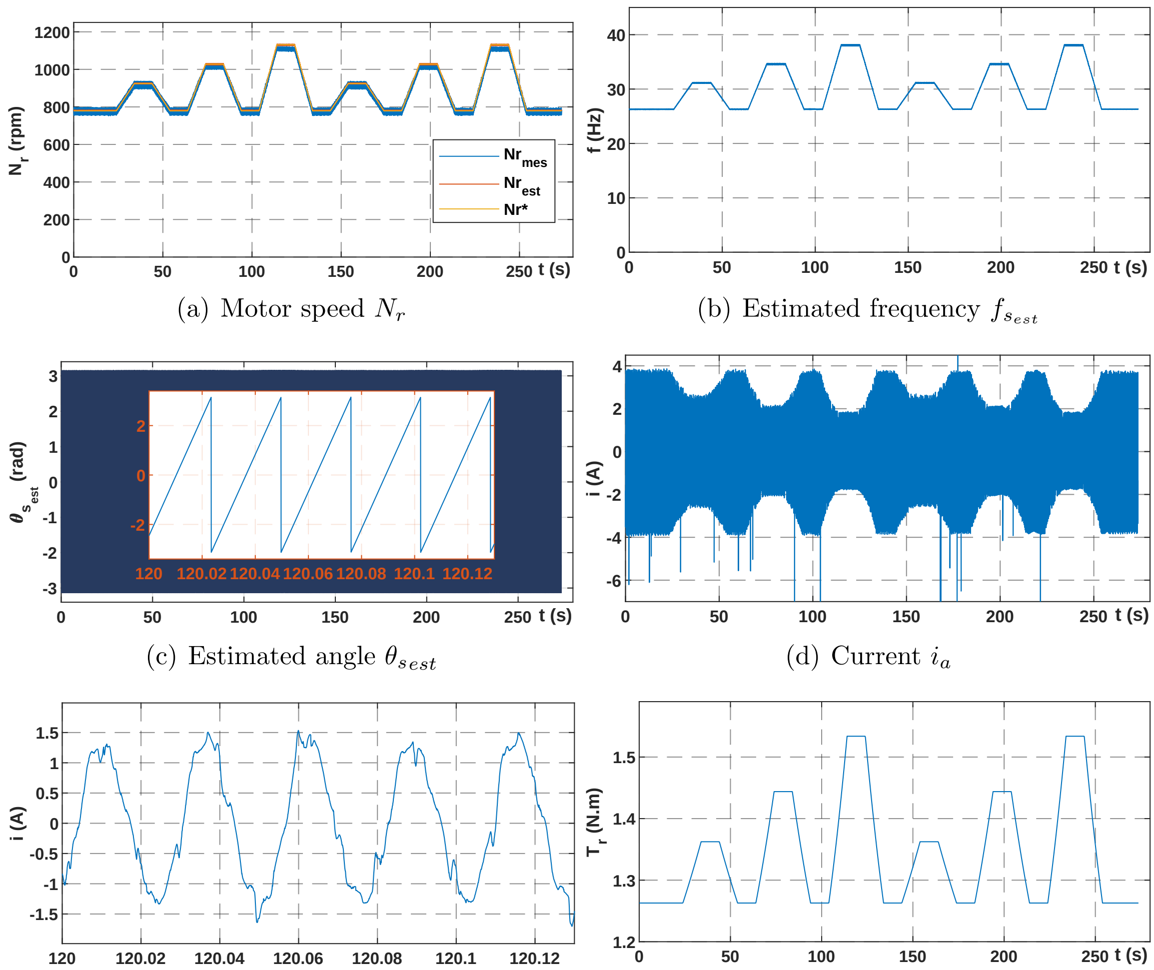

(a) Motor speed N_r

(b) Estimated frequency $f_{s_{est}}$

(c) Estimated angle $\theta_{s_{est}}$

(d) Current i_a

(e) Zoom of phase current (i_a)

(f) Load Torque T_r

Fig 3.13. EV cycle drive Test

3.6.2.4 Reduced-speed operation test

The reduced-speed test evaluates the system behavior as the speed is decreased from 1000 rpm, a condition under which sensorless control typically faces increased challenges. As shown in Fig. 3.14(a), the rotor speed closely tracks the reference, indicating good speed regulation. Similarly, the estimated frequency in Fig. 3.14(b) remains stable, confirming the robustness of the SOGI-FLL estimator under reduced-speed operation. The estimated rotor angle in Fig. 3.14(c) evolves smoothly, thereby preserving synchronization. However, Fig. 3.14(d) shows a noticeable increase in stator current as the speed decreases. At 700 rpm, the current reaches approximately 5 A, which is nearly twice the rated value. This increase is mainly attributed to the fixed slip value s=0.02. Overall, the system operates stably under reduced-speed conditions, although with an increased current demand as the speed decreases.

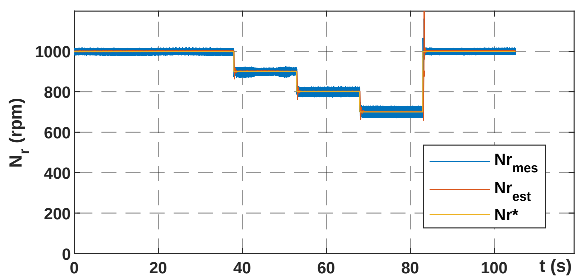

(a) Motor speed N_r

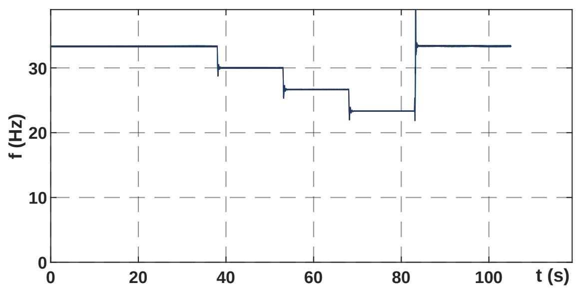

(b) Estimated frequency $f_{s_{est}}$

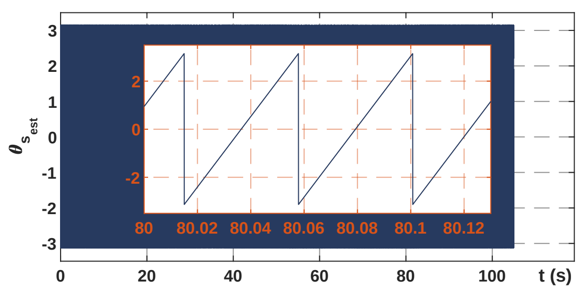

(c) Estimated angle θ_{sest}

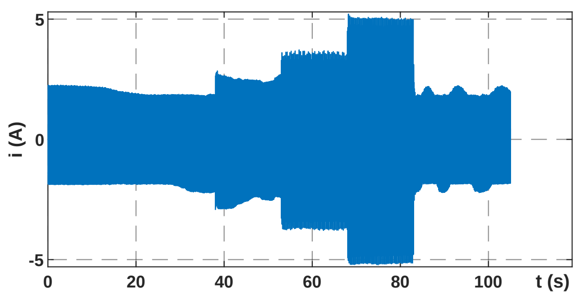

(d) Current i_a

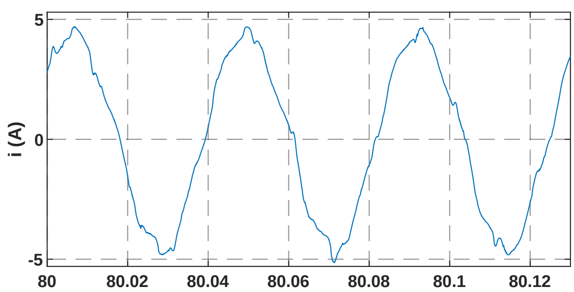

(e) zoom of current i_a

Fig 3.14. Reduced-speed operation test

3.7 Conclusion

This chapter presented the scalar control method for induction motor drives, along with a sensorless extension based on the Second-Order Generalized Integrator with Frequency-Locked Loop (SOGI-FLL) estimator. The proposed approach effectively eliminates the need for a mechanical speed sensor, contributing to a simpler and more cost-efficient drive system architecture. The method was validated through both simulation and experimental results, which demonstrated reliable performance in medium to high-speed operating regions.

The SOGI-FLL estimator proved to be accurate and robust in estimating rotor speed and frequency components, allowing the sensorless control system to operate effectively without direct speed measurement. However, a key limitation of the scalar control approach was identified at low speeds, where the drive system exhibited reduced performance and control precision. This behavior is mainly attributed to the fixed slip value selected for the control strategy, which is not optimal over the entire speed range. As the operating speed decreases, maintaining a constant slip leads to an increased stator current demand. Adapting the slip value according to the speed operating region would allow improved current regulation and overall performance.

To address this limitation, the next chapter will introduce an advanced control strategy that provides better control characteristics at low speeds. The upcoming work will focus on implementing a more sophisticated vector control scheme, capable of improving the dynamic response and ensuring accurate torque production, thereby extending the drive's performance across the full speed range.

Chapter 4

Sensorless DTC based on MESOGI-FLL Estimator

4.1 Introduction

This chapter presents the design, implementation, and validation of a sensorless Direct Torque Control (DTC) strategy for induction motors using a Multiple Enhanced Second-Order Generalized Integrator Frequency-Locked Loop (MESOGI-FLL) estimator. Following the scalar control approach developed in the previous chapter, this section transitions to a more dynamic and precise method that ensures fast torque response and accurate flux regulation-key requirements for advanced motor drive systems [95, 96].

The classical DTC technique is known for its simple structure and excellent dynamic performance, as it directly controls electromagnetic torque and stator flux using a switching table and hysteresis controllers [97, 98]. However, traditional implementations typically rely on mechanical sensors to acquire rotor speed or position, which can introduce cost, complexity, and reliability issues [99, 100]. To overcome these limitations, sensorless DTC strategies have been extensively investigated, where the estimation of rotor speed and flux plays a critical role in the overall system performance [101, 102].

In this work, a sensorless DTC scheme is developed by embedding the MESOGI-FLL estimator within the control loop. The MESOGI-FLL structure is a robust and enhanced observer based on multiple decoupled second-order generalized integrators, designed to extract clean frequency and amplitude estimates from distorted or noisy current signals [103, 104]. By leveraging multiple adaptive filters operating in parallel, this estimator enhances dynamic response and resilience to harmonics, improving the reliability of flux and speed estimation under rapidly changing conditions [105, 106].

The integration of MESOGI-FLL in the DTC scheme allows accurate estimation of rotor angular frequency and stator flux components without using any mechanical sensors. Compared to conventional observers or single SOGI-FLL approaches, the MESOGI-FLL improves convergence speed, minimizes steady-state error, and maintains robust operation across a wider range of operating conditions [104, 105]. These features are essential for achieving high-performance sensorless DTC [100, 101].

To assess the dynamic performance of the Direct Torque Control (DTC) strategy independently of the sensorless estimation framework, the system is experimentally tested under the New European Driving Cycle (NEDC) using a speed sensor. This standardized profile reproduces realistic driving conditions, including acceleration, deceleration, cruising, and idling phases, allowing for a comprehensive evaluation of the control algorithm under time-varying load and speed conditions [107]. The results obtained with the speed sensor serve as a performance benchmark for the DTC scheme and help establish a reference for future integration of the MESOGI-FLL estimator into real driving scenarios.

The proposed sensorless DTC strategy based on the MESOGI-FLL estimator is experimentally evaluated in this chapter to demonstrate its real-time performance and practical applicability in electric drive systems. The MESOGI-FLL is employed to estimate the rotor speed without the use of mechanical sensors, enabling a fully sensorless control structure that enhances reliability and reduces system complexity. The chapter first presents the mathematical formulation and control architecture of the DTC scheme, followed by a detailed description of the design and operating principles of the MESOGI-FLL estimator, with particular emphasis on its filtering characteristics and frequency estimation mechanism. Subsequently, experimental results obtained under the NEDC driving profile are analyzed to evaluate the dynamic response, estimation accuracy, and robustness of the proposed control strategy under realistic operating conditions. The experimental setup and real-time measurements are also discussed, providing further validation of the effectiveness and feasibility of the developed sensorless control approach [102, 106].

4.2 Fundamentals of Direct Torque Control (DTC)

Direct Torque Control (DTC) enables independent regulation of the stator flux and electromagnetic torque within the stationary reference frame (α, β). It relies on a predefined switching table to determine the suitable voltage vector to apply [108–110]. The selection process is closely linked to the instantaneous variations in stator flux and torque. To maintain these quantities within acceptable limits, DTC employs hysteresis controllers that constrain both flux and torque within specific tolerance bands. These controllers operate separately, each ensuring precise control of its respective variable. Based on the calculated flux and torque errors, the hysteresis outputs dictate the optimal switching state to be applied during each control cycle [111, 112].

4.2.1 Torque and Flux Controllers

4.2.1.1 Flux Controller

The evolution of the stator flux vector in DTC is a direct result of the applied voltage vector selected by the inverter [110, 111]. In the stationary reference frame, the stator flux trajectory is influenced by the direction and magnitude of this voltage vector. When an active voltage vector is applied, the stator flux moves along a specific path, typically forming a circular or hexagonal trajectory. The rate of change and orientation of the flux vector depend on both the selected switching state and the operating conditions of the motor. By strategically selecting the appropriate voltage vector through the control algorithm, the DTC method ensures that the stator flux remains within the desired amplitude range while also maintaining the required phase angle, which is essential for efficient torque production and dynamic response [113, 114].

Based on the induction motor model expressed in the stationary reference frame, the stator flux can be defined by the following differential equation [111]:

$$\frac{d\boldsymbol{\phi}_s}{dt} = \boldsymbol{V}_s - R_s\boldsymbol{i}_s \tag{4.1}$$

Integrating this expression over time gives the general solution for the stator flux vector:

$$\boldsymbol{\phi}_s(t) = \boldsymbol{\phi}_s(0) + \int_0^{T_z} (\boldsymbol{V}_s - R_s\boldsymbol{i}_s)\, dt \tag{4.2}$$

where $\phi_s(0)$ represents the initial stator flux at $t = 0$. In high-speed operating conditions, the voltage drop across the stator resistance $R_s i_s$ becomes negligible compared to the applied stator voltage. Thus, the flux equation simplifies to:

$$\boldsymbol{\phi}_s(t) \approx \boldsymbol{\phi}_s(0) + \boldsymbol{V}_s T_z \tag{4.3}$$

Consequently, the variation in stator flux over a sampling period T_z can be approximated by:

$$\Delta\boldsymbol{\phi}_s = \boldsymbol{\phi}_s(t) - \boldsymbol{\phi}_s(0) \approx \boldsymbol{V}_s T_z \tag{4.4}$$

This relation indicates that the stator flux vector can be modulated by the application of a voltage vector over the sampling interval. As a result, the tip of the stator flux vector shifts in the direction of the applied voltage, tracing a path that approximates a circular or polygonal trajectory depending on the switching pattern.

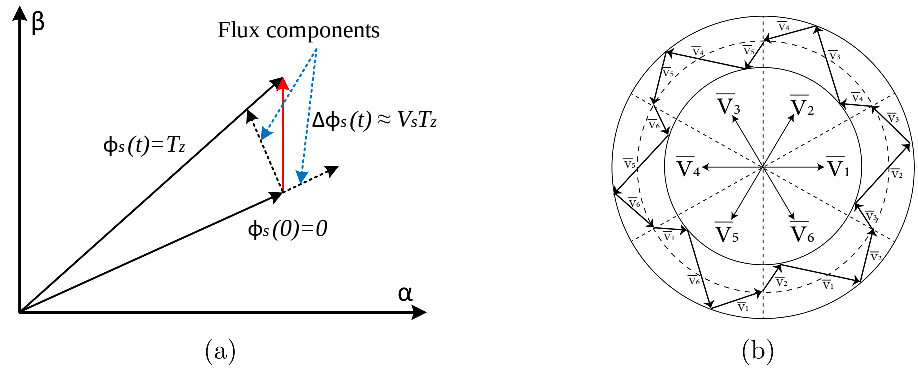

(a) (b)

Fig 4.1. Stator flux vector evolution driven by voltage vector selection

The flux controller plays a critical role in DTC strategy by regulating the magnitude of the stator flux vector. Its main objective is to maintain the flux within a predefined hysteresis band around its reference value, ensuring a fast dynamic response and robust performance under various operating conditions.

In a standard DTC scheme, the stator flux is estimated in the stationary reference frame, and its magnitude is compared with the reference flux. The resulting error is processed by a two-level hysteresis controller. This controller produces a binary output depending on whether the actual flux is above, below, or within the hysteresis band. The logic governing this decision-making process is illustrated in Fig 4.2, which shows the structure of the two-level flux controller. The controller's output, denoted as $S\phi_s$, delivers a high or low signal based on the flux error, as defined by the following conditions:

$$\begin{aligned} if \quad \Delta\phi_s &\leq -h_{\phi_s} \longrightarrow S_{\phi_s} = 0 \\ if \quad \Delta\phi_s &> h_{\phi_s} \quad \longrightarrow S_{\phi_s} = 1 \end{aligned} \tag{4.5}$$

Note that h_{ϕ_s} represents the hysteresis band of the stator flux, while $\Delta\phi_s$ denotes the stator flux error, defined as the difference between the reference flux magnitude and the estimated actual flux value as shown below:

$$\Delta\phi_s = |\phi_s^*| - |\phi_s| \tag{4.6}$$

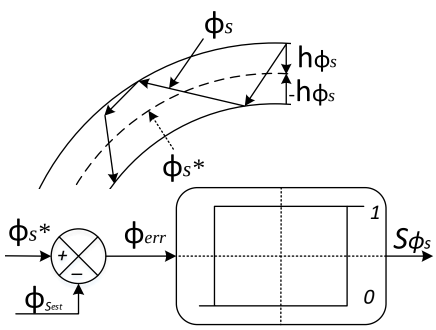

Fig 4.2. Two-level hysteresis flux controller.

4.2.1.2 Torque Controller

The electromagnetic torque is directly regulated using a hysteresis controller, in a manner similar to the flux control loop [113, 114]. The primary objective of the torque controller is to maintain the developed electromagnetic torque within a specified hysteresis band around the reference torque command. This ensures a fast dynamic response and high-performance torque regulation without the need for complex current regulators or coordinate transformations [111, 112, 115].

The electromagnetic torque is first estimated using the stator flux and the stator current components in the stationary reference frame. The torque error is then computed as the difference between the reference torque (T_e^*) and the actual estimated torque (T_e) as shown in Fig 4.3.

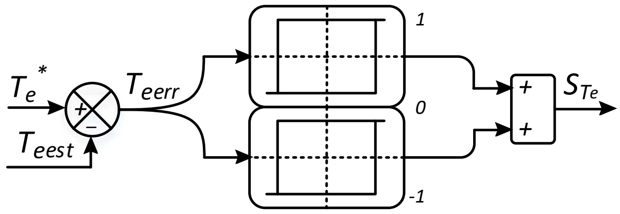

Fig 4.3. Three-level hysteresis torque controller.

The error (ΔT_e) is evaluated using a three-level hysteresis controller defined by a hysteresis band h_{T_e}. The output signal S_{T_e} of the controller can take one of three possible values based on the following logic:

$$S_{T_e} = \begin{cases} +1 & \text{if} \quad \Delta T_e \quad > \quad h_{T_e} \\ 0 & \text{if} \quad |\Delta T_e| \quad \leq \quad h_{T_e} \\ -1 & \text{if} \quad \Delta T_e \quad < \quad -h_{T_e} \end{cases} \tag{4.7}$$

This three-level control output enables more precise torque regulation by selecting the appropriate voltage vector from the DTC switching table, in coordination with both the flux controller and the stator flux vector position. Here, h_{T_e} denotes the hysteresis band of the torque, while ΔT_e represents the torque error, defined as the difference between the reference torque and the actual estimated torque value, as expressed below:

$$\Delta T_e = T_e^* - T_e \tag{4.8}$$

4.2.2 Estimation of Torque and Stator Flux

4.2.2.1 Stator Flux Estimation

In DTC, accurate estimation of the stator flux is essential for effective torque and flux regulation, particularly in sensorless control schemes. The stator flux is typically estimated using the voltage model approach, which relies on the integration of the difference between the stator voltage and the voltage drop across the stator resistance. In the stationary reference frame (α, β), the stator flux components can be expressed as:

$$\begin{aligned} \phi_{s\alpha} &= \int (v_{s\alpha} - R_s i_{s\alpha}) dt \\ \phi_{s\beta} &= \int (v_{s\beta} - R_s i_{s\beta}) dt \end{aligned} \tag{4.9}$$

where v_α, v_β are the stator voltage components, i_α, i_β are the stator current components, and R_s is the stator resistance. The magnitude of the stator flux vector ($|\phi_s|$), and the stator angle (θ_s) is then calculated as:

$$\begin{aligned} |\phi_s| &= \sqrt{\phi_{s\alpha}^2 + \phi_{s\beta}^2} \\ \theta_s &= tan^{-1}(\tfrac{\phi_{s\beta}}{\phi_{s\alpha}}) \end{aligned} \tag{4.10}$$

The stator voltage components $v_{s\alpha}$ and $v_{s\beta}$ are derived by performing the Concordia transformation on the three-phase inverter output voltages, as given below:

$$\begin{bmatrix} v_{s\alpha} \\ v_{s\beta} \end{bmatrix} = \frac{2}{3} \begin{bmatrix} 1 & -\frac{1}{2} & -\frac{1}{2} \\ 0 & \frac{\sqrt{3}}{2} & -\frac{\sqrt{3}}{2} \end{bmatrix} \begin{bmatrix} v_{sa} \\ v_{sb} \\ v_{sc} \end{bmatrix} \tag{4.11}$$

Similarly, the stator current components $i_{s\alpha}$ and $i_{s\beta}$ in the stationary reference frame are obtained by applying the Concordia transformation to the three-phase stator currents, as expressed below:

$$\begin{bmatrix} i_{s\alpha} \\ i_{s\beta} \end{bmatrix} = \frac{2}{3} \begin{bmatrix} 1 & -\frac{1}{2} & -\frac{1}{2} \\ 0 & \frac{\sqrt{3}}{2} & -\frac{\sqrt{3}}{2} \end{bmatrix} \begin{bmatrix} i_{sa} \\ i_{sb} \\ i_{sc} \end{bmatrix} \tag{4.12}$$

4.2.2.2 Electromagnetic Torque Estimation

In DTC, accurate estimation of the electromagnetic torque is essential for ensuring precise control and dynamic performance of the IM. The torque is typically calculated based on the cross-product of the stator flux and the stator current vectors in the stationary reference frame. This method relies on the flux components obtained from the voltage model and the current components derived from the Concordia transformation. The electromagnetic torque expression used in DTC is given by the following equation:

$$T_e = \frac{3}{2} P \left(\phi_{s\alpha} i_{s\beta} - \phi_{s\beta} i_{s\alpha}\right) \tag{4.13}$$

4.2.3 Sectors divisions

In the DTC scheme, the stator flux vector plays a central role in determining the appropriate inverter switching states. To facilitate voltage vector selection, the stationary reference frame is divided into six equal sectors, each spanning 60°, as shown in Fig 4.4. This method was first introduced by Takahashi and Depenbrock [108, 109] and remains foundational in DTC research [110–112]. The angular position of the stator flux vector with respect to the α-axis is continuously tracked to determine its current sector. This classification enables the controller to select the optimal voltage vector from the predefined switching table, ensuring effective torque and flux control. The identification of the sector is based on the angle θ_s, which is calculated from the estimated flux components in (4.10).

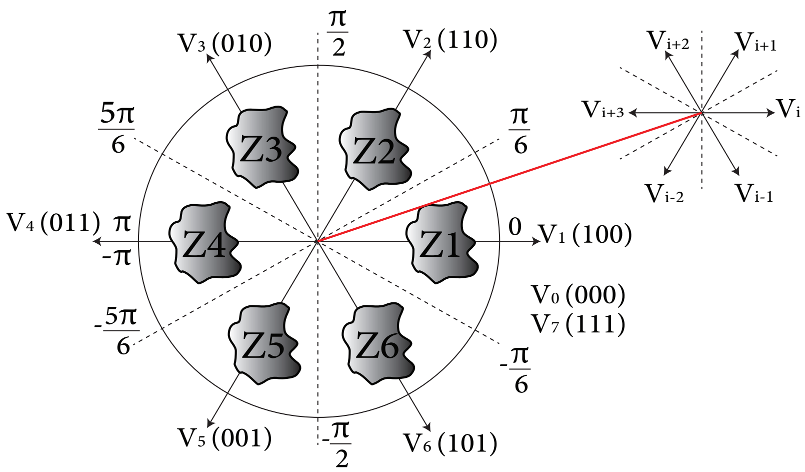

Fig 4.4. Sectors selection and stator flux vector evolution

While the stator flux vector is located in sector ii, the effects of applying different voltage vectors on the stator flux magnitude ($|\phi_s|$) and electromagnetic torque (T_e) are summarized as follows:

$$\begin{aligned}
&\text{If } V_{i+1} \text{ is applied} \longrightarrow \phi_s \text{ increases and } T_e \text{ increases.}\\
&\text{If } V_{i-1} \text{ is applied} \longrightarrow \phi_s \text{ increases and } T_e \text{ decreases.}\\
&\text{If } V_{i+2} \text{ is applied} \longrightarrow \phi_s \text{ decreases and } T_e \text{ increases.}\\
&\text{If } V_{i-2} \text{ is applied} \longrightarrow \phi_s \text{ decreases and } T_e \text{ decreases.}
\end{aligned}$$

In each sector, the voltage vectors V_i and V_{i+3} are typically not utilized, as they can either increase or decrease the torque depending on the exact position of the stator flux vector within the sector. When zero voltage vectors V_0 and V_7 are applied, the stator flux vector ceases to rotate, resulting in a constant flux magnitude. Under this condition, the electromagnetic torque decreases, although the reduction is less significant compared to when active voltage vectors are used.

Table 4.1 presents the classical DTC switching table, widely adopted in the literature [110, 112], which is constructed by discretizing the stator flux and electromagnetic torque into defined levels. Each entry in the table corresponds to a specific combination of flux and torque conditions, indicating the appropriate voltage vector to be applied for that state.

Table 4.1. Switching table

S_{ϕ_s}	S_{T_e}	Z1	Z2	Z3	Z4	Z5	Z6
0	1	V_3	V_4	V_5	V_6	V_1	V_2
0	0	V_0	V_7	V_0	V_7	V_0	V_7
0	-1	V_5	V_6	V_1	V_2	V_3	V_4
1	1	V_2	V_3	V_4	V_5	V_6	V_1
1	0	V_7	V_0	V_7	V_0	V_7	V_0
1	-1	V_6	V_1	V_2	V_3	V_4	V_5

4.3 Rotor Speed Estimation based on MESOGI-FLL

The schematic representation of the proposed rotor speed estimation approach using the Mesogi-Fll is illustrated in Fig 4.5. This configuration comprises two main functional components. First, the Mesogi-Fll unit is responsible for extracting the stator electrical frequency, denoted as ω_s, from the measured single-phase current signal i_c. Second, a slip estimation module is employed to determine the slip value, s, based on the estimated stator frequency and the calculated electromagnetic torque, T_e.

Using these two estimated parameters, rotor speed ω_r is then derived. This is accomplished by computing the product of the stator frequency ω_s and the slip speed, followed by scaling with the appropriate conversion factor, $\left(\frac{60}{2p\pi}\right)$, to express the result in revolutions per minute (rpm). The proposed approach ensures that rotor speed estimation is both fast and robust, providing high accuracy even in the presence of current signal noise and parameter variations. Furthermore, its implementation is computationally efficient, making it suitable for real-time applications in Sc of induction motors.

It is important to highlight that the Mesogi-Fll estimator inherently provides frequency estimation only for positive rotational direction. To address this limitation and enable bidirectional motor operation, a Sign block is incorporated in the Simulink implementation. This block determines the sign of the reference speed, thus allowing the control system to infer and adapt to motor rotation in the reverse direction when needed. Consequently, the proposed estimation strategy is fully compatible with dynamic operating conditions, including rapid acceleration, deceleration, and sudden load changes, while maintaining reliable speed tracking performance throughout all operating ranges.

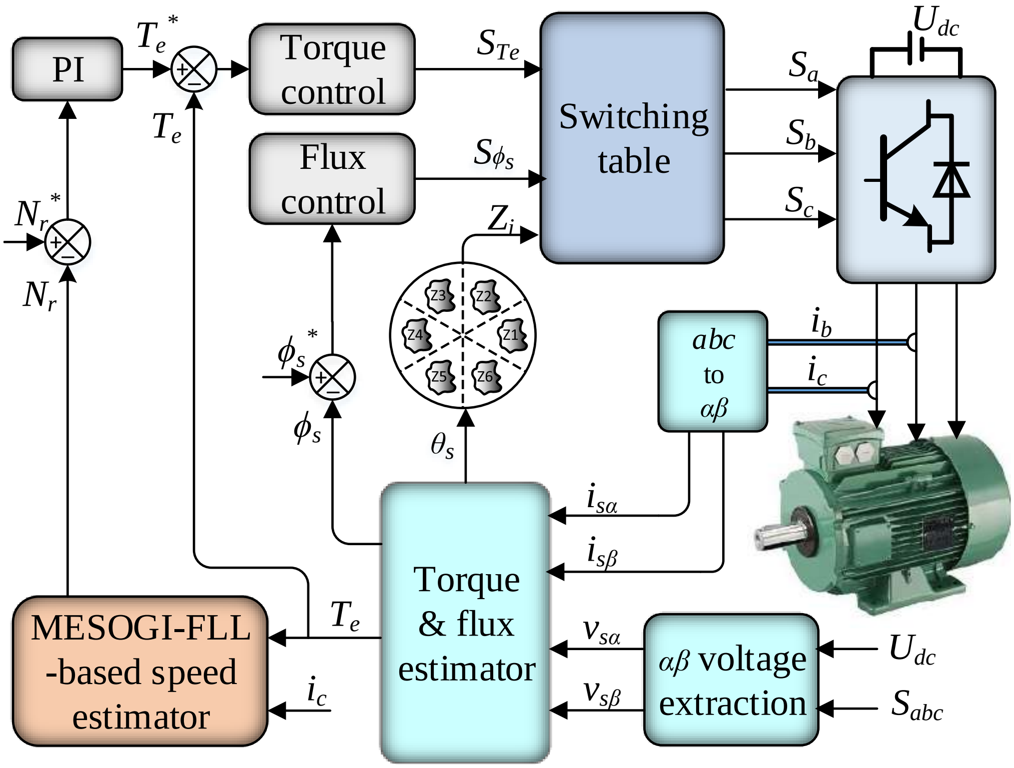

Fig 4.5. Induction motor drive system with SSDTC scheme.

4.3.1 MESOGI-FLL Estimator

The MESOGI-FLL structure represents an advanced adaptive filtering technique designed for the precise estimation of both fundamental and harmonic components within a single-phase sinusoidal signal. Its main advantage lies in its ability to suppress DC disturbances and reject harmonic interferences, enabling robust extraction of key signal characteristics such as amplitude, frequency, and orthogonal components of the input current. As illustrated in Fig 4.7(a), the system is architecturally divided into two principal modules: the MESOGI (Multiple Enhanced Second-Order Generalized Integrator) and the FLL (Frequency-Locked Loop).

The MESOGI module serves to extract the in-phase ($i_{c\alpha}$) and quadrature ($i_{c\beta}$) components of the measured current signal i_c. It operates at the fundamental frequency and selectively targeted harmonic frequencies. In this implementation, harmonics of orders 1st, 5th, 7th, and 11th are specifically considered. Internally, the MESOGI consists of a combination of multiple SOGI units working in parallel: a single ESOGI (Enhanced SOGI) for the fundamental component, and conventional SOGIs for the higher-order harmonics. The input to each SOGI is preconditioned by removing the contributions of the remaining harmonic components, ensuring that each unit processes a harmonics-cleaned version of the signal. This approach enhances the accuracy of individual component extraction.

The ESOGI, which is detailed in Fig 4.7(b), introduces an in-loop filter into the classical SOGI framework, as shown in Fig 4.7(c), enabling it to effectively estimate and eliminate the DC offset from the β-axis component of the signal. The α-axis output of each conventional SOGI is retained for further processing, while the β-axis output is only utilized in the ESOGI. This design ensures that the DC disturbance is effectively rejected in the β-axis component, thereby preventing it from influencing the frequency estimation process.

A key element of the MESOGI design is the dynamic tuning of each SOGI unit. The center frequency of each SOGI is derived by multiplying the estimated fundamental frequency by a constant factor corresponding to the harmonic order under consideration, as indicated in reference [116]. This adaptive tuning mechanism ensures that each SOGI tracks its target frequency component accurately over time.

Following the MESOGI module, the FLL estimator shown in Fig 4.7(d) is responsible for estimating the real-time fundamental frequency, denoted as ω_s. It takes as input the error signal e, which is computed by subtracting both the α-axis output and the estimated DC component (from ESOGI) from the actual input signal. In addition, the β-axis output from the ESOGI, now free of DC disturbances, is also used in the frequency calculation. The combination of these inputs allows the FLL to deliver an accurate, ripple-free estimation of the system's operating frequency. As a result, the FLL output remains stable even in the presence of noise or distortion in the input signal.

The mathematical formulation for the FLL frequency estimation, as depicted in Fig 4.7(d), is presented in [117], and will be further detailed in the following subsection.

$$\omega_s = \frac{\gamma}{s}[i_c(s) - i_{c\alpha}(s) - i_{dc}(s)]i_{c\beta}(s) \tag{4.14}$$

where γ is the FLL gain and can be determined as follows:

$$\gamma = \frac{k\omega_s}{V^2}\Gamma \tag{4.15}$$

being V the estimated amplitude and Γ is a positive gain that depends on the settling time of the FLL .

While $i_{c\alpha}$, $i_{c\beta}$, and i_{dc} introduced in (4.14) are the ESOGI's current fundamental and DC components, which can be expressed as follows [117]:

$$\begin{aligned} i_{c\alpha}(s) &= \tfrac{k\omega_s s}{s^2+k\omega_s s+\omega_s^2} i_c(s) \\ i_{c\beta}(s) &= \tfrac{k(\omega_s^2-\omega_f s)}{s+\omega_f}\tfrac{s}{s^2+k\omega_s s+\omega_s^2} i_c(s) \\ i_{dc}(s) &= \tfrac{\omega_f}{s+\omega_f}(i_c(s) - i_{c\alpha}(s)) \end{aligned} \tag{4.16}$$

where ω_f defines the cut-off frequency of the LPF, and k is the positive gain of the ESOGI adjusted as a trade-off between the speed of dynamic response and filtering features.

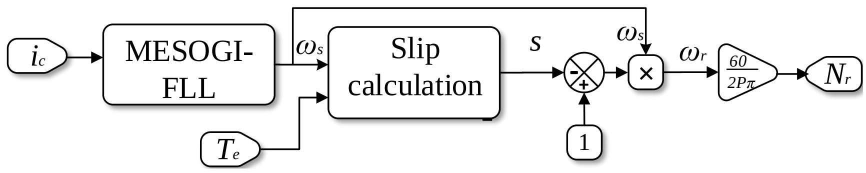

Fig 4.6. Proposed scheme for speed estimation based on the MESOGI-FLL

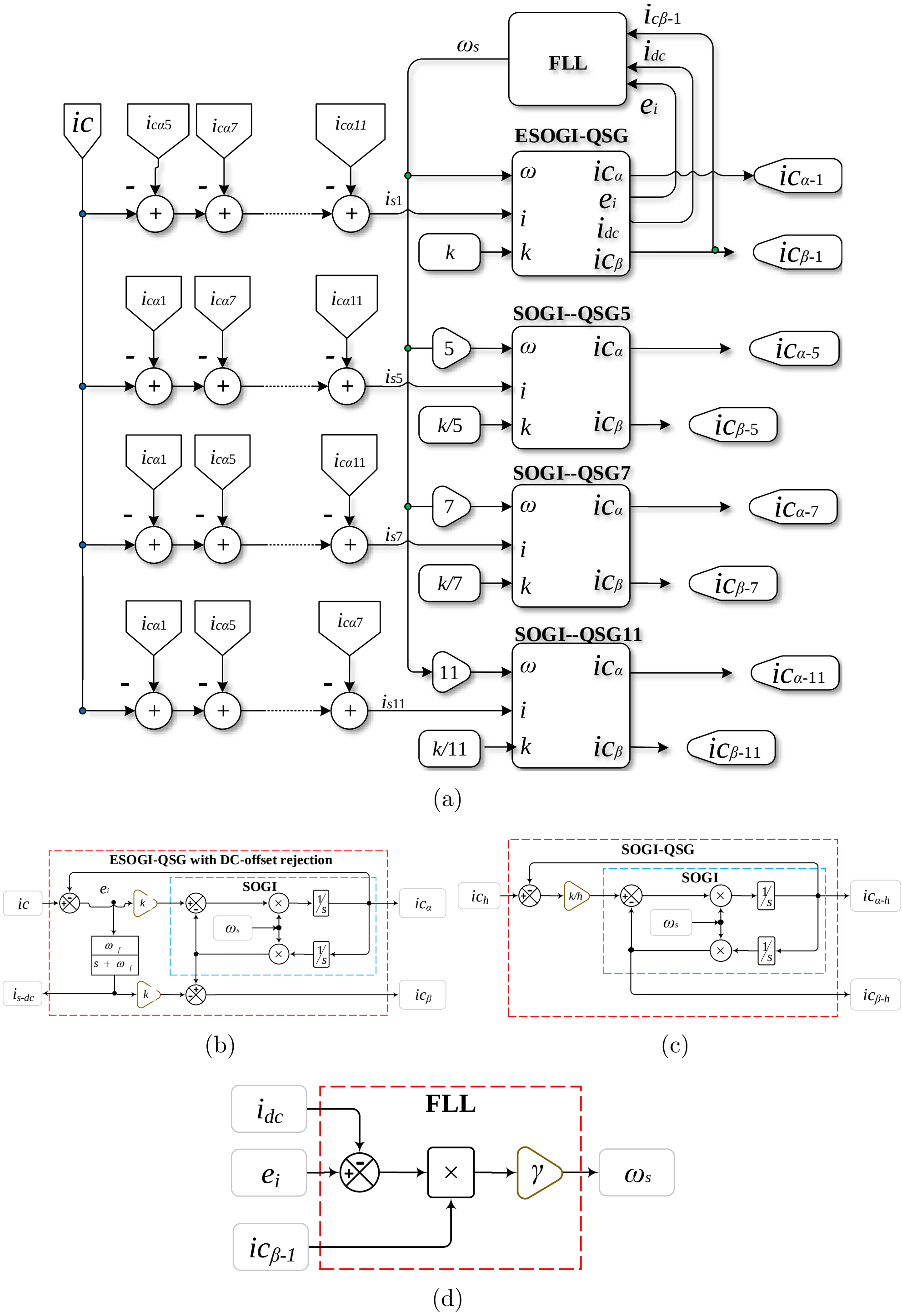

Fig 4.7. Structure of; (a) MESOGI, (b) ESOGI, (c) SOGI, and (d) FLL

4.3.2 Slip Estimation

The following describes the process used to compute the estimated slip, g_{est}, based on the frequency obtained from the FLL. This estimation is derived through a detailed mathematical analysis [118]. The approach begins with the equivalent electrical model of the IM, as shown in Fig 4.8, where the parameters are defined as follows:

$$\begin{gathered} N' = \sigma L_r(\tfrac{L_s}{L_m})^2 \quad ; \quad R'_r = R_r(\tfrac{L_s}{L_m})^2 \\ I'_r = I_r(\tfrac{L_m}{L_s}) \end{gathered} \tag{4.17}$$

where σ is the dispersion coefficient, N' is the total leakage inductance brought back to the stator, I'_r is the rotor current returned to the stator, and R'_r is the rotor resistance brought back to the stator.

The electromagnetic torque, T_e, can be derived as:

$$T_e = \frac{3PR'_r}{g\omega_s} \frac{V_s^2}{\omega_s^2 N'^2 + \frac{R_r'^2}{g^2}} \tag{4.18}$$

where g defines the slip, and the stator voltage V_s is given by:

$$V_s = \phi_s \omega_s \tag{4.19}$$

Considering (4.18) and (4.19), and after some mathematical simplifications, the following second-order equation is obtained:

$$T_e.\omega_s^2.N'^2.g^2 - 3.P.R'_r.\omega_s.\phi_s^2.g + T_e.R_r'^2 = 0 \tag{4.20}$$

By putting: $a = T_e\omega_s^2 N'^2$; $b = -3.P.R'_r\omega_s\phi_s^2$; $c = T_e R_r'^2$ (4.20) yields:

$$a.g^2 + b.g + c = 0 \tag{4.21}$$

This equation, (4.21), has two solutions, g_1 and g_2, expressed as follows:

$$g_1 = \tfrac{-b-\sqrt{\Delta}}{2.a} \quad ; \quad g_2 = \tfrac{-b+\sqrt{\Delta}}{2.a} \tag{4.22}$$

with:

$$\Delta = b^2 - 4.a.c \tag{4.23}$$

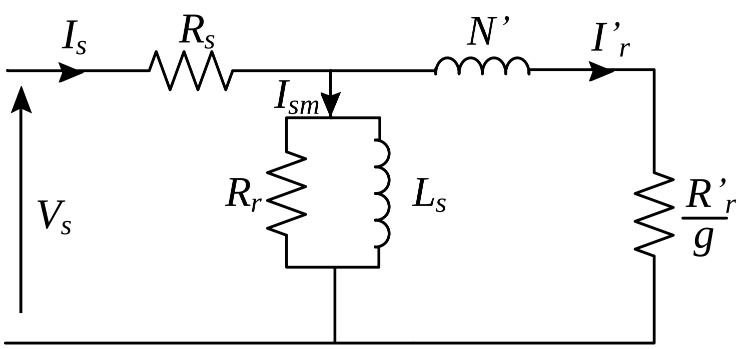

Fig 4.8. IM equivalent circuit.

To determine the valid solution, g_1 or g_2, for (4.21), a simulation test using a system similar to that of Fig 4.5, is carried out in MATLAB/SIMULINK software. The simulation results are obtained by applying a variable resistance torque, T_r, to the IM. The plots of the two solutions, g_1 and g_2, are depicted in Fig 4.9, which highlight that g_1 is the valid solution for (4.21), as it exhibits proper values and varies proportionally to T_r change.

As a result, The slip speed, g, equals g1 given in (4.22), and hence, rotor speed estimation is achieved as follows:

$$N_r = \frac{60}{2P\pi}(1-g)\omega_s \tag{4.24}$$

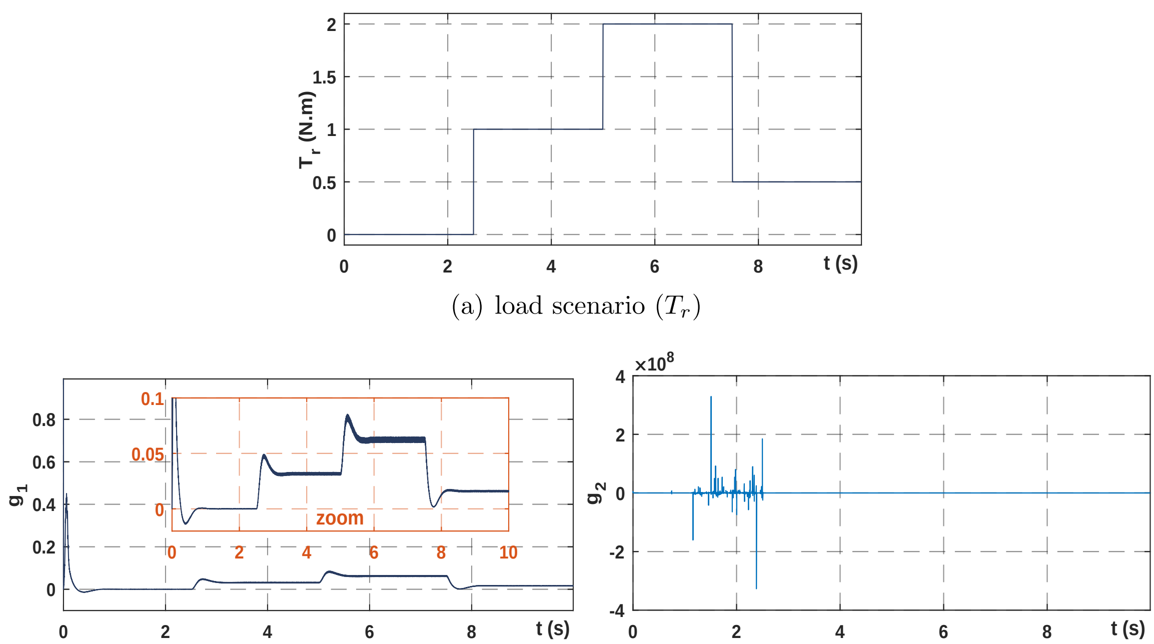

(a) load scenario (T_r)

(b) first solution g_1

(c) Second solution g_2

Fig 4.9. Load scenario, and plots of the obtained solutions, g_1 and g_2.

4.3.3 Performance Assessment of the MESOGI-FLL

In this subsection, the performance of the MESOGI-FLL in comparison with the conventional SOGI-FLL is investigated in MATLAB. Table 4.2 summarizes the MESOGI-FLL and SOGI-FLL parameters taken from [116]. The MESOGI-FLL and the SOGI-FLL estimation accuracy are examined considering three different cases. In case 1, a distorted input current with low-order harmonics, 5th, 7th, and 11th, with magnitudes $V_5 = 0.2$ p.u, $V_7 = 0.15$ p.u, $V_{11} = 0.1$ p.u, and without DC component is considered. Case 2 tests the MESOGI-FLL and SOGI-FLL for a shifted input current with a 0.1 p.u DC component. For case 3, a highly distorted input current containing a DC component of 0.1 p.u and harmonics with the same magnitudes as case 1. The obtained results presenting the responses of the MESOGI-FLL and SOGI-FLL for each case under a sudden frequency variation from 50 Hz to 55 Hz at t = 1s are given in Fig 4.10(a) and Fig 4.10(b). These figures depict the waveforms of the input, i_c, and the output currents, $i_{c\alpha}$ and $i_{c\beta}$, on the right side, and the estimated frequency response with the input frequency, on the left side, for cases 1, 2, and 3, respectively. These figures illustrate that the MESOGI-FLL ensures accurate estimation of the β-axis free form DC component and harmonics, while the one estimated, $i_{c\beta}$, by the SOGI-FLL is shifted by a DC-offset for cases 2 and 3, for the case of the input contains DC component. In addition, the figures on the left side demonstrate an accurate estimation of the operating frequency with good transient response, without any ripples at steady-state for case 2 and with tinny ripples for cases 1 and 3 due to inherent harmonics by using the MESOGI-FLL. Meanwhile, the SOGI-FLL exhibits poor frequency estimation with significant ripples for all cases, with a bigger amplitude for the cases of DC disturbance involved. For more clarity, Table 4.3 summarizes each case's numerical findings, reporting the DC component and THD in the β-axis current and the ripples' maximum magnitude in the estimated frequency for both MESOGI-FLL and SOGI-FLL. These findings confirm the high accuracy of the MESOGI-FLL estimates, in which the $i_{c\alpha\beta}$ currents with no DC component for all cases and maximum THD about 0.42% and 0.23%, respectively, and an estimated frequency with negligible ripples of a magnitude around 0.084 Hz are achieved. The estimated ic_β by the SOGI-FLL contains a DC component of around 7% for the cases of inducing DC disturbance. The maximum THDs of the estimated ic_α and ic_β are obtained around 3.4% and 1.1% for cases 2 and 3. In addition, the estimated frequency by the SOGI-FLL has significant ripples with a maximum amplitude of about 0.4% for case 1 and 0.56% for cases 2 and 3.

Therefore, it can be concluded that the MESOGI-FLL is immune to the DC disturbance and harmonics effect and guarantees an accurate frequency estimation; hence, it is beneficial to implement for estimating the angular frequency (angular speed) of an IM correctly, even in the case of a highly distorted current.

Table 4.2. MESOGI-FLL and SOGI-FLL parameters

Parameter	Symbol	Unit	Value
MESOGI/ SOGI Gain	k	-	0.8
FLL Gain	Γ	s^{-1}	50
LPF cut-off frequency	$\omega_f/2\pi$	Hz	30

Table 4.3. MESOGI-FLL and SOGI-FLL performance.

		Case 01			Case 02			Case 03		
Methods	Input output signals	THD [%]	DC component [%]	Frequency ripples [Hz]	THD [%]	DC component [%]	Frequency ripples [Hz]	THD [%]	DC component [%]	Frequency ripples [Hz]
SOGI-FLL	i_c	26.93	0	0.4	0.14	10	0.565	26.93	10	0.56
	$i_{c\alpha}$	3.33	0		0.66	0		3.4	0	
	$i_{c\beta}$	0.72	0		0.83	7		1.1	7	
MESOGI-FLL	$i_{c\alpha}$	0.42	0	0.048	0.14	0	0	0.42	0	0.048
	$i_{c\beta}$	0.23	0		0.12	0		0.23	0	

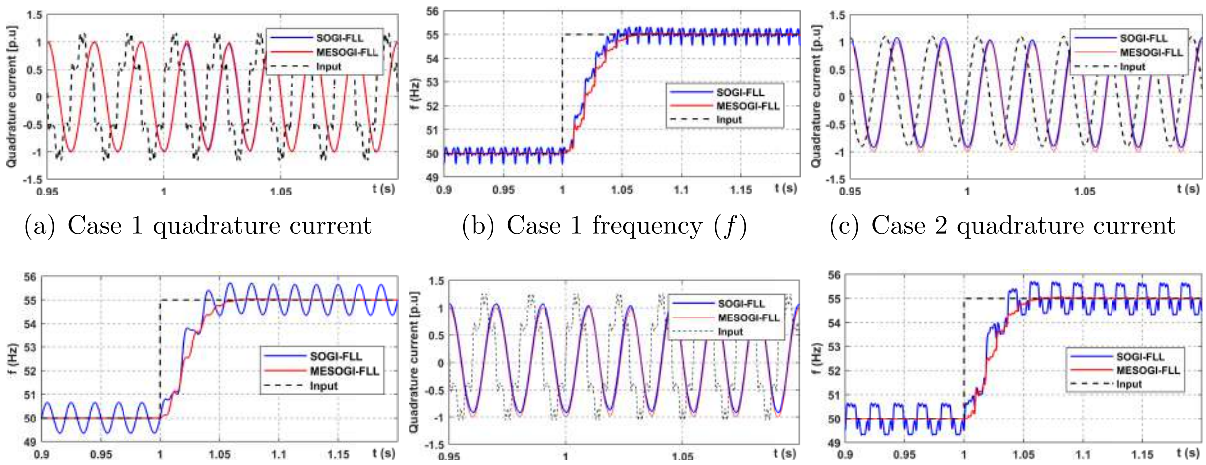

(a) Case 1 quadrature current (b) Case 1 frequency (f) (c) Case 2 quadrature current

(d) Case 2 frequency (f) (e) Case 3 quadrature current (f) Case 3 frequency (f)

Fig 4.10. SOGI-FLL and MESOGI-FLL performance for cases 1, 2, and 3.

4.4 Experimental Results

The experimental validation of the proposed control strategies has been carried out using a dedicated test bench, as shown in Fig 4.11. The setup consists of a computer running MATLAB/SIMULINK, which interfaces with a dSPACE MicroLabBox (DS1202) for real-time implementation. The control algorithm is compiled and deployed through the Control Desk software. Six PWM pulses are generated and passed through an adaptation and isolation card (5V-15V) to drive a Semikron three-phase inverter, which in turn supplies an IM.

The induction motor is coupled to a Powder brake equipped with a torque control unit to emulate various loading conditions. The system is instrumented with LA 55-P current sensors and an incremental encoder (DC 5V-24V, 4096 P/R) to capture motor measurements. Experimental data are acquired using Control Desk and post-processed in MATLAB for visualization and analysis.

To comprehensively evaluate the proposed methods, the experimental results are divided into two parts:

- Dynamic performance of the drive system in a vehicle application scenario.
- SSDTC based on the MESOGI-FLL estimator.

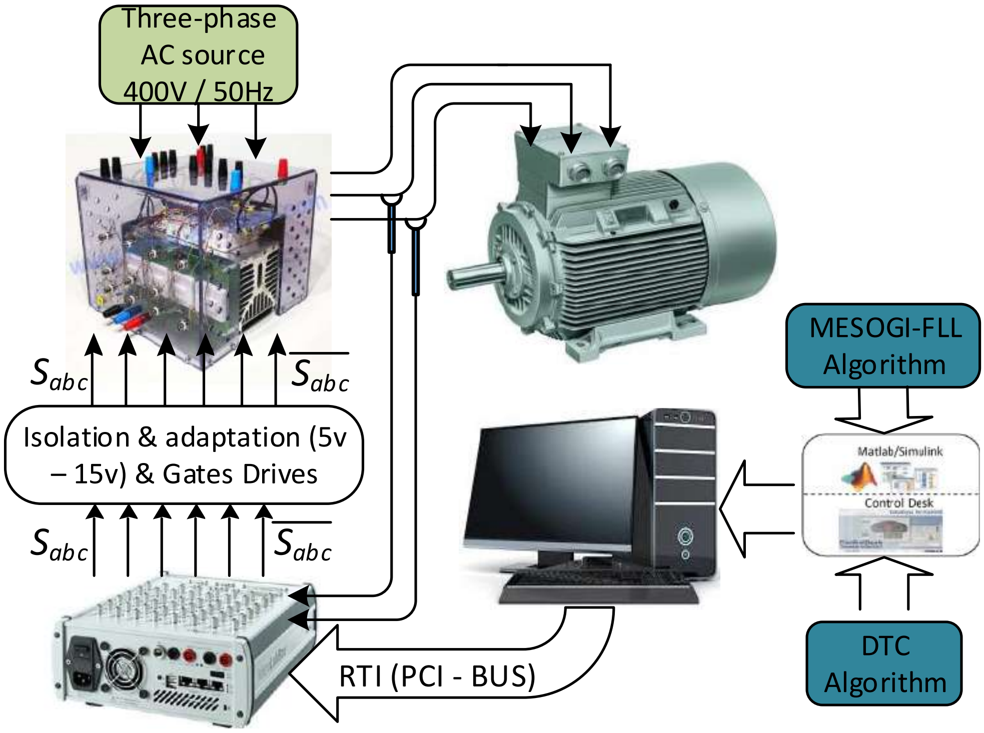

(a) System implementation schematic diagram

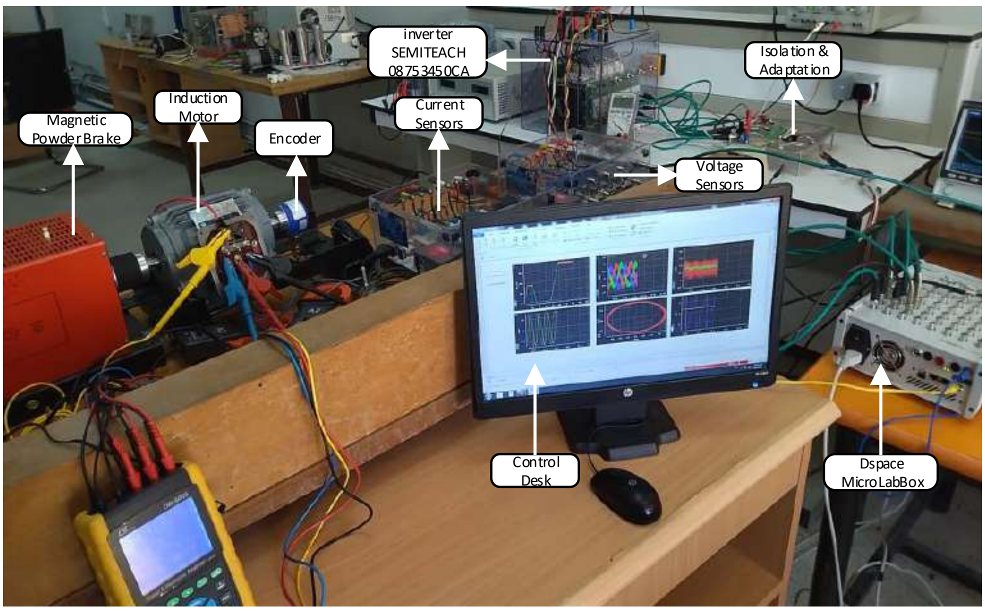

(b) An actual photograph.

Fig 4.11. Experimental test bench.

4.4.1 Evaluation of EV Performance Using the NEDC Cycle

In this subsection, the performance of the DTC strategy is experimentally validated using a realistic vehicle dynamic profile. The New European Driving Cycle (NEDC) is employed as a reference speed profile to simulate standard vehicle operation, providing a comprehensive evaluation of the drive system's dynamic response. rotor speed is directly measured via an incremental encoder to ensure precise feedback control.

The reference speed from the NEDC profile is introduced into the DTC control loop via MATLAB/SIMULINK, and the corresponding control algorithm is deployed in real time using dSPACE MicroLabBox (DS1202). The six PWM signals generated are sent through an isolation card to the Semikron inverter, which drives the induction motor. The system's ability to track the complex speed trajectory of the NEDC profile with high accuracy is demonstrated, reflecting the DTC strategy's robustness and dynamic capability. The resulting speed and torque responses are captured and plotted to illustrate the effectiveness of the system in real-world driving scenarios.

Fig 4.12 illustrates the experimental validation of the DTC strategy under the NEDC cycle. The motor speed (Fig 4.12(b)) closely tracks the reference profile. During acceleration, the measured speed increases smoothly with minimal delay, while during deceleration it decreases in synchronization with the reference. In steady-speed segments, rotor speed remains aligned with the commanded values, demonstrating the accuracy and robustness of the control system.

The phase currents i_a, i_b, and i_c (Fig 4.12(c)) are balanced and exhibit the expected 120° displacement. Their amplitudes increase during acceleration to meet higher torque demand and decrease during cruising and deceleration, remaining within safe limits. Small switching-induced ripples appear, consistent with DTC operation.

The electromagnetic torque T_e (Fig 4.12(d)) responds rapidly to speed changes, increasing during acceleration and decreasing during deceleration or cruising. A minor torque ripple is visible, characteristic of DTC. The stator flux magnitude ϕ_s (Fig. 4.12(e)) remains near its reference with small oscillations inside the hysteresis band, confirming accurate flux estimation and regulation.

The stator flux components $\phi_{s\alpha}$ and $\phi_{s\beta}$ during the NEDC cycle are illustrated in (g), showing sinusoidal waveforms indicative of balanced and stable flux. Fig 4.12(f) shows the reference angle θ_s^*, accurately followed by the control system. The flux trajectory in the $\alpha\beta$ plane (Fig. 4.12(h)) plots $\phi_{s\beta}$ versus $\phi_{s\alpha}$, forming a nearly circular locus centered at the origin. This demonstrates that the stator flux vector rotates smoothly and remains balanced, with magnitude and orientation well regulated, returning to zero whenever the reference speed reaches zero.

Overall, these results demonstrate that the proposed DTC strategy provides accurate speed tracking, balanced current waveforms, fast and robust torque response, and stable flux regulation under realistic driving conditions, confirming its suitability for electric vehicle applications.

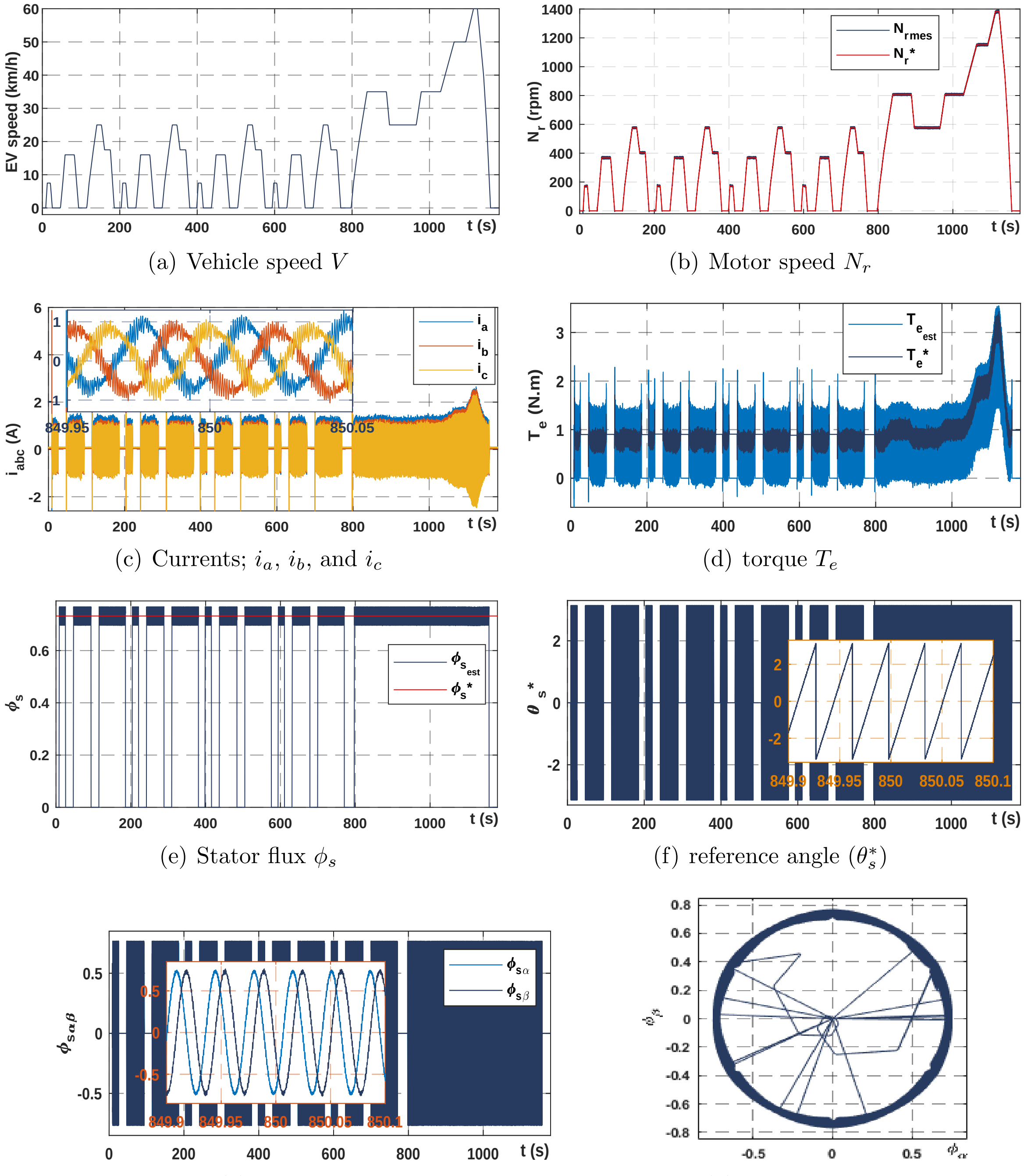

(a) Vehicle speed V

(b) Motor speed N_r

(c) Currents; i_a, i_b, and i_c

(d) torque T_e

(e) Stator flux ϕ_s

(f) reference angle (θ_s^*)

(g) $\phi_{s\alpha}$ and $\phi_{s\beta}$

(h) Flux trajectory

Fig 4.12. Experimental validation during NEDC cycle drive

4.4.2 SSDTC Based on MESOGI-FLL Estimator Resutls

This part presents the experimental validation of the proposed sensorless speed and torque control strategy, namely the Mesogi-Fll-based SSDtc. In this configuration, rotor speed is estimated in real time using the Mesogi-Fll algorithm integrated into the Dtc scheme, eliminating the need for a physical speed sensor.

The control algorithm, including the Mesogi-Fll estimator, is deployed through the dSPACE MicroLabBox and executed using Control Desk software. The estimated speed is used as feedback in the Dtc control loop, and the inverter drives the induction motor accordingly. The test scenarios include variable speed commands, sudden load changes, and reverse rotation, which are intended to assess the robustness and adaptability of the proposed estimator.

Experimental results, including estimated versus actual speed (from encoder), torque performance, and system behavior under load perturbations, are collected and analyzed. These results confirm the effectiveness of the Mesogi-Fll estimator in delivering stable and accurate rotor speed estimation, even under challenging operating conditions, demonstrating its suitability for sensorless Dtc applications in electric drive systems.

4.4.2.1 Variable Speeds Test

This test evaluates the performance of the proposed Mesogi-Fll-based SSDTC under variable rotor speed conditions. The reference speed, N_r^*, is varied from 1200 rpm down to 800, 400, 200 rpm, and back to 1200 rpm, with results shown in Fig 4.13.

As seen in Fig 4.13(a), both the measured rotor speed Nr_{mes} and the estimated speed N_r closely follow the reference throughout all transitions, with the estimated speed exhibiting less noise, highlighting the accuracy and robustness of the Mesogi-Fllestimator. The estimated stator frequency $f_{s_{est}}$ (Fig 4.13(b)) adapts smoothly to speed changes with minimal delay, demonstrating reliable dynamic response.

The estimated slip g_{est} (Fig 4.13(c)) and torque T_e (Fig 4.13(e)) respond consistently to speed variations, with torque closely tracking its reference T_e^*. The flux components $\phi_{s\alpha}$ and $\phi_{s\beta}$ (Fig 4.13(g)) remain well-estimated, confirming correct flux regulation. The three-phase currents i_a, i_b, i_c (Fig 4.13(d)) and the measured and the components $i_{c_{mes}}$, $i_{c\alpha}$, $i_{c\beta}$, $|i_c|$ (Fig 4.13(h)) indicate accurate current tracking under all speed transitions.

Additionally, the estimated rotor flux angle θ_{est} (Fig 4.13(i)) varies smoothly, validating proper flux position tracking essential for SSDTC. These results collectively confirm that the proposed SSDTC achieves precise motor control, fast dynamic response, and high estimation accuracy, even under significant speed variations, highlighting its suitability for practical electric drive applications.

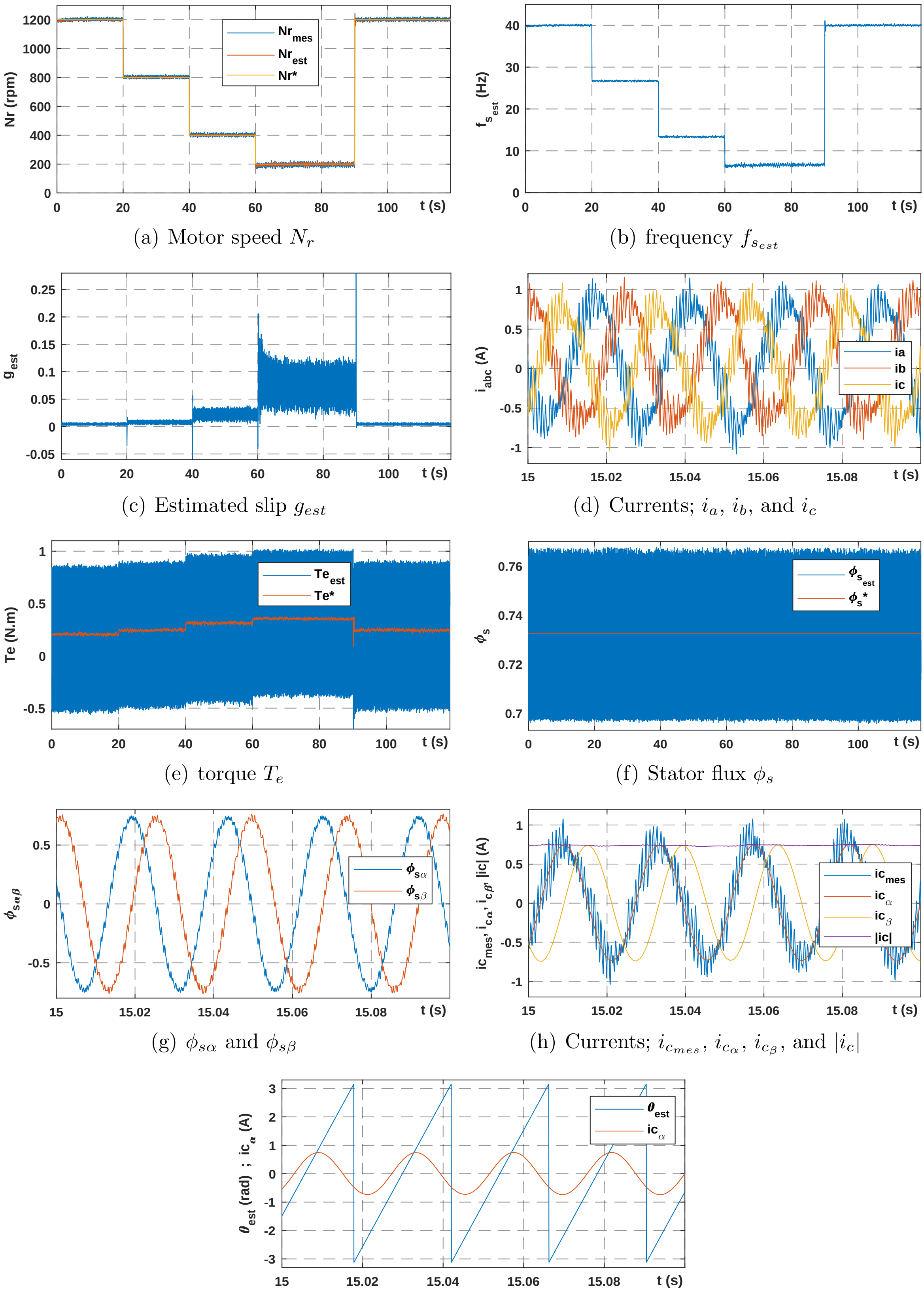

(a) Motor speed N_r

(b) frequency $f_{s_{est}}$

(c) Estimated slip g_{est}

(d) Currents; i_a, i_b, and i_c

(e) torque T_e

(f) Stator flux ϕ_s

(g) $\phi_{s\alpha}$ and $\phi_{s\beta}$

(h) Currents; $i_{c_{mes}}$, i_{c_α}, i_{c_β}, and $|i_c|$

(i) estimated angle (θ_{est}) *and* i_{c_α}

Fig 4.13. Experimental results under variable speed conditions.

4.4.2.2 Load variation Test

In this test, the performance of the proposed Mesogi-Fll-based SSDTC is evaluated under different load conditions at a fixed reference rotor speed of 1200 rpm. The load torque is gradually increased from 0.5 N.m to 1 N.m, 1.5 N.m, and finally 2 N.m, while the responses of the system are recorded, as shown in Fig 4.14.

Fig 4.14(a) indicates that the estimated speed follows the reference more smoothly and accurately than the measured, with less noise and no overshoot during disturbances. The estimated stator frequency (Fig 4.14(b)) adapts consistently to load changes, while the slip (Fig 4.14(c)) increases proportionally, reflecting expected machine behavior. The torque response (Fig 4.14(e)) tracks its reference precisely and rises with the applied load, confirming the controller's capability to meet torque demands. The flux components $\phi_{s\alpha}$ and $\phi_{s\beta}$ (Fig 4.14(g)) remain well-estimated and balanced, ensuring correct flux regulation.

The actual three-phase currents (Fig 4.14(d)) exhibit distortion under load, but the estimated signals $i_{c\alpha}$, $i_{c\beta}$, and $|i_c|$ (Fig 4.14(h)) remain well-filtered and free from significant offsets or harmonics. Finally, the estimated rotor flux angle θ_{est} (Fig 4.14(i)) varies smoothly, ensuring correct flux orientation for stable sensorless Dtc operation.

Overall, the results confirm that the proposed SSDTC achieves accurate estimation and robust control of speed, slip, torque, flux, and currents under load variations, validating its suitability for practical applications.

4.4.2.3 Reverse Speed Direction Test

This test evaluates the capability of the proposed controller to operate when the reference speed is reversed. The Im was initially set to operate at a fixed reference speed of 1200 rpm. At $t = 22$ s, the reference speed was switched to -1200 rpm, before returning to 1200 rpm at $t = 52$ s. The corresponding experimental results are presented in Fig 4.15, which reports the same variables as in the previous tests.

As shown in Fig 4.15(a), both the estimated and measured speeds accurately follow the applied reference, even during the reversal, demonstrating the robustness of the proposed method in bidirectional speed tracking. Rotor speed estimation also exhibits high accuracy throughout the test. The electromagnetic torque, presented in Fig 4.15(e), changes sign consistently with the negative reference speed while maintaining proper tracking performance. The estimated slip, illustrated in Fig 4.15(c), remains constant despite the reversal in rotation direction.

Similar observations to those reported in Test 1 apply to Fig 4.15(d), Fig 4.15(g), and Fig 4.15(h), except that the wave-forms are phase-shifted by π when the Im operates in the reverse direction.

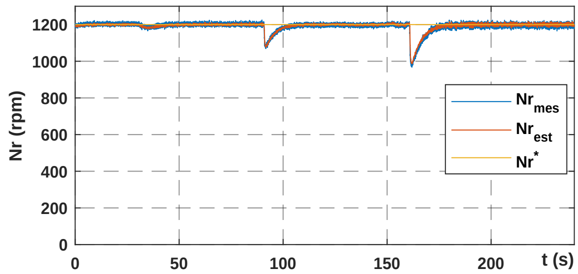

(a) Motor speed N_r

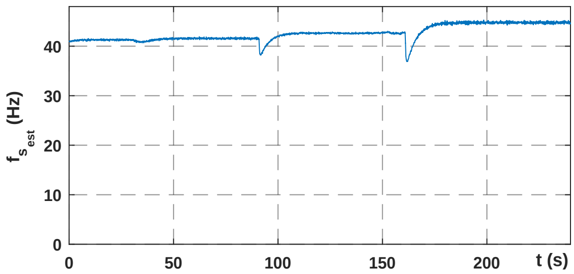

(b) frequency f_{sest}

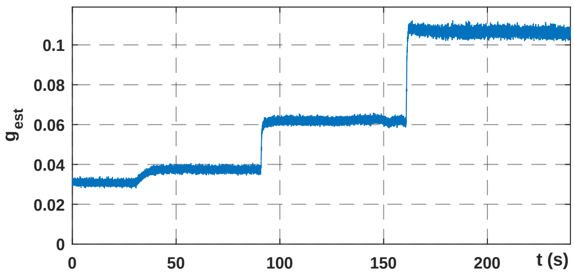

(c) Estimated slip g_{est}

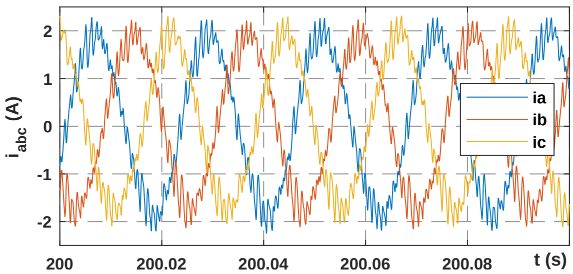

(d) Currents; i_a, i_b, and i_c

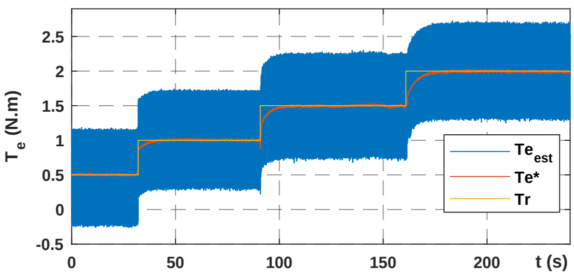

(e) torque T_e

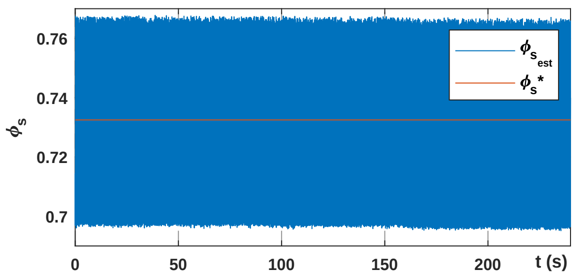

(f) Stator flux ϕ_s

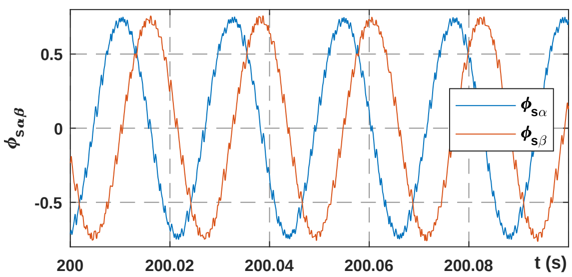

(g) $\phi_{s\alpha}$ and $\phi_{s\beta}$

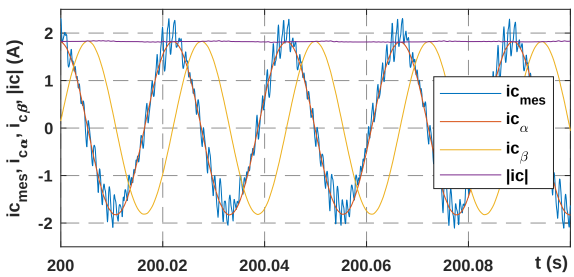

(h) Currents; $i_{c_{mes}}$, i_{c_α}, i_{c_β}, and $|i_c|$

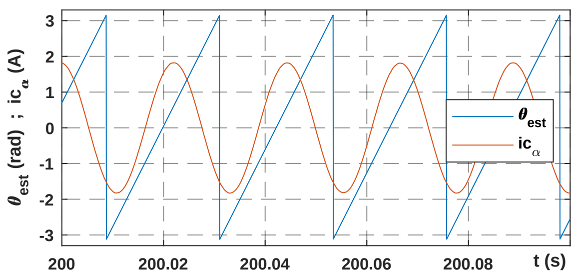

(i) estimated angle (θ_{est}) *and* i_{c_α}

Fig 4.14. Experimental results under load variation.

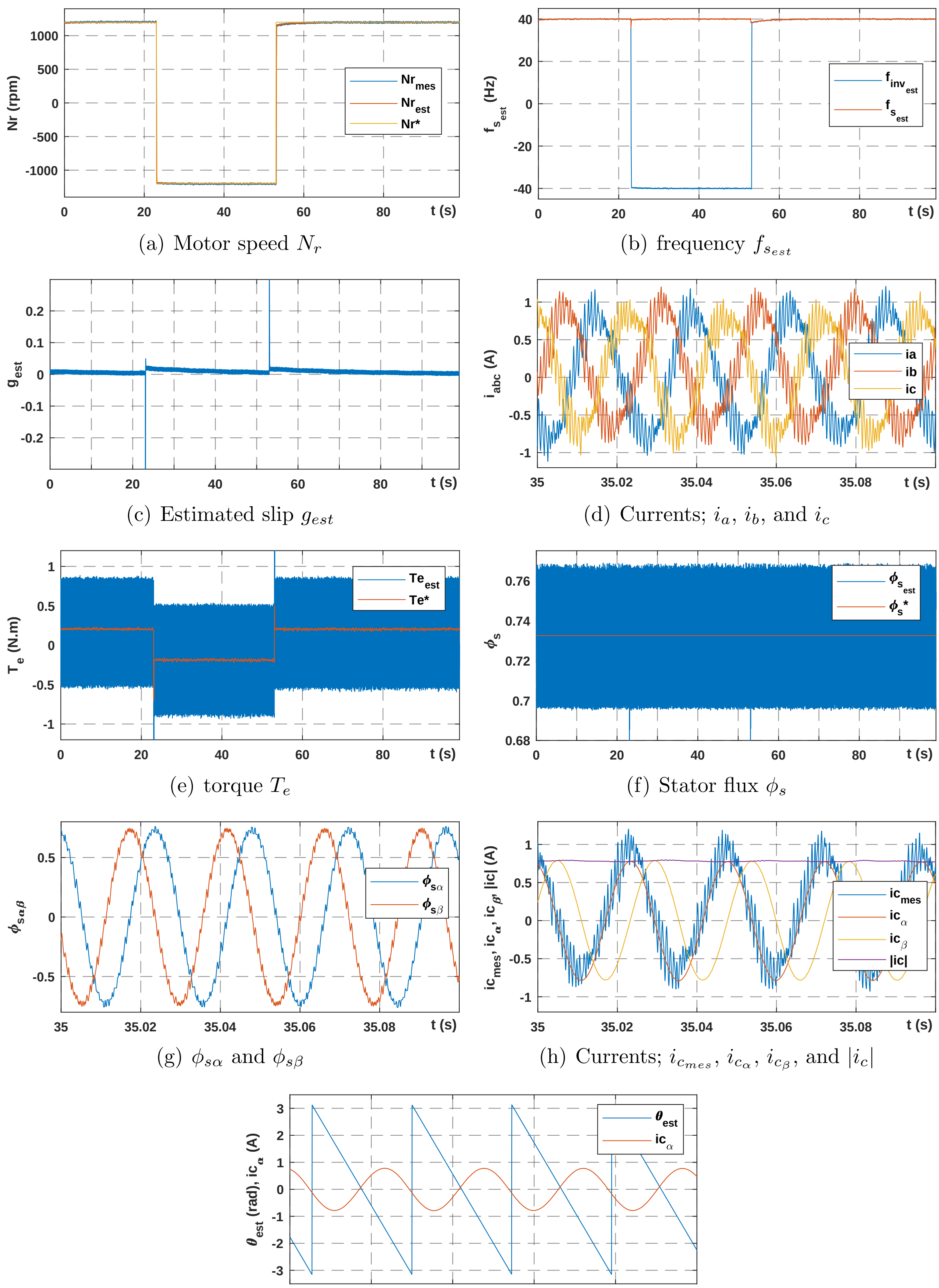

(a) Motor speed N_r

(b) frequency $f_{s_{est}}$

(c) Estimated slip g_{est}

(d) Currents; i_a, i_b, and i_c

(e) torque T_e

(f) Stator flux ϕ_s

(g) $\phi_{s\alpha}$ and $\phi_{s\beta}$

(h) Currents; $i_{c_{mes}}$, i_{c_α}, i_{c_β}, and $|i_c|$

(i) estimated angle (θ_{est}) *and* i_{c_α}

Fig 4.15. Experimental results for reverse speed direction test.

4.5 CONCLUSION

In this chapter, the sensorless Direct Torque Control (DTC) strategy of the induction motor based on the MESOGI-FLL estimator was developed and thoroughly evaluated. The New European Driving Cycle (NEDC) was successfully applied to the traction system, and the induction motor demonstrated stable performance across the cycle. The MESOGI-FLL estimator was integrated into the control framework and validated through detailed simulations and experimental analysis, confirming its ability to accurately estimate rotor speed and flux while ensuring fast dynamic response and reliable torque control. The results showed very good agreement between the reference and estimated values, thereby validating the robustness of the proposed estimator under different load and speed variations.

Nevertheless, a limitation was observed at low-speed operation, where the estimator could not maintain accurate performance due to the inherent challenges of weak back-EMF signals in this region. Despite this, the overall performance across medium- and high-speed ranges was excellent, and the approach proved highly effective for EV traction applications. The work presented in this chapter builds upon the modeling, estimator design, and implementation subsections, and it highlights both the strengths and the boundaries of the proposed method. These findings not only confirm the feasibility of the MESOGI-FLL-based sensorless DTC scheme but also provide valuable insights that can guide future research toward improving low-speed estimation accuracy and further enhancing the reliability of induction motor drives in electric vehicle applications.

General Conclusion

This thesis presented a comprehensive investigation into the modeling and control of electric drive systems, with a particular focus on induction motor control for electric vehicle (EV) applications. The research addressed both theoretical and practical challenges in achieving efficient, reliable, and sensorless motor control.

Initially, the thesis established a solid foundation by reviewing the role and evolution of electric vehicles, underlining the importance of energy efficiency and advanced drive systems in modern EV design. A detailed modeling of the EV traction system was then developed, integrating the electric motor and inverter as the main components of propulsion. The motor model was designed to represent its dynamic behavior accurately, and particular effort was devoted to the identification of induction motor parameters to ensure reliable performance under varying operating conditions. This modeling stage laid the groundwork for precise simulation and controller design.

The core contribution of the thesis lies in the development and evaluation of two sensorless control strategies for the induction motor. The scalar control approach, enhanced by the Second-Order Generalized Integrator Frequency-Locked Loop (SOGI-FLL) estimator, demonstrated improved performance in speed and flux estimation, making it suitable for low-complexity applications. Furthermore, a more advanced control technique, the Direct Torque Control (DTC) strategy integrated with a Multiplied Enhanced SOGI-FLL (MESOGI-FLL) estimator, was proposed and validated. This technique achieved high dynamic performance, accurate torque control, and robustness against parameter variations, all without relying on physical speed sensors.

The theoretical developments were supported by extensive simulations and experimental validations, confirming the effectiveness of the proposed estimators and control strategies. The results showed that both control schemes enable precise and stable operation of induction motors under various operating conditions, thereby contributing to the development of reliable and cost-effective EV drive systems.

Despite these achievements, several limitations were observed. The sensorless scalar control approach exhibits reduced accuracy at very low speeds due to fixed-slip operation and shows some sensitivity to torque fluctuations. The sensorless DTC strategy, although providing enhanced torque and flux control, is affected by torque ripples, especially under dynamic load conditions, and is limited at very low speeds. Additionally, the experimental validation was conducted on a laboratory-scale test bench, which may not fully capture real-world driving scenarios and extreme operating conditions.

Future work could focus on mitigating these limitations by developing enhanced estimation and control methods. In particular, the use of a three-phase MESOGI-FLL estimator could be explored to provide more accurate speed estimation and to filter torque ripples effectively, while also improving flux estimation under very low-speed conditions. Further research could include adaptive or hybrid control strategies to maintain high performance across the full speed range, testing on real vehicle platforms, and optimization of hardware implementation to reduce cost and computational complexity.

In summary, this work advances the state of sensorless motor control in EVs by providing novel estimation techniques and robust control schemes, contributing to the overall efficiency and feasibility of next-generation electric vehicle powertrains.

Appendix A

Powertrain Parameters

A.1 Induction Motor Parameters

Table A.1. Induction Motor Parameters.

Parameters	Symbol	Unit	Value
Rated Power	P_n	kw	0.55
Rated Voltage	V_n	V	230/400
Rated current	I_n	A	2.48/1.43
Rated Speed	N_n	rpm	1390
Pole Paire	p	/	2
Stator Resistance	R_s	Ω	12.5
Rotor Resistance	R_r	Ω	10.64
Magnetizing Inductance	M	H	0.66
Equivalent Inductance	L_{eq}	H	0.098
Stator Inductance	L_s	H	0.71
Rotor Inductance	L_r	H	0.71
Moment of Inertia	J	$kg.m^2$	0.0023
Friction Coefficient	C_f	$N{\cdot}m{\cdot}s/rad$	0.0008

A.2 Electric Vehicle Parameters

Table A.2. Electric Vehicle parameters

Parameter	Symbol	Unit	Value
Vehicle mass	m	80	kg
Wheel radius	R	0.23	m
Rolling resistance coefficient	K_r	0.015	/
Drag coefficient	C_d	0.2	/
Frontal surface area	A_s	0.6	m^2
Air density	ρ	1.2	kg/m^3
Gear ratio	g_r	2	/
Drivetrain efficiency	η	0.95	/

Appendix B

Experimental Setup

B.1 dSPACE MicroLabBox

The experimental setup is based on the **MicroLabBox (DS1202)** from dSPACE, a versatile real-time system for rapid prototyping and control algorithm implementation. It integrates seamlessly with MATLAB/SIMULINK via dSPACE RTI and ControlDesk, allowing automatic code generation and real-time parameter tuning.

Fig B.1. DS1202

The MicroLabBox provides multiple analog and digital I/O channels, encoder interfaces, and communication ports such as CAN, Ethernet, and serial, enabling direct connection to sensors, actuators, and power converters. Its high computational capability and low-latency operation make it ideal for electric drive applications, including scalar control, FOC, and DTC, and it serves as the central controller, acquiring motor feedback, executing real-time algorithms, and generating PWM signals to drive the inverter.

B.2 Control Desk

ControlDesk is a versatile software platform by dSPACE for real-time experiment control, monitoring, and data acquisition. It allows users to interactively configure experiments, visualize signals, tune parameters, and log data in real time. ControlDesk integrates seamlessly with the MicroLabBox and SIMULINK-generated code, enabling rapid testing of control algorithms and system performance monitoring.

Fig B.2. Control Desk

B.3 Isolation and Adaptation Card

The isolation and adaptation card interfaces the dSPACE controller with the power inverter. It converts low-voltage PWM signals (5V) from the controller to high-voltage signals (15V) for driving the inverter switches, while providing isolation between the control circuit and the high-power stage to protect against voltage spikes and noise. This ensures reliable operation of control algorithms, maintains signal integrity, and safeguards sensitive components in the setup.

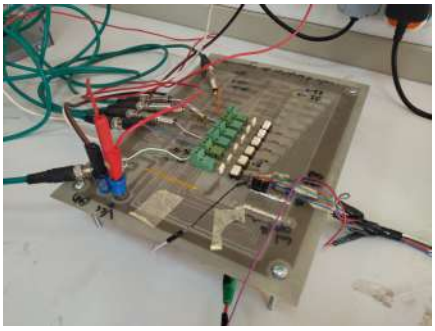

Fig B.3. Isolation and Adaptation Card 5-15V

B.4 Three-Phase Semikron IGBT Inverter

The experimental setup employs a three-phase IGBT educational inverter (SEMITEACH 08753450CA) from Semikron, which serves as the power conversion stage for the induction motor drive. The inverter is based on a conventional three-phase voltage-source topology and converts the DC-link voltage into a controlled AC supply for the motor. Switching commands are generated by the dSPACE MicroLabBox and applied via an isolation and adaptation board using PWM techniques. Its fast switching and reliable operation make it suitable for experimental validation of control strategies.

Fig B.4. Semikron inverter

B.5 Incremental Encoder (Speed Sensor)

The experimental setup uses an incremental encoder as the speed sensor, operating at DC 5-24 V with a resolution of 4096 pulses per revolution (P/R). This high-resolution encoder provides accurate rotor position and speed feedback to the MicroLabBox, which is essential for implementing real-time control algorithms. The encoder output is interfaced directly with the controller, and its signals are processed to calculate rotor speed, enabling precise execution of control strategies of the IM.

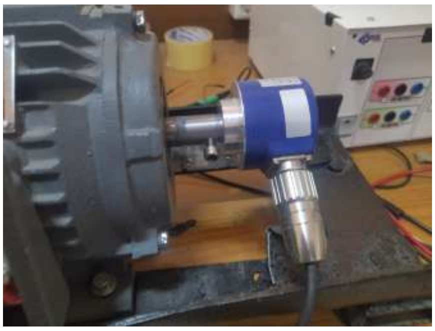

Fig B.5. Incremental Encoder

B.6 Current & Voltage Sensors with Adaptation Card

The experimental setup employs both current and voltage sensors, which were custom-fabricated in the laboratory using a CNC circuit printer. The design schematics of the sensors were created using the Proteus software, and the sensors provide feedback signals to the MicroLabBox for real-time control. Each sensor is connected to an adaptation card that processes the signals in three stages:

- **Gain multiplication:** Amplifies the low-level sensor signal to a voltage suitable for the controller.
- **DC-offset regulation:** Centers the signal within the MicroLabBox ADC input range to prevent saturation.
- **Filtering:** Removes high-frequency noise and transients, producing clean signals for precise control.

This dual adaptation setup ensures reliable measurement of both motor currents and voltages, which is crucial for implementing control strategies such as scalar control, Field-Oriented Control (FOC), and Direct Torque Control (DTC).

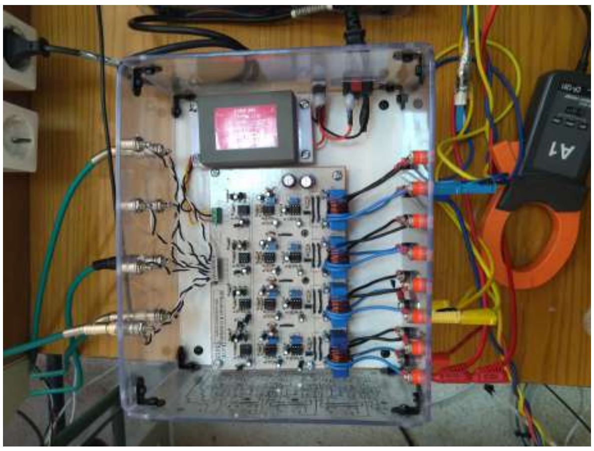

Fig B.6. Current Sensors.

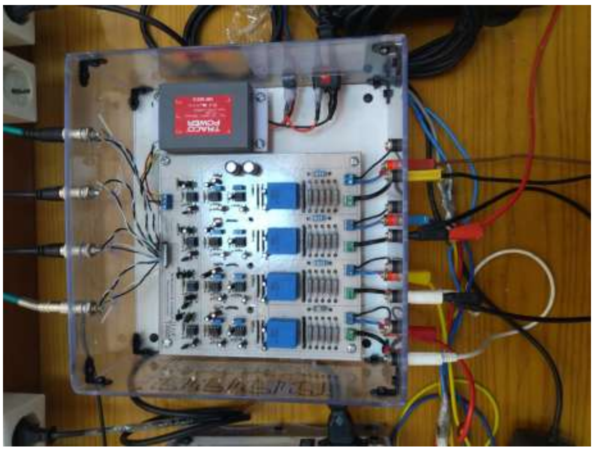

Fig B.7. Voltage Sensors.

B.7 Induction Motor

The experimental setup employs a three-phase Im, which serves as the primary load for testing control algorithms. This motor is directly driven by the Semicron inverter and receives PWM signals processed by the MicroLabBox through the isolation and adaptation card.

Fig B.8. Induction Motor

Its electrical and mechanical characteristics, such as rated power, voltage, current, and speed, are carefully selected to match the experimental conditions. The motor provides a realistic platform to evaluate control strategies including scalar control, Foc, Dtc under various operating scenarios.

B.8 Powder Brake and Torque Control Unit

The experimental setup includes a Magnetic Powder Brake for applying controllable load torque to the induction motor. The brake allows precise adjustment of mechanical load, enabling testing of the motor and control algorithms under various torque conditions. It is paired with a Torque Ccontrol Unit, which receives the torque profile from the dSPACE MicroLabBox and regulates the brake current to achieve the desired torque accurately.

This combination ensures that the motor experiences accurate, controllable load torque, allowing precise evaluation of types of control algorithms in the experimental setup. The torque control unit ensures the applied torque faithfully follows the profile generated by the MicroLabBox, providing reliable and repeatable testing conditions.

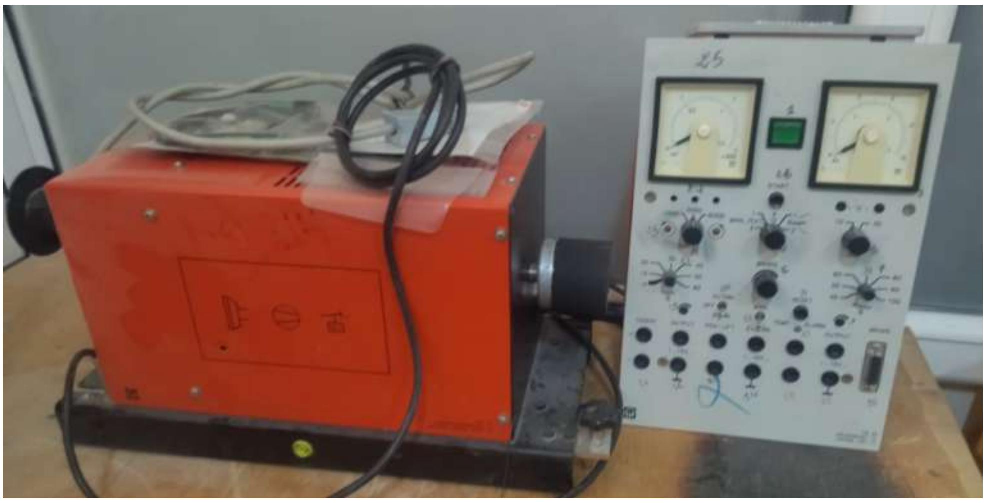

Fig B.9. Powder Brake and its Torque Control Unit

Bibliography

[1] Khaligh, A., & Li, Z. (2010). Battery, ultracapacitor, fuel cell, and hybrid energy storage systems for electric, hybrid electric, fuel cell, and plug-in hybrid electric vehicles: State of the art. IEEE transactions on Vehicular Technology, 59(6), 2806-2814.

[2] Larminie, J., & Lowry, J. (2012). Electric vehicle technology explained. John Wiley & Sons.

[3] Cao, W., Bukhari, A. A. S., & Aarniovuori, L. (2019). Review of electrical motor drives for electric vehicle applications. Mehran University Research Journal of Engineering & Technology, 38(3), 525-540.

[4] Bose, B. K. (1986). Power electronics and AC drives. Englewood Cliffs.

[5] Vas, P. (1998). Sensorless vector and direct torque control. Oxford university press.

[6] Blaschke, F. (1772). The principle of field orientation as applied to the new transvector closed-loop control system for rotating-field machine. Siemens review, 34, 217-220.

[7] Sepeeh, M. S., Zulkifli, S. A., Sim, S. Y., & Pathan, E. (2018). A comprehensive review of field-oriented control in sensorless control techniques for electric vehicle. Int. Rev. Electr. Eng.(IREE), 13, 461-475.

[8] Takahashi, I., & Noguchi, T. (2008). A new quick-response and high-efficiency control strategy of an induction motor. IEEE Transactions on Industry applications, (5), 820-827.

[9] Baader, U., Depenbrock, M., & Gierse, G. (2002). Direct self control (DSC) of inverter-fed induction machine: a basis for speed control without speed measurement. IEEE transactions on industry applications, 28(3), 581-588.

[10] Cirrincione, M., Accetta, A., Pucci, M., & Vitale, G. (2012). MRAS speed observer for high-performance linear induction motor drives based on linear neural networks. IEEE transactions on Power Electronics, 28(1), 123-134.

[11] Vas, P. (1998). Sensorless vector and direct torque control. Oxford university press.

[12] Ohtani, T., Takada, N., & Tanaka, K. (1992). Vector control of induction motor without shaft encoder. IEEE Transactions on Industry Applications, 28(1), 157-164.

[13] Holtz, J. (2006). Sensorless control of induction machines With or without signal injection. IEEE transactions on industrial electronics, 53(1), 7-30.

[14] Xu, D., Wang, B., Zhang, G., Wang, G., & Yu, Y. (2018). A review of sensorless control methods for AC motor drives. CES Transactions on electrical machines and systems, 2(1), 104-115.

[15] Ganapathy, R., & Santha, K. R. (2018). Review of sliding mode observers for sensorless control of permanent magnet synchronous motor drives. International Journal of Power Electronics and Drive Systems, 9(1), 46.

[16] Diab, A. A. Z., Elsawy, M. A., Denis, K. A., Alkhalaf, S., & Ali, Z. M. (2022). Artificial neural based speed and flux estimators for induction machine drives with matlab/simulink. Mathematics, 10(8), 1348.

[17] Hemalatha, N., Venkatesan, S., Kannan, R., Kannan, S., Bhuvanesh, A., & Kamaraja, A. S. (2024). Sensorless speed and position control of permanent magnet BLDC motor using particle swarm optimization and ANFIS. Measurement: Sensors, 31, 100960.

[18] Abdullah, Q., Farah, N., Ahmed, M. S., Shah, N. S. M., Aydodu, Ö., Talib, M. H. N., ... & Salh, A. (2024). Sensorless speed control of induction motor drives using reinforcement learning and self-tuning simplified fuzzy logic controller. IEEE Access.

[19] Kanakabettu, A. K. M., Irvathoor, R. B., Saralaya, S., Jodumutt, S. B., & Singh, A. B. (2024). Novel Advanced Artificial Neural Network-Based Online Stator and Rotor Resistance Estimator for Vector-Controlled Speed Sensorless Induction Motor Drives. Energies, 17(9), 2150.

[20] Bamigbade, A., & Khadkikar, V. (2022). Frequency estimators for SOGI FLL: Modeling, design, and equivalence for FLL advancements. IEEE Transactions on Instrumentation and Measurement, 71, 1-12.

[21] Shi, W., & Yu, J. (2023). Weakly time-variant SOGI-based frequency derivative estimator. IEEE Transactions on Power Electronics, 38(7), 8056-8061.

[22] Chan, C. C. (2007). The state of the art of electric, hybrid, and fuel cell vehicles. Proceedings of the IEEE, 95(4), 704-718.

[23] Husain, I. (2021). Electric and hybrid vehicles: design fundamentals. CRC press.

[24] Ehsani, M., Gao, Y., Longo, S., & Ebrahimi, K. (2018). Modern electric, hybrid electric, and fuel cell vehicles. CRC press.

[25] Chan, C. C. (2002). The state of the art of electric and hybrid vehicles. Proceedings of the IEEE, 90(2), 247-275.

[26] Zeraoulia, M., Benbouzid, M. E. H., & Diallo, D. (2006). Electric motor drive selection issues for HEV propulsion systems: A comparative study. IEEE Transactions on Vehicular technology, 55(6), 1756-1764.

[27] Miller, J. M. (2008). Propulsion systems for hybrid vehicles (Vol. 2). Iet.

[28] Larminie, J., & Lowry, J. (2012). Electric vehicle technology explained. John Wiley & Sons.

[29] Goodenough, J. B., & Park, K. S. (2013). The Li-ion rechargeable battery: a perspective. Journal of the American Chemical Society, 135(4), 1167-1176.

[30] Dunn, B., Kamath, H., & Tarascon, J. M. (2011). Electrical energy storage for the grid: a battery of choices. Science, 334(6058), 928-935.

[31] Emadi, A., Williamson, S. S., & Khaligh, A. (2006). Power electronics intensive solutions for advanced electric, hybrid electric, and fuel cell vehicular power systems. IEEE Transactions on power electronics, 21(3), 567-577.

[32] Chan, C. C., & Chau, K. T. (2001). Modern electric vehicle technology (Vol. 47). oxford University press.

[33] Pillay, P., & Krishnan, R. (2002). Application characteristics of permanent magnet synchronous and brushless DC motors for servo drives. IEEE Transactions on industry applications, 27(5), 986-996.

[34] Krishnan, R. (2017). Permanent magnet synchronous and brushless DC motor drives. CRC press.

[35] Husain, I. (2002). Minimization of torque ripple in SRM drives. IEEE Transactions on industrial electronics, 49(1), 28-39.

[36] Tarascon, J. M., & Armand, M. (2001). Issues and challenges facing rechargeable lithium batteries. nature, 414(6861), 359-367.

[37] Hossain Lipu, M. S., Miah, M. S., Ansari, S., Meraj, S. T., Hasan, K., Elavarasan, R. M., ... & Hussain, A. (2022). Power electronics converter technology integrated energy storage management in electric vehicles: emerging trends, analytical assessment and future research opportunities. Electronics, 11(4), 562.

[38] Gnann, T., Funke, S., Jakobsson, N., Plötz, P., Sprei, F., & Bennehag, A. (2018). Fast charging infrastructure for electric vehicles: Today's situation and future needs. Transportation Research Part D: Transport and Environment, 62, 314-329.

[39] Sanguesa, J. A., Torres-Sanz, V., Garrido, P., Martinez, F. J., & Marquez-Barja, J. M. (2021). A review on electric vehicles: Technologies and challenges. Smart Cities, 4(1), 372-404

[40] Parag Jose, C., & Meikandasivam, S. (2016). A review on the trends and developments in hybrid electric vehicles. Innovative Design and Development Practices in Aerospace and Automotive Engineering: I-DAD, February 22-24, 2016, 211-229.

[41] Chen, Z., Lu, J., Liu, B., Zhou, N., & Li, S. (2020). Optimal energy management of plug-in hybrid electric vehicles concerning the entire lifespan of lithium-ion batteries. Energies, 13(10), 2543.

[42] Zhao, F., Mu, Z., Hao, H., Liu, Z., He, X., Victor Przesmitzki, S., & Ahmad Amer, A. (2020). Hydrogen fuel cell vehicle development in China: An industry chain perspective. Energy Technology, 8(11), 2000179.

[43] Liu, H., Wei, Z., He, W., & Zhao, J. (2017). Thermal issues about Li-ion batteries and recent progress in battery thermal management systems: A review. Energy conversion and management, 150, 304-330.

[44] Hegazy, O., Barrero, R., Van Mierlo, J., Lataire, P., Omar, N., & Coosemans, T. (2013). An advanced power electronics interface for electric vehicles applications. IEEE transactions on power electronics, 28(12), 5508-5521..

[45] Yang, Z., Shang, F., Brown, I. P., & Krishnamurthy, M. (2015). Comparative study of interior permanent magnet, induction, and switched reluctance motor drives for EV and HEV applications. IEEE Transactions on Transportation Electrification, 1(3), 245-254.

[46] Hofman, T., & Dai, C. H. (2010, September). Energy efficiency analysis and comparison of transmission technologies for an electric vehicle. In 2010 IEEE vehicle power and propulsion conference (pp. 1-6). IEEE.

[47] Du, G., Zou, Y., Zhang, X., Kong, Z., Wu, J., & He, D. (2019). Intelligent energy management for hybrid electric tracked vehicles using online reinforcement learning. Applied Energy, 251, 113388.

[48] Husain, I., Ozpineci, B., Islam, M. S., Gurpinar, E., Su, G. J., Yu, W., ... & Sahu, R. (2021). Electric drive technology trends, challenges, and opportunities for future electric vehicles. Proceedings of the IEEE, 109(6), 1039-1059.

[49] Krishnan, R. (2001). Electric motor drives: modeling, analysis, and control. Prentice Hall..

[50] Bdewi, M. Y., Mohammed, A. M., & Ezzaldean, M. M. (2021). Design and performance analysis of permanent magnet synchronous motor for electric vehicles application. Engineering and Technology Journal, 39(03 Part A), 394-406.

[51] Esho, A. O. O., Iluyomade, T. D., Olatunde, T. M., & Igbinenikaro, O. P. (2024). Electrical propulsion systems for satellites: a review of current technologies and future prospects. International Journal of Frontiers in Engineering and Technology Research, 6(02), 035-044.

[52] Mohammad, K. S., & Jaber, A. S. (2022). Comparison of electric motors used in electric vehicle propulsion system. Indonesian Journal of Electrical Engineering and Computer Science, 27(1), 11-19.

[53] Krause, P. C., Wasynczuk, O., Sudhoff, S. D., & Pekarek, S. (2002). Analysis of electric machinery and drive systems (Vol. 2). New York: IEEE press.

[54] Leonhard, W. (2001). Control of electrical drives. Springer Science & Business Media.

[55] Demerdash, N. A., He, J., & Chen, H. (2025). Electric Machinery and Drives: An Electromagnetics Perspective. John Wiley & Sons.

[56] Merabet, E. (2008). Commande Floue Adaptative d0une Machine Asynchrone Double Etoile (Doctoral dissertation, Université de Batna 2).

[57] Manoharan, P., Ravichandran, S., Siva Kumar, J. S., Abdullah, M., Ching Sin, T., & Tengku Hashim, T. J. (2025). Electrical Equivalent Circuit Parameter Estimation of Commercial Induction Machines Using an Enhanced Grey Wolf Optimization Algorithm. Biomimetics, 10(4), 228.

[58] Zhong, Z., Fang, X., Lin, F., & Yang, Z. (2024). Multi-parameter identification method of induction motor based on coupling and small signal injection. IET Electric Power Applications, 18(10), 1317-1331.

[59] Reddy, B. K., Ayyagari, K. S., Kumar, Y. P., Giri, N. C., Rajgopal, P. V., Fotis, G., & Mladenov, V. (2024). Experimental Benchmarking of Existing Offline Parameter Estimation Methods for Induction Motor Vector Control. Technologies, 12(8), 123.

[60] Gülbahçe, M. O., & Karaaslan, M. E. (2022). Estimation of Induction Motor Equivalent Circuit Parameters from Manufacturer's Datasheet by Particle Swarm Optimization Algorithm for Variable Frequency Drives. Electrica, 22(1).

[61] Manual, F. (2007). ACS800 Standard Control Program 7. x. ABB Oy, Helsinki, Finland.

[62] Moradi, A. (2021). PLC-järjestelmän implementointi GreenLine-testauslinjalle.

[63] Odhano, S. A., Pescetto, P., Awan, H. A. A., Hinkkanen, M., Pellegrino, G., & Bojoi, R. (2018). Parameter identification and self-commissioning in AC motor drives: A technology status review. IEEE Transactions on Power Electronics, 34(4), 3603-3614.

[64] Depenbrock, M. (1987, June). Direct self-control (DSC) of inverter fed induktion machine. In 1987 IEEE power electronics specialists conference (pp. 632-641). IEEE.

[65] Bechouche, A., Sediki, H., Abdeslam, D. O., & Haddad, S. (2011). A novel method for identifying parameters of induction motors at standstill using ADALINE. IEEE Transactions on Energy Conversion, 27(1), 105-116.

[66] Toliyat, H. A., Nandi, S., Choi, S., & Meshgin-Kelk, H. (2012). Electric machines: modeling, condition monitoring, and fault diagnosis. CRC press.

[67] Babau, R., Boldea, I., Miller, T. J. E., & Muntean, N. (2007). Complete parameter identification of large induction machines from no-load acceleration?deceleration tests. IEEE transactions on industrial electronics, 54(4), 1962-1972.

[68] Krishnan, R. (2001). Electric motor drives: modeling, analysis, and control. Prentice Hall.

[69] Haddoun, A., Benbouzid, M. E. H., Diallo, D., Abdessemed, R., Ghouili, J., & Srairi, K. (2007). A loss-minimization DTC scheme for EV induction motors. IEEE Transactions on vehicular technology, 56(1), 81-88.

[70] Best, R. E. (2007). Phase-locked loops: design, simulation, and applications. McGraw-Hill Education.

[71] RXiao, F., Dong, L., Li, L., & Liao, X. (2016). A frequency-fixed SOGI-based PLL for single-phase grid-connected converters. IEEE Transactions on Power Electronics, 32(3), 1713-1719.

[72] Hasan, M. Z., Shiam, I. F., Nova, T. T., & Reza, M. S. (2019, February). A modified PLL based on second order generalized integrator for single-phase voltage system. In 2019 International Conference on Electrical, Computer and Communication Engineering (ECCE) (pp. 1-6). IEEE.

[73] Dang, K., Li, W., Chen, W., & Wang, G. (2025). An SOGI-Based Cross-Coupled Filtering Method for Speed and Position Estimation in Low-Cost PMSM Drives Using Hall-Effect Sensors. IEEE Transactions on Power Electronics.

[74] Ardalan, P., Rasekh, N., Khaneghah, M. Z., Abrishamifar, A., & Saeidi, M. (2022). A modified SOGI-FLL algorithm with DC-offset rejection improvement for single-phase inverter applications. International Journal of Dynamics and Control, 10(6), 2020-2033.

[75] Priyanka, B., & Lavanya, M. C. (2024, February). Phase-locked loop (PLL) techniques for grid synchronization: A comprehensive review. In 2024 Second International Conference on Emerging Trends in Information Technology and Engineering (ICETITE) (pp. 1-9). IEEE.

[76] Matas, J., Martín, H., de la Hoz, J., Abusorrah, A., Al-Turki, Y., & Alshaeikh, H. (2019). A new THD measurement method with small computational burden using a SOGI-FLL grid monitoring system. IEEE Transactions on Power Electronics, 35(6), 5797-5811.

[77] Babu, N., Guerrero, J. M., Siano, P., Peesapati, R., & Panda, G. (2020). A novel modified control scheme in grid-tied photovoltaic system for power quality enhancement. IEEE Transactions on Industrial Electronics, 68(11), 11100-11110.

[78] Golestan, S., Guerrero, J. M., Abusorrah, A., Al-Hindawi, M. M., & Al-Turki, Y. (2016). An adaptive quadrature signal generation-based single-phase phase-locked loop for grid-connected applications. IEEE Transactions on Industrial Electronics, 64(4), 2848-2854.

[79] Wang, H., Yang, Y., Ge, X., Zuo, Y., Yue, Y., & Li, S. (2021). PLL-and FLL-based speed estimation schemes for speed-sensorless control of induction motor drives: Review and new attempts. IEEE Transactions on Power Electronics, 37(3), 3334-3356.

[80] Krause, P. C., Wasynczuk, O., Sudhoff, S. D., & Pekarek, S. (2002). Analysis of electric machinery and drive systems (Vol. 2). New York: IEEE press.

[81] Vas, P. (1998). Sensorless vector and direct torque control. Oxford university press.

[82] Bose, B. K. (1986). Power electronics and AC drives. Englewood Cliffs.

[83] Pillay, P., & Krishnan, R. (2002). Application characteristics of permanent magnet synchronous and brushless DC motors for servo drives. IEEE Transactions on industry applications, 27(5), 986-996.

[84] Muhammad, H. R. (2004). Power Electronics-Circuits, Devices, and Applications. Upper Saddle River, NJ, Pearson Prentice Hall.

[85] Teodorescu, R., Liserre, M., & Rodriguez, P. (2011). Grid converters for photovoltaic and wind power systems. John Wiley & Sons.

[86] Freijedo, F. D., Doval-Gandoy, J., Lopez, O., Martinez-Penalver, C., Yepes, A. G., Fernandez-Comesana, P., ... & Lago, A. (2009, November). Grid-synchronization methods for power converters. In 2009 35th Annual Conference of IEEE Industrial Electronics (pp. 522-529). IEEE.

[87] Karimi-Ghartemani, M., & Iravani, M. R. (2002). A nonlinear adaptive filter for online signal analysis in power systems: applications. IEEE Transactions on Power Delivery, 17(2), 617-622.

[88] Rahman, M. A., Vilathgamuwa, D. M., Uddin, M. N., & Tseng, K. J. (2003). Nonlinear control of interior permanent-magnet synchronous motor. IEEE Transactions on Industry Applications, 39(2), 408-416.

[89] Labbe, B. (2013). A contribution to synchronization of the sliding-mode control-based integrated step-down DC/DC converter (Doctoral dissertation, INSA de Lyon).

[90] Yazdani, A., & Iravani, R. (2010). Voltage-sourced converters in power systems: modeling, control, and applications. John Wiley & Sons.

[91] Vásquez, J. C., Guerrero, J. M., Gregorio, E., Rodríguez, P., Teodorescu, R., & Blaabjerg, F. (2008, June). Adaptive droop control applied to distributed generation inverters connected to the grid. In 2008 IEEE international symposium on industrial electronics (pp. 2420-2425). IEEE.

[92] MO?D?Y?SKI, Kamil, RAFA?, Krzysztof, et BOBROWSKA-RAFA?, Ma?gorzata. Application of the second order generalized integrator in digital control systems. Archives of Electrical Engineering, 2014, vol. 63, no 3.

[93] Kherbachi, Abdelhammid, Ahmed Bendib, Kamel Kara, and Aissa Chouder. "ARM based implementation of SOGI-FLL method for power calculation in single-phase power system." In 2017 5th International Conference on Electrical Engineering-Boumerdes (ICEE-B), pp. 1-6. IEEE, 2017.

[94] Rodriguez, P., Luna, A., Candela, I., Teodorescu, R., & Blaabjerg, F. (2008, November). Grid synchronization of power converters using multiple second order generalized integrators. In 2008 34th Annual Conference of IEEE Industrial Electronics (pp. 755-760). IEEE.

[95] Vas, P. (1998). Sensorless vector and direct torque control. Oxford university press.

[96] Blaschke, F. (1772). The principle of field orientation as applied to the new transvector closed-loop control system for rotating-field machine. Siemens review, 34, 217-220.

[97] Casadei, D., Serra, G., Tani, A., & Zarri, L. (2013, March). Direct torque control for induction machines: A technology status review. In 2013 IEEE Workshop on Electrical Machines Design, Control and Diagnosis (WEMDCD) (pp. 117-129). IEEE.

[98] Douiri, M. R., & Cherkaoui, M. (2013). Comparative study of various artificial intelligence approaches applied to direct torque control of induction motor drives. Frontiers in Energy, 7(4), 456-467.

[99] Chu, Y., Fang, Y., & Fei, J. (2017). Adaptive neural dynamic global PID sliding mode control for MEMS gyroscope. International Journal of Machine Learning and Cybernetics, 8(5), 1707-1718.

[100] Xu, D., Wang, B., Zhang, G., Wang, G., & Yu, Y. (2018). A review of sensorless control methods for AC motor drives. CES Transactions on electrical machines and systems, 2(1), 104-115.

[101] YOON, Young-Doo et SUL, Seung-Ki. Sensorless control for induction machines based on square-wave voltage injection. IEEE Transactions on Power Electronics, 2013, vol. 29, no 7, p. 3637-3645.

[102] Mohan, H., Pathak, M. K., & Dwivedi, S. K. (2020). Sensorless control of electric drives?a technological review. IETE Technical Review, 37(5), 504-528.

[103] Rodriguez, P., Luna, A., Munoz-Aguilar, R. S., Etxeberria-Otadui, I., Teodorescu, R., & Blaabjerg, F. (2011). A stationary reference frame grid synchronization system for three-phase grid-connected power converters under adverse grid conditions. IEEE transactions on power electronics, 27(1), 99-112.

[104] Karimi-Ghartemani, M., & Iravani, M. R. (2004). Robust and frequency-adaptive measurement of peak value. IEEE Transactions on Power Delivery, 19(2), 481-489.

[105] Golestan, S., Mousazadeh, S. Y., Guerrero, J. M., & Vasquez, J. C. (2017). A critical examination of frequency-fixed second-order generalized integrator-based phase-locked loops. IEEE Transactions on Power Electronics, 32(9), 6666-6672.

[106] Saha, B., & Singh, B. (2024). Torque ripple mitigation in sensorless PMBLDC motor drive with adaptive observer for LEV. IEEE Transactions on Power Electronics.

[107] Giechaskiel, B., Joshi, A., Ntziachristos, L., & Dilara, P. (2019). European regulatory framework and particulate matter emissions of gasoline light-duty vehicles: A review. Catalysts, 9(7), 586.

[108] Takahashi, I., & Noguchi, T. (2008). A new quick-response and high-efficiency control strategy of an induction motor. IEEE Transactions on Industry applications, (5), 820-827.

[109] Depenbrock, M. (1987, June). Direct self-control (DSC) of inverter fed induktion machine. In 1987 IEEE power electronics specialists conference (pp. 632-641). IEEE.

[110] Casadei, D., Profumo, F., Serra, G., & Tani, A. (2002). FOC and DTC: two viable schemes for induction motors torque control. IEEE transactions on Power Electronics, 17(5), 779-787.

[111] Vas, P. (1998). Sensorless vector and direct torque control. Oxford university press.

[112] Aissa, O., Reffas, A., Talhaoui, H., Ziane, D., & Saim, A. (2023). An Improved Direct Torque Control with an Advanced Broken Bar Fault Diagnosis for Induction Motor Drives. International Transactions on Electrical Energy Systems, 2023(1), 8816896.

[113] Gudey, S. K., Malla, M., Jasthi, K., & Gampa, S. R. (2023). Direct torque control of an induction motor using fractional-order sliding mode control technique for quick response and reduced torque ripple. World Electric Vehicle Journal, 14(6), 137.

[114] Mahfoud, S., El Ouanjli, N., Derouich, A., El Idrissi, A., Chetouani, E., Loulijat, A., ... & Mosaad, M. I. (2025). An advanced direct torque control for doubly fed induction motor using evolutionary computational techniques. Scientific Reports, 15(1), 22719.

[115] Fahassa, C., Zahraoui, Y., Akherraz, M., Kharrich, M., Elattar, E. E., & Kamel, S. (2022). Induction motor DTC performance improvement by inserting fuzzy logic controllers and twelve-sector neural network switching table. Mathematics, 10(9), 1357.

[116] Kherbachi, A., Bendib, A., Chouder, A., Ahmed, H., Benbouzid, M., & Motahhir, S. (2024). Design and analysis of virtual impedance control scheme based on MESOGI for improving harmonic sharing of nonlinear loads. Scientific Reports, 14(1), 13356.

[117] Kherbachi, A., Chouder, A., Bendib, A., Kara, K., & Barkat, S. (2019). Enhanced structure of second-order generalized integrator frequency-locked loop suitable for DC-offset rejection in single-phase systems. Electric Power Systems Research, 170, 348-357.

[118] Krause, P. C., Wasynczuk, O., Sudhoff, S. D., & Pekarek, S. (2002). Analysis of electric machinery and drive systems (Vol. 2). New York: IEEE press.